

Flume Construction and RFID Tracking Techniques for Fluvial Sediment Transport Studies

by

John James Hufnagel

A thesis

presented to the University of Waterloo

in fulfillment of the

thesis requirement for the degree of

Masters of Applied Science

in

Civil Engineering

Waterloo, Ontario, Canada, 2016

©John James Hufnagel 2016

AUTHOR'S DECLARATION

I hereby declare that I am the sole author of this thesis. This is a true copy of the thesis, including any required final revisions, as accepted by my examiners.

I understand that my thesis may be made electronically available to the public.

Abstract

Sediment transport studies incorporating radio frequency identification (RFID) tracers are becoming a key component in understanding sediment transport dynamics due to the data they provide on spatial and temporal variability. This technique involves inserting small glass cylindrical transponders into stones then seeding those stones in the river bed. Existing methods of using RFID tracers involve either manually sweeping the channel bed after a hydrologic event or placing a series of fixed antennas along the channel to detect when sediment containing a RFID tracer passes that point. The first method is limited because it does not correlate the hydrodynamic conditions with the movement of the sediment, while the second method is limited by spatial resolution afforded by the fixed antennas.

The goal of this research is to develop a flume with the capacity to accurately measure sediment inputs, transport, and export in real time. This is accomplished by automating the sediment supply, using a sediment trap with a light table to monitor sediment leaving the flume, and implementing an RFID sediment tracking system to provide real time tracking of the movement of individual clasts over the course of an experiment.

A tilting flume with sediment supply and capture systems was designed and built with an integrated RFID tracking system to enable sediment transport experiments to be conducted in the flume while continuously tracking the position of RFID tagged sediment. The RFID tracking system, located under the floor of the flume, consists of a carriage containing the antennas, tuners, multiplexing RFID readers, batteries, and rollers to enable the carriage to roll along the flanges of the beam supporting the flume. The carriage is transported back and forth the length of the flume using cogged belts and pulleys powered by a DC motor and controlled by a PLC with limit switches. The identification of RFID tags detected by the carriage is transmitted Bluetooth to a stationary computer that also receives carriage position information from a laser range finder.

Validation tests were conducted with vertically oriented RFID tags to establish the detection range and accuracy of estimating RFID tag positions. When no steel cross members were present, an RFID tag could be detected up to 21 cm above the flume floor with streamwise position estimation accurate within 1 cm. When steel cross members or multiple RFID tags were present, the detection range and position estimation accuracy decreased. Further refinement to this technique could be achieved by experimenting with different antenna designs which may provide a larger detection range and by using different type of PIT tags to enable tracking of smaller sized sediment. The developed flume

and tracking system will allow us to obtain new and better information about sediment transport which should improve fundamental understanding and aid in the design of channel restoration projects.

Acknowledgements

I would like to thank my supervisor, Dr. Bruce MacVicar, for his guidance and support through this research project. Without his support, this research would not have been possible.

I would also like to acknowledge the financial contributions from the Canadian Foundation for Innovation and the lab space provided in the Hydraulics Lab at the University of Waterloo.

I extend my thanks to all the people who made completing my masters degree a much more rewarding and unique experience: Scott Dilling, Christina Bright, Vernon Bevan, Cailey McCutcheon, Margot Chapuis, Terry Ridgway, Kavinaath Muruga, Julian Krick, Elli Papangelakis, and the staff in the engineering machine shop.

Finally, I would like to thank my family: Felix, Aisha and most of all, my wife Rhonda.

Table of Contents

Chapter 1 Introduction.....	1
Chapter 2 Literature Review	3
2.1 Direct Measurements.....	4
2.1.1 Integrated Direct Sampling Methods.....	4
2.1.1.1 Bedload Traps.....	4
2.1.1.2 Screened Gates and Baskets on Flume	6
2.1.1.3 Slot or Pit Samplers	9
2.1.2 Localized Direct Sampling Methods	11
2.2 Indirect Transport Measurements.....	13
2.2.1 Motion Picture Photography.....	14
2.2.2 Painted Sediment	15
2.2.3 Video Analysis of Light Table	16
2.2.4 Acoustic Doppler Current Profiler Bedload Velocity	18
2.2.5 Piezoelectric bedload impact sensors	19
2.3 Tracers	20
2.3.1 Radioactive tracers on sand	21
2.3.2 Magnetic and Iron and Radio Tracers	22
2.3.3 RFID Tracers	25
2.3.4 RFID Sediment Transport Research Gap	26
Chapter 3 Design and Construction of Flume	27
3.1.1 Flume Tilting Mechanism	28
3.1.1.1 Multiple Jack Screws.....	28
3.1.1.2 Multiple Scissor Lift Jacking System.....	31
3.1.1.3 Single Hydraulic Support Tilting Design.....	33

3.1.2 Flume Structural Design.....	35
3.1.3 Water Contact Surface Design and Sealing.....	40
3.1.4 Sediment Supply with Vibratory Feeder	41
3.1.5 Sediment Extractor with Light Table Measurement.....	45
Chapter 4 Design and Construction of RFID Tracking System	49
4.1 RFID Background	49
4.1.1 RFID Operating Principals	49
4.1.2 Elements of an RFID system.....	51
4.1.2.1 RFID Transponder Design.....	52
4.1.2.2 Antenna Design and Detection Ranges	52
4.1.2.3 RFID Reader Systems	55
4.1.3 Multiplexer Units.....	59
4.1.3.1 BioMark™ Multiplexing Transceiver	62
4.1.3.2 Oregon RFID HDS Reader Antenna and Multiplexer.....	63
4.2 Design of flume RFID sediment tracking carriage.....	65
4.2.1 RFID Carriage Movement Design.....	65
4.2.1.1 Carriage Movement Mechanical Design.	65
4.2.1.1.1 Rack and Pinion Drive.....	66
4.2.1.1.2 Screw Drive	67
4.2.1.1.3 Cogged Belt Drive	67
4.2.1.2 Automation of Motion Control.....	68
4.2.1.2.1 Servo Drive with PLC	69
4.2.1.2.2 DC Motor with Arduino	70
4.2.1.2.3 DC Motor with PLC and 4 state Motor Controller.....	72
4.2.2 RFID Carriage Assembly	73

Chapter 5 Experimental Results Demonstrating RFID Carriage determined Positions of Particles. ...	75
5.1 RFID Tag Detection with no Steel within detection range.....	76
5.2 RFID Tag Detection with Steel Support Beam	79
5.3 Traverse RFID tag across flume.....	83
5.4 RFID tag proximity and collision.....	88
Chapter 6 Summary and Conclusions	93
Bibliography	96
Appendix A Bluetooth Connection to Oregon RFID Multiplexer	107
Appendix B PLC and Limit Switch Logic	111
Appendix C Jack Screw Details	115
Appendix D Using USB Port on Windows Computer to Connect with Oregon RFID Multiplexer..	118
Appendix E RFID Mechanical Drive Components.....	120
Appendix F Servo Drive Pricing Sheet	121

List of Figures

Figure 1: Diagrammatic view of shorter experimental trough (Gilbert & Murphy, 1914)	5
Figure 2 Variations of Sampling bedload discharge documented by Ehrenberger in 1931 (as cited in Hubbell D. W., 1964)	7
Figure 3 Results of Bedload collections during one hour in a laboratory flume documented by Einstien in 1931 (as cited in Hubbell D. W., 1964).....	8
Figure 4 Total Transport Rate Verses Time (Kuhnle & Southard, 1988)	9
Figure 5 Schematic diagram of the Birkbeck slot-sampler (Reid, et al., 1995)	11
Figure 6 Helley-Smith Bedload Sampler (Emmett, 1980)	12
Figure 7 Bunte Bedload Sampler (Bunte, et al., 2008).....	13
Figure 8 Pixel spacing grid for the measurement of mean surface grain size fraction.....	16
Figure 9 Flume Outlet with Light Table and Camera (Zimmermann, et al., 2008)	17
Figure 10 Schematic Diagram of PBIS (Rickenmann & McArdell, 2007)	19
Figure 11 Arrangement of PBIS array across channel width (Rickenmann & McArdell, 2007).....	20
Figure 12 Distribution of Step Length and Rest Period (Schmidt & Ergenzinger, 1992).....	24
Figure 13 Side View of Complete Flume Assembly	27
Figure 14 Screw Jack Construction (Joyce Dayton, 2013).....	29
Figure 15 Double Clevis Jack Screw (Joyce Dayton, 2013)	30
Figure 16 Jack Screw System with Mitre Gear Boxes and Motors	30
Figure 17 Jack Screw and Mitre Gear Box Distance.....	31
Figure 18 Schematic Diagram of Scissor Lift with common shaft	31
Figure 19 Scissor Lift Mechanism Driven by ACME Thread.....	32
Figure 20 Hydraulic Cylinder Pivot and Floor Mount	34
Figure 21 Jack Post.....	35
Figure 22 Deflection Plot of Flume Supported by Single Hydraulic Cylinder	36

Figure 23 Flume Side View with Component Details.....	36
Figure 24 Flume Structure End View.....	37
Figure 25 Framing Wood Intermediate Supports Shown in Flume Upper Section.....	39
Figure 26 PVC Floor Plate Deflection Finite Element Analysis.....	40
Figure 27 Top L Bracket to Retain Side Wall Plates	41
Figure 28 Vibratory Feeder	42
Figure 29 Vibratory Feeder with Rolling Stairs.....	43
Figure 30 Vibratory Feeder with Motorized Trolley Crane with Dump Box at Floor level	44
Figure 31 Vibratory Feeder with Dump Box Dumping into Hopper	45
Figure 32 Light Table and Sediment Trap Arrangement End View	46
Figure 33 Light Table Bottom Isometric View	47
Figure 34 Screw Conveyor Arrangement.....	48
Figure 35 Low Frequency Half Duplex Charge and Tag Response (Texas Instrument, 2004)	51
Figure 36 Typical reader components	51
Figure 37 Layout of Glass Transponder (Finkenzeller, 2010)	52
Figure 38 Transponder Reading Field With Stick and Gate Antenna (Texas Instrument, 2002).....	53
Figure 39 Range of 32 mm PIT tag with RI-ANT-S02 Ferrite Rod Antenna (Morhardt, et al., 2000)	54
Figure 40 Serial and TTL levels (RS-232 vs. TTL Serial Communication, 2010)	57
Figure 41 Schematic of connection between antenna, reader and data-logging calculator (Morhardt, Bishir, Handlin, & Mulder, 2000)	59
Figure 42 Typical Multiplexed System	60
Figure 43 Texas Instruments™ RI-MOD-TX8A multiplexer	61
Figure 44 RI-MOD-TX8A Schematic with RF Module and Controller	62
Figure 45 BioMark IS1001 Reader Module	63
Figure 46 Oregon RFID Multiplexer with Control Module, RF Module, and Data Logger	64

Figure 47 Servo Motor and PLC Schematic Diagram.....	69
Figure 48 Arduino Motion Control Schematic Diagram.....	70
Figure 49 Pulse Width Modulation (PWM, n.d.)	71
Figure 50 DC Motor with PLC Control Schematic Diagram.....	72
Figure 51 RFID Carriage Assembly	74
Figure 52 RFID Test Assembly.....	75
Figure 53 Detection Cloud with no steel shadowing.....	77
Figure 54 Minimum and Maximum Detection with no steel shadowing	78
Figure 55 Detection Cloud at steel seam of flume sections.....	80
Figure 56 Minimum and Maximum Detection at steel seam of flume sections	82
Figure 57 RFID Tag Location Traversing across width of flume	84
Figure 58 Centroid of Detection Area	85
Figure 59 Two Tag Detection at 3.05 m downstream with Lateral Separation.....	89
Figure 60 Two Tag Detection at 3.05 m downstream with Stream wise Separation	91
Figure 61 PLC Limit Switch and Output Layout	111
Figure 62 PLC Ladder Logic Program.....	114
Figure 63 PuTTY Startup Screen	118
Figure 64 PuTTY Serial line configuration.....	119

List of Tables

Table 1 Motivation for Tracer Studies adapted from (Schmidt & Ergenzinger, 1992).....	22
Table 2 Detection Range with RI-ANT G01E antenna and 23 mm transponders (Lauth & Papanicolaou, 2008)	54
Table 3 Detection Range with Aquartis and Flat Bed Antennas (Schneider, et al., 2010).....	55
Table 4 Bluetooth Device Transmitter Classes (Wright, n.d.)	58
Table 5 Itemized Costing of BioMark Multiplexing System for 12 Antennas.....	63
Table 6 Itemized Costing of Oregon RFID Multiplexing System for 12 Antennas	65
Table 7 Antenna Number, Position, and Angle.....	76
Table 8 Detection Range with no steel shadowing.....	77
Table 9 Minimum and Maximum Detection with no steel shadowing	79
Table 10 Detection Range at steel seam of flume sections	80
Table 11 Minimum and Maximum Detection at steel seam of flume sections	83
Table 12 Predicted RFID Tag Lateral Location.....	86
Table 13 Minimum, Maximum and Average Streamwise Detection Location Across Flume.....	87
Table 14 Minimum, Maximum, and Average Detection for 2 tags with Lateral Spacing	90
Table 15 Minimum, Maximum, and Average Detection for 2 tags with Stream Wise Spacing	92
Table 16 PLC Input and Output List	111
Table 17 PLC Logic Elements used in Ladder Logic	112
Table 18 RFID Carriage Mechanical Drive Components from McMaster Carr	120

Chapter 1

Introduction

River engineering is increasingly concerned with the dynamics of the sediment being conveyed by the river rather than principally focusing on the problem of flow conveyance. This interest is motivated by a desire for improved control of erosion and sediment aggradation, improved flood management, and enhanced recreational and ecological value of the channels. Stream restoration and fish habitat enhancement (Imhof, et al., 1996) requires understanding of the sediment transport mechanics over the full range of the flow regime and sediment characteristics exposed to the channel. The predominate channels evaluated in river engineering are alluvial channels which have their boundaries formed by loose sediment deposited by previous floods or glacial activity.

The mechanics of sediment transport can be studied in both natural and artificial channels, referred to as flumes. Studies in natural channels have improved our awareness of channel forming processes and provided us with general trends correlating variables such as channel slope, the shape of the flood hydrograph, sediment sizing, and vegetation, with channel characteristics such as width, depth, pool-riffle spacing, and sediment transport capacity. This knowledge enables the design of channels based on comparison with similar features and conditions found in other rivers. Designing by comparison may work when there are sufficient studies on comparable channels, but improved understanding of the mechanics driving the river forming processes would provide more flexibility for practitioners. In natural channels, due to rapid change of the variables affecting sediment transport during floods, it is often not feasible to obtain data on turbulent activity and local flow conditions which are driving the movement of individual clasts of sediment, rather only overall flow conditions and sediment transport rates can be observed. Flume based studies are able to complement the data obtained from the studies in natural channels by precisely controlling and monitoring variables such as flow rates, sediment supply, channel form, and bed roughness and slope to simulate conditions occurring in natural environments.

While flume studies exist which look specifically at a few variables, there is a need for flumes which incorporate accurate flow control with sediment supply and tracking. The tracking of sediment movement in flumes is commonly done by sieve analysis of discharge from the sediment trap, photographic or manual analysis of the bed after the flume is drained, or manually sweeping the bed for the position of tracer stones after a test run. All of these methods result in a significant time delay between the sediment transport event and the collection of data quantifying the sediment transport.

This delay leaves questions about the hydraulic conditions at the time of entrainment and steps and/or pauses during transport.

The goal of this research is to develop a flume with the capacity to accurately measure sediment inputs, transport, and export in real time. This will be accomplished by automating the sediment supply, using a sediment trap with a light table to monitor sediment leaving the flume, and implementing an radio frequency identification (RFID) sediment tracking system to provide real time tracking of the movement of individual clasts over the course of an experiment.

The structure of this thesis consists of a literature review, documentation of the design of flume and RFID system, and experimental results. In Chapter 2, literature of bedload sediment transport measurement techniques used both in field and flume studies is reviewed to develop a perspective of the types of data which can be obtained in using a range of measurement techniques along with the limitations inherent in these methods. This section finishes with a review of studies that used RFID tracking for sediment transport monitoring to provide a context for the current study. The methodological advances that represent the most significant contributions of this thesis are described in Chapters 3 and 4. In Chapter 3, the design process involved in developing the flume is documented. This involved examining the design options considered for tilting mechanisms and presenting the details of flume structure and floor design. The design of the proposed sediment trap integrated with light table and sediment supply system is also presented since these components needed to be considered when designing the flume even though they will be added to the flume at a later date. The key innovation from the current work is the design of an RFID carriage to allow the real time tracking of sediment tracer particles as detailed in Chapter 4. This chapter explores relevant aspects of the technology, the techniques that have been employed to use RFID for sediment tracking in other studies, and the system employed in the flume. Chapter 5 documents preliminary results from RFID tracking tests and describes a tag positioning algorithm. Chapter 6 presents the conclusions of the findings obtained in this research.

Chapter 2

Literature Review

The term “sediment transport” refers to all components of material, such as chemical precipitates, silt, sand, gravel, and cobble (Mcgee, 1908) that the movement of water conveys down a channel. While chemical precipitates travel as dissolved solution, and silt and clays are generally transported in suspension, bedload sediment composed of sand, gravel, and cobble is typically transported down the channel by sliding, rolling, and saltation (i.e. short hops) with only occasional moments where the particles are elevated off the bed. The bedload sediment is an significant components of the total transported sediment load because it typically defines the boundary of an alluvial channel, with changes to the bedload flux potentially leading to erosion (decrease in local elevation) or aggradation (increase in local elevation). Earlier bedload sediment transport theories assumed that particles comprising the channel bed move together as a mass or moving carpet similar to a land slide but at a slower rate. Subsequent experimentation and observation has led to the conclusion that this only happens in extreme circumstances (Leopold, et al., 1964). Rather, transport occurs as a series of movement and rest periods (Schmidt & Ergenzinger, 1992), with strong spatial variability due to bed and hydraulic heterogeneity, and differences between size classes (i.e. fractional or size-dependent transport). This has motivated research on how individual particles are moving with the characterization of transport not just limited to the transport rates of different size fractions (Wilcock & McArdell, 1993), but also details of entrainment (Diplas, et al., 2008), movement, deposition and rest between periods of movement (Habersack, 2001).

This review will look at a range of sediment transport measurement techniques with the goal of providing a context for RFID sediment transport measurement techniques in fluvial geomorphology research. This chapter is organized into four sections: 1. Direct transport measurement, 2. Indirect transport measurements, 3. Tracers, 4. RFID Tracers.

Conceptually, the most basic sediment measurement technique is to capture either all or a sample of the load and weigh it. This approach is referred to herein as direct measurement. In many instances, this may be impractical or undesirable and so a number of indirect techniques have been developed that use some proxy of sediment transport to estimate load and further details of the load such as the size distribution and velocity of the clasts. Tracers are also used to sample individual paths and can be integrated to estimate the total load. This review describes applications of various sediment

transport measurement techniques. While the review is not exhaustive, it provides an understanding of the types of data which can and cannot be obtained from the different techniques, showing how RFID tracer measurements complement other measurement techniques in deepening our understanding sediment transport mechanics.

2.1 Direct Measurements

Direct measurements refer to the physical capture of the sediment. It can be divided into two general categories: integrated sampling methods that capture all the bedload sediment transported down the channel, and localized methods that capture the bedload material being transported at a specific location and for a specific period of time from which generalized transport rates can be inferred.

2.1.1 Integrated Direct Sampling Methods

2.1.1.1 Bedload Traps

Integrated sampling methods are commonly used in flumes since it is preferential to remove all the bedload sediment at the flume discharge to ensure it does not enter the tail water tank and damage the pump. Integrated sampling is not as common in natural channels since it requires excavation of the channel to install the sampler and an effective method needs to be developed to remove sediment from the sampler. The most notable exceptions to this are Leopold and Emmett's (1997) bedload trap incorporating a conveyor belt for sediment removal and Lenzi et al.'s (1990) use of sediment trap along with ultrasonic gauges to quantify the height and volume of sediment transported during a flood event.

Sediment traps being used in scale models of river were being created by 1920 in laboratories with sufficient predictive quality to establish a standard for using scale models in sediment transport studies (Graf, 1984). Among the first of these were Hubert Engels (1854-1945) and Theodor Rehbock (1864-1950) in Germany.

In America, some of the early work was being conducted by Gilbert and Murphy (1914). This study was motivated in part by the controversy surrounding hydraulic gold mining in the Sacramento and Yuba rivers that fed down to the San Francisco Bay. Debris waves were being created by the dredging and sluicing of gravel to extract the gold, disrupting the downstream waterways, and creating a need for a quantitative understand of the sediment transport mechanics. Gilbert and

Murphy (1914) created a wooden trough flume at the University of California at Berkeley 9.6 m long and 0.6 m wide as shown in Figure 1. The height of it was tapered such that it was 0.5 m high at the head tank (A) and 0.3 m high at the tail water tank (C). The head tank remained stationary while the flume, which was connected to the head tank by a flexible rubber connection, could pivot on semi-cylindrical hinge. Flow was controlled using a gate at the head tank. A sediment trap (B) was a cross trough 3.4 m wide, 0.8 m in the stream-wise direction, and 1 m deep with the experimental flume having a full width opening ovetop of the sediment trap, allowing sediment to drop into the cross trough. The walls of the sediment trap trough were close to the same height as the experimental flume allowing an equilibrium water level to be maintain between the flume and cross trough so there would be no net water flow into the cross trough, only sediment dropping out of the flume.

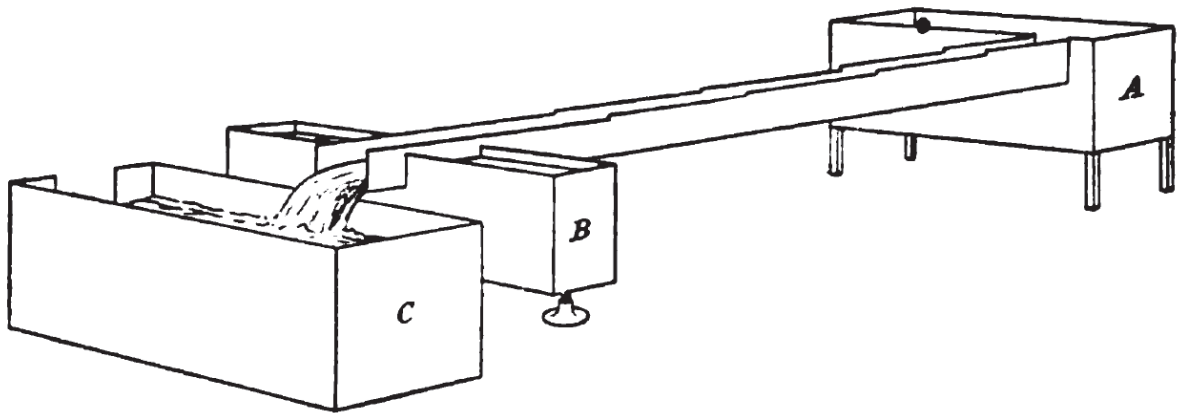


Figure 1: Diagrammatic view of shorter experimental trough (Gilbert & Murphy, 1914)

This flume facilitated the evaluation of the effects of slope, discharge, and sediment size on stream capacity. The slope effect was determined by feeding the sediment of a specific coarseness into a controlled stream with specific width and depth. Over time, the slope of the stream would adjust to create the transport capacity required to maintain equilibrium. They were able to show that at a negligible slope, the stream had no sediment transport capacity, while increased slope lead to a proportional increase in stream capacity as:

$$(S - \sigma)^n$$

where S is the slope of the stream, σ is the competent slope, and n was an experimentally determined value ranging from 0.93 to 2.37 with larger values for smaller discharges or coarser sediment. The discharge was determined to control the transport capacity following a similar power relation as:

$$(Q - \kappa)^o$$

where κ is the competent discharge of the chosen slope and grade of sediment, Q is the discharge, and o is an experimentally determined coefficient with a value between 0.81 and 1.24. Larger coefficients (o) were associated with smaller slopes and coarser debris. In a similar manner, the stream capacity was affected by sediment fineness as follows:

$$(F - \psi)^p$$

where F is the degree of fineness, ψ is the competent fineness, and p is an experimentally determined coefficient with a value between 0.5 and 0.62.

These three relationships incorporate the concept of the stream capacity being a function of the driving factors (slope, discharge, sediment fineness) compared with a threshold value, a concept that is seen in DuBoy type critical shear stress formulas and Schoklitsch type critical discharge formulas (Graf, 1984). Gilbert also postulated that transport rate is correlated with stream velocity. His analysis of sediment transport also introduced the concept of form factor: the depth to width ratio. In addition to the quantitative findings, Gilbert also speculated that the transport capacity differs based on whether the river stage is rising or falling, with a rising river causing scour of the deeper pools.

Gilbert was the primary proponent of the graded river concept, in which the supply of energy to a channel is balance with slope adjustment by the power consumed to move the water and sediment. When this balance is maintained, the channel neither aggrades nor degrades. This concept was further developed by Kesseli (1941) and (Mackin, 1948). The discussion of stream power initiated by Gilbert was further developed by Bagnold (1966) and Yang (1976) as a method to prediction sediment transport rates. The experimental data obtained by Gilbert and Murphy were the first substantial set of readily available data on sediment transport. Sediment transport analysis using bedload traps have continued to be a keystone in the development of sediment transport theories.

2.1.1.2 Screened Gates and Baskets on Flume

Continued research in sediment transport dynamics revealed that the instantaneous rate of sediment transport varies greatly from the average rate. Hubbell (1964) documented cyclical fluctuations in transport rate ranging between 3 to 20 minutes as shown in the Figure 2 and Figure 3 using bedload samplers resting on the channel bed.

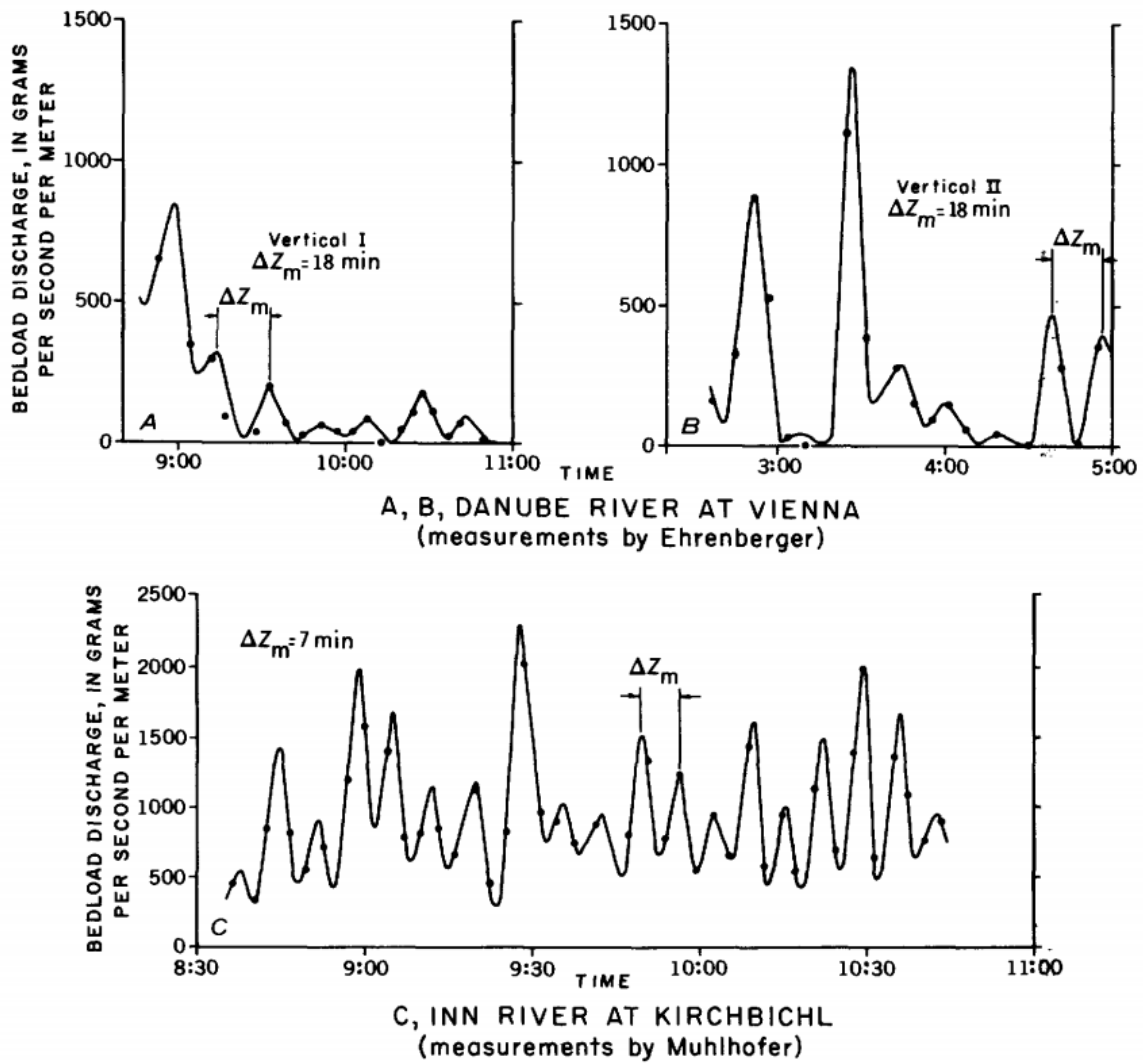


Figure 2 Variations of Sampling bedload discharge documented by Ehrenberger in 1931 (as cited in Hubbell D. W., 1964)

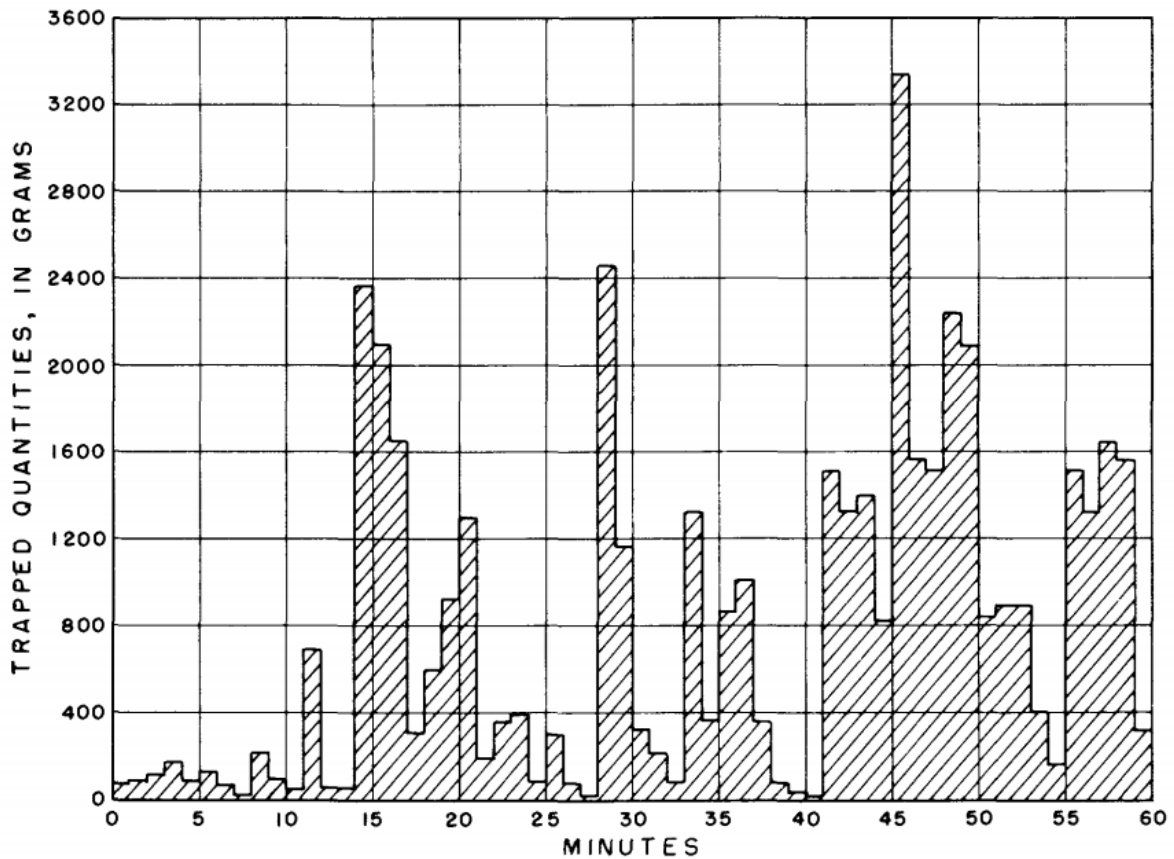


Figure 3 Results of Bedload collections during one hour in a laboratory flume documented by Einstein in 1931 (as cited in Hubbell D. W., 1964)

These variations in transport rate indicated that instantaneous transport rates do not accurately reflect the average transport rate and any method of collecting data being used to determine the average rate must provide the ability to obtain data over a substantial period of time.

Fluctuations in sediment transport rates were observed by Kuhnle and Southard (1988) by using a screened gate at the discharge of a flume which would collect sediment while allowing the water to flow through. This gate would then be opened every 30 seconds to allow the sediment to be flushed onto a screened basket. A new basket would be put in for every flush, allowing for 30 second sampling of the transport rate.

Visual observation of the flume through a transparent sidewall indicated the periodic formation of jams with a decreased slope upstream of the jam and an increased slope downstream. As the jam formed, sediment would accumulate upstream of the jam and degrade downstream of the jam resulting in a drop in sediment discharging the flume. Upon breakup of the jam, a sediment wave would be created resulting in a spike in the transport rate plot (Figure 4).

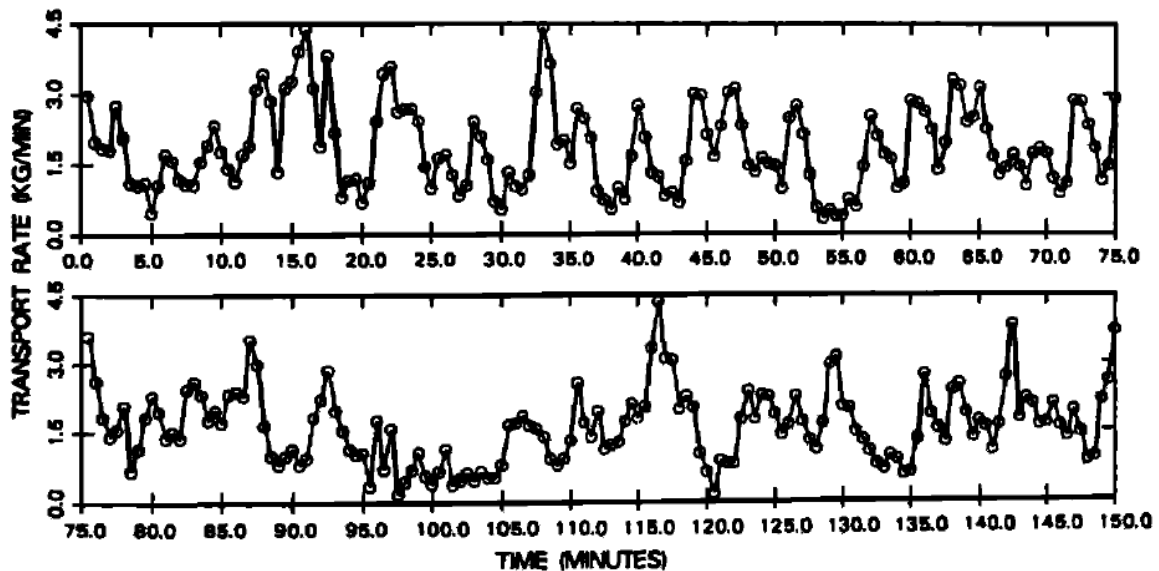


Figure 4 Total Transport Rate Verses Time (Kuhnle & Southard, 1988)

Screen and basket sediment transport measurements enable quantitative analysis of the dynamic processes occurring as a channel continually adjusts. However, this measurement approach is limited because it is labour intensive, the resolution of the data is limited to the frequency at which baskets can be changed. The full effects of the jamming are moderated by the downstream sediment transport activity because the sediment transport is being measured at the flume discharge rather than at the location of jamming.

2.1.1.3 Slot or Pit Samplers

By creating a pit below the channel bed, and placing a plate with a lateral slot over the pit, the transported bedload can be trapped in the pit while the water moves over the top. Pit samplers have been used to determine the grain size distribution of the bed load being transported by excavating and analyzing the contents of the pit, and also used to determine the bedload discharge rate by measuring the time require to fill the pit (Hubbell D. W., 1964). Collection efficiencies approaching 100% can

be achieved if the width of the slot is between 100 to 200 times the size of the clasts being captured. The pit samplers are ideal for ephemeral channels where it is often not feasible to supply personnel to monitor the sediment being transported during the flood event due to the sporadic and flashy nature of floods since the pit samplers can be installed during dry season, and then inspected after a flood to determine the quantity of bedload sediment transported.

One of the drawbacks of the original pit type samplers is that they only provide time averaged sediment transport data. The Birkbeck bedload sampler (Reid, et al., 1980) overcame this limitation by equipping a pit-trap sampler with a water filled pressure pillow under a free moving stainless steel box located in a larger concrete pit (see Figure 5). As the stainless steel box fills with sediment, the increased pressure in the pillow is read by a pressure transducer connected to a data-logger. The pressure in a stilling well adjacent to the pit-traps is also continuously recorded to indicate the stage of the channel and infer the flow rate and average shear stress. The difference between the pressure from the stilling well, and the pressure recorded from the pressure pillows indicates the load of sediment accumulated in the stainless steel boxes. A second pressure transducer located upstream of the stilling well can also be used to determine the water surface slope used to calculate the bed shear stress.

In the Turkey Brook demonstration (Reid, et al., 1980) and the Nehal Yatir sediment monitoring program (Reid, et al., 1995), banks of 3 bedload samplers were installed across the central portion of the channel cross section while a bank of 5 samplers were installed in the Nehal Eshtomoa study (Powell, et al., 2001) providing an indication of the transport rate in the channel center compared with the channel margins. By removing the sampled material in layers from the sampler, grain size distribution over the course of the flood can be inferred (Powell, et al., 2001) by correlating the layer with the data logged pressure on the pillow and water stage, although the layers are not perfectly level as the sampler tends to fill with a ridge under the slot. Some limitations of the Birback sampler are that they have the potential to fill up part way through a flood event, require manually emptying between floods, and have limited lateral resolution.

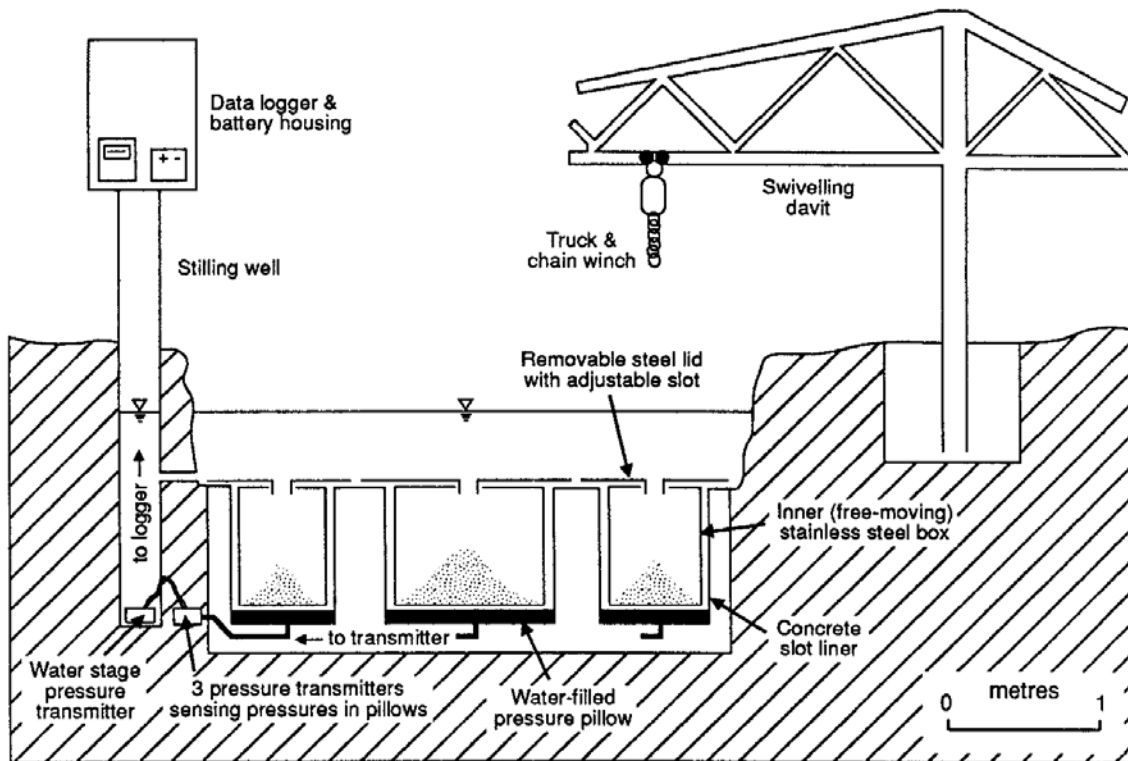


Figure 5 Schematic diagram of the Birkbeck slot-sampler (Reid, et al., 1995)

2.1.2 Localized Direct Sampling Methods

While integrated bulk sampling is most advantageous in a flume, obtaining localized data on the bulk transport in a natural channel provides an indication of the transport rate while resulting in less channel disruption and installation time. The most extensively used localized bulk bedload transport sampling instrument for field applications is the Helley-Smith Bedload sampler as shown in Figure 6 (Edwards & Glysson, 1988). Helley and Smith (1971) developed their bedload sampler to enable a single person to lower the sampler into the water and hold its position during flood events. Since suspended sediment samplers cover the range down to 0.3 feet above the bed, the Helley-Smith was developed to measure from the bed up to 0.3 feet. The Helley-Smith is predominately designed for use in grain sizes ranging from 0.5 to 16 mm (Helley & Smith, 1971). Refinement of the design has enable bedload sampling efficiencies to approach 100% when compared with a continuously excavated bedload trap (Emmett, 1980).

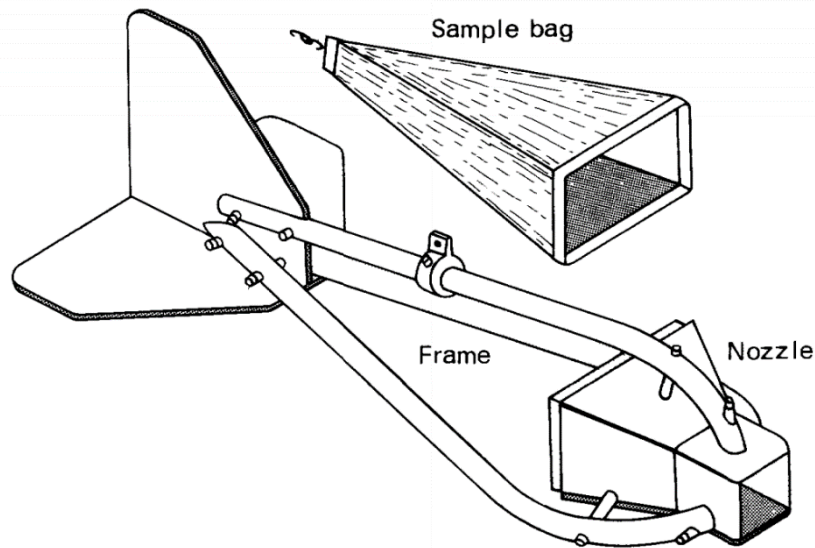


Figure 6 Helley-Smith Bedload Sampler (Emmett, 1980)

To facilitate lowering the sampler to the bed during high flow conditions, cable stays which are anchored upstream are used to secure the sampler so it is not swept downstream. These cables develop high tensile load when the sampler is exposed to the high velocity water at the water surface. As the sampler is lowered, the velocity decreases, reducing the drag force on the sampler such that by the time the sampler is on the bed, it has moved forward. Care must be taken that the sampler does not scoop up bed material as it moves forward to an equilibrium position (Hubbell D. W., 1964). The sampler also can fill up too quickly in high flow conditions which requires repeated sampling at the same location to obtain representative data to account for the statistical variations in transport rate (Bunte, et al., 2008).

Bunte et al. (2008) developed a sampler to address the problems inherent with using cable stays and unintentionally scooping bed material into the trap with their sampler which uses stakes secured into the bed along with an aluminum ground plate (Figure 7) and a larger collection bag to extend the sampling period between sampler replacement.

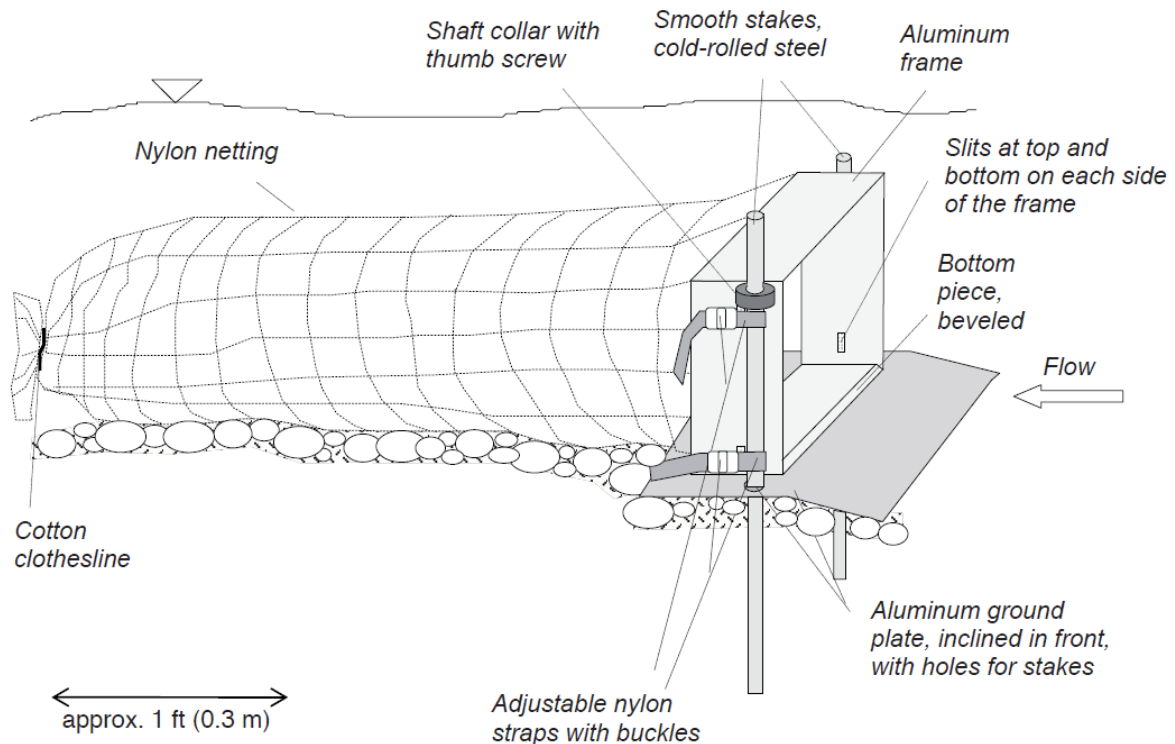


Figure 7 Bunte Bedload Sampler (Bunte, et al., 2008)

While the Bunte Sampler minimizes disturbances to the bed experienced by the Helley-Smith sampler, the presence of the sampler disrupts the flow patterns in the channel, altering the sediment transport characteristics. Also, since sampler does not extend across the entire width of the channel but usually placed in the location where the highest sediment transport is anticipated, estimates of the bedload transport rate over the entire channel may not be representative.

2.2 Indirect Transport Measurements

While direct transport measurements help to understand overall sediment transport phenomena by capturing all the sediment, it is often not feasible to perform this either due to the depth of the channel, the resulting disturbance, or the lack of an appropriate method of processing the sediment that is removed from the channel. Bulk transport measurements are also imprecise because they capture the whole load with little information about the behavior of individual fractions and individual data. A number of indirect transport measurements have been developed that provide

additional detail on size fractions or individual clast motion information while avoiding some of the shortcomings of direct transport measurement methods.

2.2.1 Motion Picture Photography

Motion picture analysis provides a method of instantaneously observing sediment transport. The effectiveness of this technique for predicting bedload rates were shown by Drake, et al. (1988), who corroborated the results with transport rates obtained using a bedload sampler. By obtaining instantaneous sediment transport data, Drake et al. (1988) facilitated refinement of the sediment transport theories from those based on a competence functions (Buffington & Montgomery, 1997) such as critical shear (Shields, 1936; Meyer-Peter & Müller, 1948) or stream power (Bagnold, 1966) to theories based on the turbulence dominated stochastic nature (Einstein, 1950) of bedload transport. The transport rates were measured in a natural stream in Wyoming where flow was primarily provided by snowmelt from the Wind River Mountains creating a stable flow regime. This flow could be further managed by an upstream control gate to a diversion and an intake for an irrigation ditch 45 m downstream. Plan view motion picture photography was obtained with the camera mounted on a temporary bridge and the camera pointed down into a glass bottomed box on the water surface. After analyzing the motion pictures, the modes of entrainment, measurement of the amount of displacement, and conditions for distraintment were quantified. The transport rate was calculated by observing the number of particles that cross a 21 cm section in 30 seconds.

In addition to providing detailed information on individual particle motion, the motion picture photography enable quantification of the effects on sediment transport of sweep events, these are periodic relatively fast streamwise flow events angled towards the bed which have previously been observed in laboratory conditions investigating the dynamics of the turbulent boundary layer (Kline, et al., 1967; Corino & Brodkey, 1969; Grass, 1971). Analysis of the films revealing that 70% of the bedload transport was occurring in the sweep events which occur less than 10% of the time.

Motion picture analysis techniques continue to be refined (Roseberry, et al., 2012), with higher spatial and time resolution along with incorporation of image analysis software such as Image J (National Institute of Health) for marking the centroid of particles in successive frames. This enhances the accuracy of the analysis while still requiring manual analysis of the images.

2.2.2 Painted Sediment

Wilcock and McArdell (1993) investigated the transport rate of different size fractions under partial mobility conditions where only certain of the size fractions are mobile by painting each size fraction a different colour. Their study was motivated by the recognition that the transport rate of different size classes is affected by the size distribution of sediments on the surface of the bed rather than the entire depth of the bed. The range of partial transport, where flow rates are sufficient for incipient motion for some of the grains, but all the grain are not regularly mobilized (referred to as full mobility), was an area that Wilcock and McArdell recognized had not been well researched. To accurately model natural channel fraction transport rates, conditions needed to be created in the flume which enabled the natural selection process for certain fractions to preferentially occur on the bed surface. This was achieved by using a recirculating water and sediment flume. By recirculating the sediment, only the mobile sediment was being re-introduced into the flume. Wilcock and McArdell argue that by re-supplying the flume with only the sediment fractions which are mobile, a steady state condition could be achieved. The recirculating flume was used by many of the key studies (Parker & Wilcock, 1993; Wilcock & McArdell, 1997; Wilcock et al. 2001) to gain insight into factional transport rates and bed pavement. Implicit in their argument is the assumption that the channel is only obtaining sediment feed from the bed of the alluvial channel.

Having each size fraction of sediment painted a different colour improved the accuracy of observing the bed surface size fraction over analysis of bed surface grain size distribution with unpainted sediment since unpainted sediment observations can be biased by partially covered grains and grain orientation. The analysis time for unpainted sediment is also longer as the boundary for each grain needs to be identified and the grain size measured. Even through it is time consuming to paint the grains, the analysis was more efficient and repeatable.

The bed surface size fraction was analyzed by draining the bed at the end of a run and photographing the bed. Overlaid on the photographs were two separate 4 cm x 4 cm grids that were offset by 2 cm in the downstream and cross stream direction as shown in Figure 8 to achieve a diagonal grid spacing of 2.8 cm. The colour of sediment at each grid intersection was recorded and the concentration of each size fraction on the bed surface was calculated.

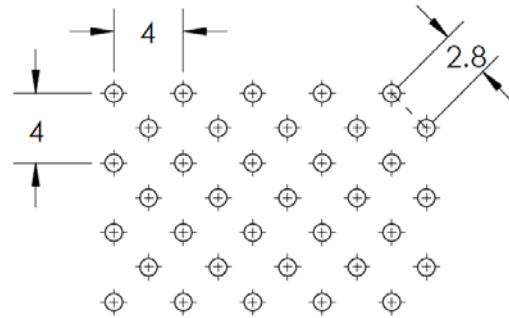


Figure 8 Pixel spacing grid for the measurement of mean surface grain size fraction

Using photographic analysis of bed sediment size along with sieve analysis of sediment discharging the flume, Wilcock and McArde (1993; 1997) were able to develop a set of data which coupled fractional transport rates with bed surface size distribution and flow rate. They were able to establish a reference shear stress at which incipient motion occurred for each size fraction on beds with poorly sorted grain size distribution. Their results supported field observations of small size fractions being transported at lower discharges while all fractions are mobilized at higher discharges (Hassan & Church, 2001). They were able to identify two regimes of transport occurring: smaller sizes having full mobility while the larger sizes have partial mobility with the size delineating full mobility from partial mobility increasing with higher discharges.

While the painted clasts enable photographic analysis of the bed surface to determine size distribution, the movement of individual clasts could not be tracked with this method. The requirement to drain the flume each time the bed was photographed disturbs flow and sediment transport mechanics, effectively creating a rising, steady state, and falling hydrograph for each run – eliminating the ability to distinguish if the rising or falling leg of the hydrograph have the largest contribution to sediment transport. This technique is also not applicable to long term experiments due to the paint wearing off.

2.2.3 Video Analysis of Light Table

Developments in sediment transport measurements have shown the high variability in transport rates (Hubbell D. W., 1964; Drake, et al., 1988; Kuhnle & Southard, 1988). The motion picture analysis (Drake, et al., 1988) was able to identify the variability, but the manual analysis and short amount of data collected minimized the long term viability. Screened Gate and Sieve analyses (Kuhnle & Southard, 1988) enabled continuous measurement of the variability, but the time step is limited to the

30 seconds required to change baskets. New developments in video image analysis capabilities of LabView™ software (National Instruments, 2005), coupled with improved computational speed and camera technology has enable continuous video based analysis of sediment using a light table. LabView™ contains a suite of video analysis tools to isolate an individual piece of sediment from its background by increasing the contrast between the sediment and the background then applying filters and thresholds to delineate the boundary of the sediment. The size of the delineated sediment can then be measured by counting the pixels across from one side to the other. This technology was employed by Zimmerman et.al (2008) on the discharge of a flume shown in Figure 9.

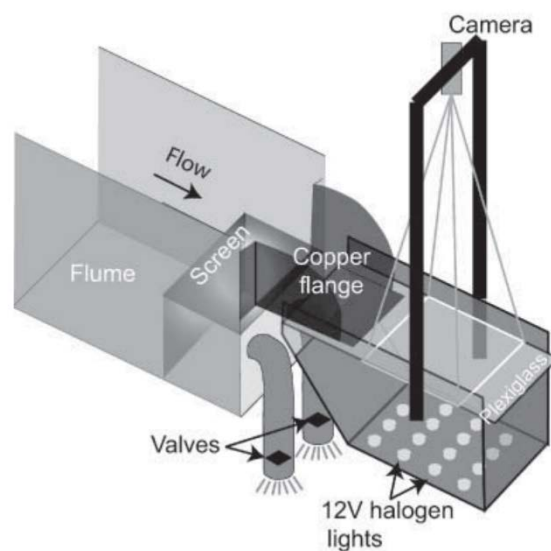


Figure 9 Flume Outlet with Light Table and Camera (Zimmermann, et al., 2008)

In this flume, the bed of flume is lower than the screen area which is used to divert excess flow away from the light table. By having an upward step at the end the flume, this creates a location for sediment to accumulate rather than be flushed out, modifying the sediment transport rate. Discussion of this step was not present in the paper, while it primarily focused on calibration of the light table against sieve analysis, rather than using the light table to demonstrating sediment transport measurements representative of a field site. The sediment transport rate was determined by identifying the size and number of particles on the light table combined with calculating the velocity based on tracking the movement of the largest particles for successive images. The quantity of sediment transported tended to be overestimated by 39% when compared with sieve analysis but the grain size distribution matched the results from the sieve analysis. With further design refinement,

light table sediment transport analysis could provide the ability to continuously monitor both the quantity of sediment being discharged and the fractional distribution.

2.2.4 Acoustic Doppler Current Profiler Bedload Velocity

A method to observe the sediment transport activity at the location of interest is to use the bottom tracking feature of an acoustic Doppler current profile (ADP) to determine apparent bed velocity. Such a device is typically used to measure water velocity by emitting a series of acoustic pulses and then measuring the Doppler shifted pulses reflected back from particles carried along with the water. Rennie et al. (2002) showed that a similar principal could be used to calculate the velocity of sediment moving along the bed by reflecting the acoustic waves off the channel bed.

The ADP divides the measurement area into cells which it determines based on the return time for the backscatter (reflected) signal. The bottom is determined by the ADP detecting a marked increase in the backscatter signal indicating a higher density material is reflecting more acoustic energy back to the ADP. If the backscatter is coming off a sloping or irregular surface, then the travel time will not be consistent for all the waves bouncing off the bottom, resulting in the ADP generating a poor signal quality on the bottom velocity. Thus, bottom tracking works best for a perfectly flat sand beds rather than beds exhibiting dunes or other irregular features.

Bedload measurements using an ADP have several advantages over traditional pits or Helley Smith samplers. They provide the ability to measure bed velocity at locations where it is unfeasible to install a sediment trap or pit, with measurement obtainable on a boat traversing the channel. The ADP also does not need to be anchored by cables since ADPs commonly have a DGPS features or can be coupled with an external real-time kinematic DGPS to provide position information and the ability to navigate the boat to maintain a stationary position.

Gravel bed-load transport data is erratic (Rennie, et al., 2002; Rennie, Millar, & Church, 2002) requiring sampling intervals in the order of 30 minutes to obtain reliable gravel transport results. This method also creates poor quality data over complex topography. Bottom tracking with the SonTek ADP is limited to bottom depths ranging from between 2m to 8 m. Since only the bed surface velocity is being obtained, transport rates can only be determined if the bed conditions are recreated in a flume to establish a rating curve.

2.2.5 Piezoelectric bedload impact sensors

Vibration energy created by moving sediment impacting a sensor has also been used to determine the quantity of sediment being transported. The effectiveness of this method of measurement is demonstrated in the Erlenbach stream by Rickenmann and McArdell (2007) with their Piezoelectric bedload impact sensors (PBIS) study. The Erlenbach stream is a step pool stream with sediment ranging in size from silt to boulders several meters in diameter. Piezoelectric crystals were employed due to the high voltage that can be generated from moderate levels of compressive load. The crystals were mounted to the underside of 0.36 m long by 0.497 m wide by 0.015 m thick steel plates which in turn were mounted on acoustically isolating elastomers (see Figure 10), with an array of sensors mounted across the width of the channel (Figure 11). The sensors were mounted in a concrete check dam immediately upstream of a sediment retention basin.

The sensors were set up to record an impact event every time the piezoelectric crystal created a voltage exceeding 0.2 V. Through experimentation, it was determined that this voltage correlates with quartz particles 10 to 30 mm ϕ impacting the plate, enabling transport of sediment exceeding the median grain size to be recorded. Calibration runs were conducted in an experimental flume to correlate the quantity of impacts to the level of sediment transport. Ongoing evaluation of the effectiveness of the PBIS calibration was obtained by collecting the sediment from the sediment retention basin downstream of the PBIS array revealing an accuracy within the range of 1.5 to 2 times the actual sediment transported.

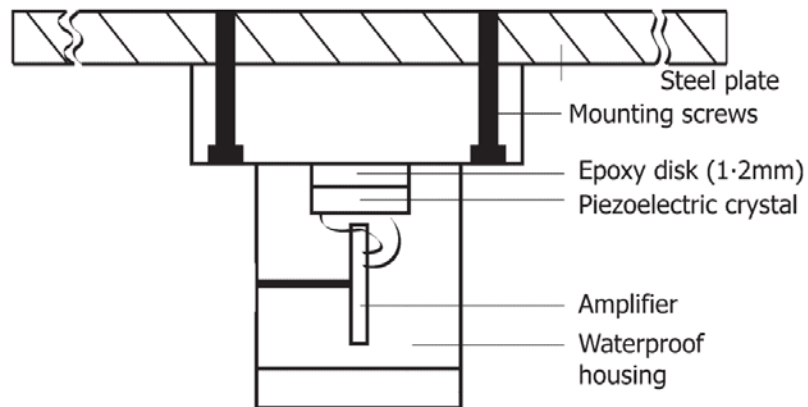


Figure 10 Schematic Diagram of PBIS (Rickenmann & McArdell, 2007)

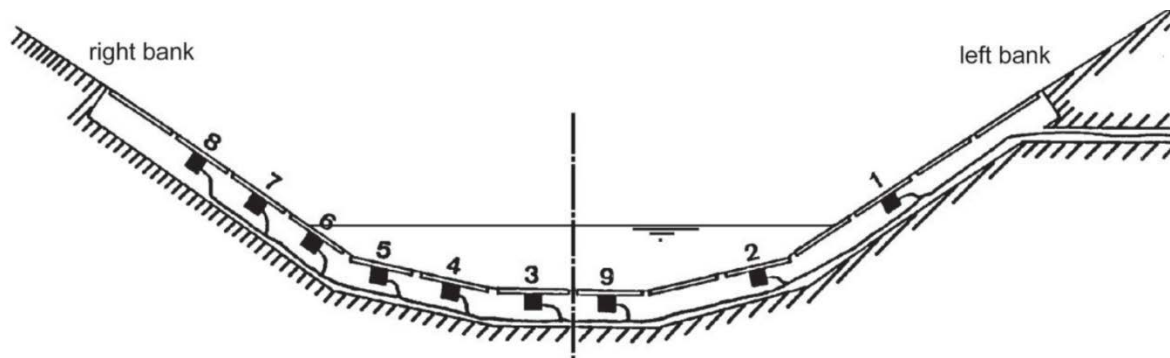


Figure 11 Arrangement of PBIS array across channel width (Rickenmann & McArdell, 2007)

Predicted sediment transport based on classical formulas tend to vary by orders of magnitude from those actually observed in mountain streams, making an application such as PBIS beneficial to obtain an indication quantity of sediment being transported. The main drawback of the system is its high reliance on calibration which is affected by the different modes of bedload motion and grain size distribution.

2.3 Tracers

Sediment transport theories have progressed from DuBoys 1879 theory (as cited in Graf, 1984) that assume movement of the bed occurs in layers or a like a highly viscous slurry to stochastic theories that look at the transport rate as the net result of the movement of individual clasts (Einstein, 1950), each with their own step size and rest periods with strong spatial and temporal variability (Hassan, et al., 1991; Schmidt & Ergenzinger, 1992) due to bed and hydraulic heterogeneity (Kironoto & Graf, 1995; MacVicar & Roy, 2007) and difference in size classes (Wilcock & McArdell, 1993)(i.e. fractional or size dependent transport). As fluvial hydraulics and sediment transport data have been refined since Einstein's work (Kline, et al., 1967; Diplas, et al., 2010), the importance of obtaining data on the movement of individual clasts to refine stochastic models of sediment transport have increased.

One of the methods of tracking the movement of individual clasts is to attach tracers to the clasts that allow monitoring of their movement over time. This enables sediment transport rates to be estimated without physically removing the stones from the channel bed while tracing the movement of traced clast amongst untraced clasts. This section will explore methods of measuring sediment transport based on applying radioactive, magnetic, iron, and RFID tracers.

2.3.1 Radioactive tracers on sand

Data has been obtained on individual particle step lengths using radioactive tracers by Hubbell and Sayre (1964) to characterize the step length and step size of individual grains of sand and also as a basis for determining bulk transport rates. The primary experiments were carried out in the North Loup River which is predominately groundwater fed with a very consistent flow regime. The study reach was a straight section 550 m long, 15 m wide, with dunes 0.4 m deep and 3.7 m long, and with an average depth of 0.8 m and slope of 0.00083. The median grain size was 0.29 mm. Natural sand was labeled with Iridium-192 and laid down in a line across the width of the river. Secondary experiments were conducted in flumes using a similar technique.

Since the labeled sand was all tagged with the same radioactive isotope, they were not able to uniquely track the movement of each grain, rather they were able to evaluate the change in concentration of radioactive particles down the length of the river. For six days subsequent to seeding the radioactive particles in the river, the riverbed was scanned and radioactive concentrations were mapped. Based on the radioactive concentration distribution downstream from the source on subsequent days, Hubbell and Sayre postulated that the step length for the movement of each grain was exponentially distributed with a Poisson distribution representing the concentration of radioactive particles downstream from the seeding location as time elapsed. The data acquired on grain step size and downstream concentration enabled Einstein's (1950) probability model to be refined with empirically obtained step data rather than relying on bulk transport data Einstein originally used in developing his equations.

In addition to characterizing the movement of individual grains, Hubbell and Sayre used radioactive concentration data to quantify the mass of sediment transported by estimating depth of sediment which was actively being transported, referred to as the active layer. The active layer estimations were done in three ways: firstly by evaluating the dune patterns and using the difference between the deepest troughs and the mean bed surface level to determine an effective depth; secondly by measuring the depth of radioactive particles on the days subsequent to seeding to quantify the amount of vertical mixing indicating the active depth; and thirdly by the ratio of the weight of the tracer particles released to the product of the channel bed width and area under the concentration distribution curve. The estimated sediment transport rate using the combination of the three active layer methods was within 36% of the rate that would have been estimated using Einstein's method, establishing the value of tracing individual grains in sediment transport research.

2.3.2 Magnetic and Iron and Radio Tracers

While radioactive tracers laid the groundwork for tracking individual clasts, the use of radioactive substances in natural channels possess environmental risks. Research in the movement of individual clasts progressed with using magnetic, iron, and radio transmitter tracking. Schmidt and Ergenzinger (1992) identified the motivation for tracking individual clasts as laid out in Table 1. In addition to obtaining detailed information on individual clast movement, Haschenburger and Church's (1998) objective in using tracers was to quantify transport rates in floods in a mountain stream where portable sediment samplers and pit type traps are not applicable.

Problem Investigated	Tracer Technique¹
Moment of Transport initiation and termination	PETSY
Selectivity of initial movement	PETSY
Travel lengths of individual particles	FETT, MATT, PETSY
Influence of particle shape on travel length and transport probability	MATT
Influence of bed topography on travel length and transport probability	MATT
Selectivity of transport or equal mobility	FETT, MATT, PETSY
Length of individual steps	PETSY
Duration of rest period and times of motion	PETSY
Transport velocities	PETSY
Pathways of individual particles	PETSY
Spatial distribution of particles from point sources	FETT, MATT
Most frequent position of sedimentation	FETT, MATT, PETSY
Simulation of particle distribution from point source	PETSY

Note 1: FETT = Ferruginous Tracer Technique, MATT = Magnetic Tracer Technique, PETSY = Pebble Transmitter System

Table 1 Motivation for Tracer Studies adapted from (Schmidt & Ergenzinger, 1992)

The methods used to track the movement of individual clasts by Schmidt and Ergenzinger (1992) were to insert iron cores in 278 natural clasts; fabricate 480 colored concrete clasts with magnetic tracers shaped spherically, ellipsoidal, platy and elongated; and insert radio transmitters in 7 natural clasts with the tracer clasts implanted in a step pool natural channel. Once the radio transmitter clasts moved beyond the study reach, they were redeployed upstream of the tracking area. The iron and magnetic tracers were tracked after the flood events while the radio transmitter clasts were continuously tracked with stationary antennas during the flood events.

The method used by Haschenburger and Church (1998) was to install magnetic tracers in 1000 natural clasts deployed in the channel with their depth and original location recorded and also drive 83 scour

indicators into the channel along a series of cross sections down the length of the study reach. The tracers and scour indicators were installed before the October to March flood season with movement tracked the following summer. The tracers that indicated movement determined the active or scour depth while the depth of transported tracers indicated the fill depth. Tracer particles indicated the active width by comparing mobile and immobile tracers across the channel width at 10 cross sections. Tracers deployed on the surface that stayed on the surface after the flood event indicated areas where no scour or fill occurred. Scour indicators were also used to determine the active depth. The distance that tracers moved divided by the duration of the flood event determined the virtual velocity, which coupled with the active depth and width determined the quantity of sediment transported.

From the iron and magnetic tracers studies, Schmidt and Ergenzinger (1992) found that elongated clasts had the highest probability of entrainment and longest transport length while platy clasts demonstrated the least movement. Using the radio transmitter clasts, Schmidt and Ergenzinger recorded field data of step length and rest period for individual clasts, showing an exponential distribution of both step sizes and rest period as shown in Figure 12.

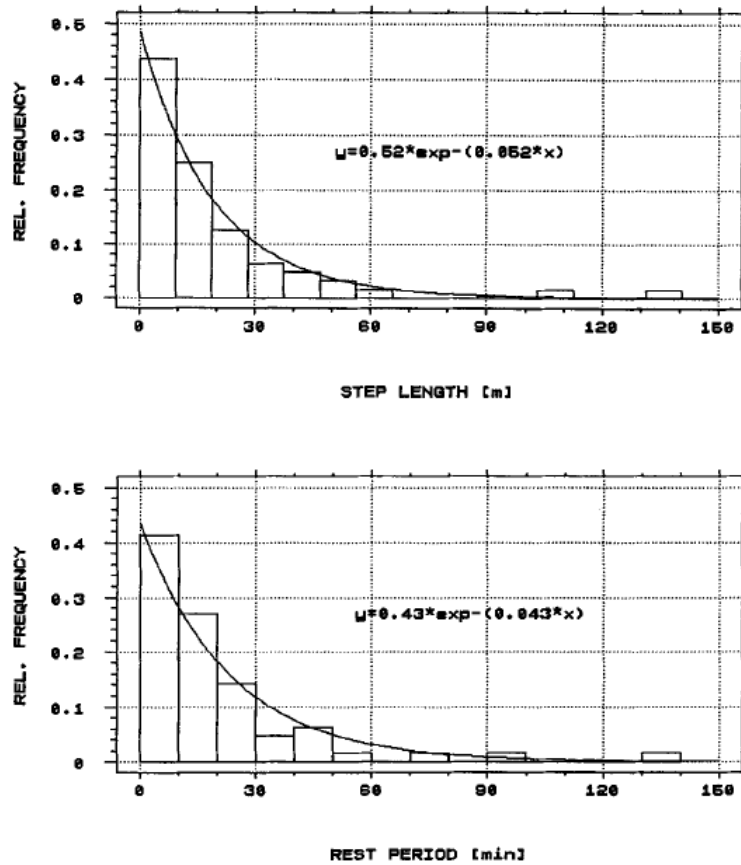


Figure 12 Distribution of Step Length and Rest Period (Schmidt & Ergenzinger, 1992)

Haschenburger and Church found the sediment being transported ranged between 0.09 to 9.7 kg/s based on using magnetic tracers and scour indicators under flood conditions up to 36 m³/s.

While magnetic and iron tracers enable tracking individual clasts, substantial time is consumed excavating tracers to obtain their identity and application is limited to ephemeral channels. Radio tracers used by Schmidt and Ergenzinger were able to identify actual location using radio tracers but were limited to only using 7 tracers – minimizing the ability to capture the stochastic variability inherent in transport mechanics.

2.3.3 RFID Tracers

RFID techniques have largely replaced painting and magnetically tagged tracers due to their relatively long life (up to 50 years), low cost (~\$3/tag) and unique identification codes that allow stones to be identified without disturbing the bed (Lamarre, et al., 2005; Allan, et al., 2006). This technique involves inserting small glass cylindrical transponders (12-32 mm long, 0.8 – 1.8 mm ϕ) into real or artificial stones and then seeding those stones in the river bed. A series of studies have focused on demonstrating the suitability of this method and establishing the performance range of this technique. Nichols (2004) demonstrated the effectiveness of tracking artificial sediment constructed of concrete and sediment with 32 mm RFIT tags inserted in each clast while casting. These clasts were placed into an ephemeral channel in a semi-arid region, with the location of the clasts tracked using a hand held antenna after 4 flow events achieving a 96% recovery rate when sweeping the dry channel identifying tagged clasts that were at the surface, semi-buried, and fully buried. Lamarre et.al (2005) demonstrated sediment tracking using 23 mm RFID tags inserted in 204 natural clasts ranging in size from 42 x 17 mm to 411 x 143 mm. These clasts were removed and replaced in the channel and tracking was conducted with a hand held antenna after 2 bankfull events with a recovery rate of 96% after the first event and 87 % after the second, tracking clasts buried up to 0.25m. Lauth and Papanicolaou (2009) proposed an RFID flume system for determining virtual velocity of sediment as it travels down a flume by detecting when the tagged clast passed through one of four loop antennas positioned across the width of the flume. Each clast would contain two RFID tags oriented at 90 degrees to each other with anti-collision capabilities, increasing the probability that the clast would be detected irrespective of its orientation. Schneider et.al (2010) tracked RFID tagged clasts in a mountain stream using gate and loop antennas and quantified the velocity of clast movement at which detection could still occur when passing through and over an antenna.

Recent studies have used RFID tags to quantify sediment transport characteristics. Bradley and Tucker (2012) seeded 893 RFID tagged clasts in a mountain stream and monitored their movement over four years of spring snowmelt flood seasons. With the data they collected on cumulative travel distance, they were able to refine the distribution model for step lengths and step size. This study was primarily based on travel length over the entire flood season rather than correlating magnitude of sediment transport with hydraulic variables. MacVicar and Roy (2011) seeded a natural channel with 299 RFID tagged clasts in which a large piece of woody debris moved during a flood to force a riffle pool sequence. The tagged clasts were tracked after a series of floods and the sediment mobility was

found to be higher downstream than upstream of a forcing element in a forced riffle pool with lower deposition rates downstream of the forcing element. Milan (2013) explored sediment dynamics through a riffle pool sequence coupling RFID tracking with bedload traps located along the thalweg of the riffle pool and CFD analysis. They found that the pool was maintained during floods by the sediment being routed onto the point bar rather than through the thalweg.

2.3.4 RFID Sediment Transport Research Gap

Over the past 10 years, RFID techniques have increasingly become a staple of sediment transport research. The techniques of sweeping before and after a flood event (Nichols, 2004; Lamarre, et al., 2005; Bradley & Tucker, 2012) provide information on the cumulative length of clast displacement during the flood event but do not provide details on the timing and size of each step correlated to the instantaneous hydrographic conditions. Stationary antennas provide information that the clast has moved past a specific area (Schneider, et al., 2010) or a series of areas (Papanicolaou, et al., 2010) within a certain period of time – providing timing information that can be correlated to hydraulic conditions, but the spatial resolution is limited to the number of antennas employed.

A system that could combine the sweeping capabilities to provide detailed spatial information with data collection over the course of the hydrograph would enhance the ability to correlate sediment movement with instantaneous flow. The sweeping techniques commonly used for field studies are limited to a single antenna and are accomplished by personnel walking through the channel sweeping a circular antenna along the channel bed. This technique is not suitable for continuously sweeping to provide detailed sediment movement data during a flood due to the dangerous conditions during a flood, the time required for the operator to do one sweep of the channel bed, along with the flow and bed disturbances caused by the sweeping process.

The objective of this current research is to design, build, and validate a flume and RFID system suitable for tracking RFID tagged sediment by an automated sweeping of antennas. The flume structure is designed to accommodate scanning from below to provide the opportunity to sweep under the bed with multiple antennas across the width of the flume. This sweeping process is automated with synchronized, multiplexing RFID readers enabling a collection of antennas situated across the width of the flume to repeatedly sweep the active length of the flume, providing improved spatial and temporal resolution for sediment movement data.

Chapter 3

Design and Construction of Flume

The project involved designing and building a flume that would allow continual RFID scanning during experiments. Based on a successful Canadian Foundation for Innovation (CFI) grant and available space in the Hydraulics Lab at the University of Waterloo, it was determined that the flume would be 18.3 m (60') long, 1.2 m (4') wide and 0.6 m (2') deep. To allow coarse sediment transport experiments at slopes where bedforms such as pools and riffles are commonly observed, the flume was required to have a tilting range between 2% downgrade to 0.5% upgrade. It was designed to be capable of supporting a load where it was half full of saturated sediment (rocks, gravel, and sand), with the rest filled with water. The flume was designed for constant feed of sediment that will be stockpiled at the end of the experiment. The technical considerations involved in designing the flume structure and tilting mechanisms along with the sediment handling are discussed in this section of the report.

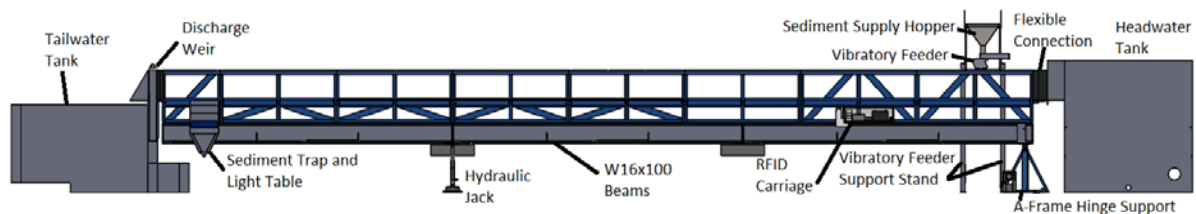


Figure 13 Side View of Complete Flume Assembly

The completed flume assembly detailing all the major components from the headwater tank to the tailwater tank is shown in Figure 13. Water is supplied to the flume system from an overhead pipe delivering water to the base the headwater tank. The water then rises through settling vanes to remove eddies from the water before it enters the flume. Between the headwater tank and the flume there is a flexible connection, enabling the headwater tank to remain stationary while the flume tilts to the required slope. The flume tilts by pivoting on two bronze bushing hinges supported on an A-Frame structure secured to the floor. Sediment is supplied to the flume at the flume head by the vibratory feeder which controls the supply of sediment being delivered from the sediment hopper. The vibratory feeder and sediment supply hopper are located on an independent frame supported directly from the concrete floor to minimize transmission of vibrations into the flume structure. The RFID carriage rides on the flanges of the W16x100 beam up and down the length of the flume. The

hydraulic jack located $\frac{2}{3}$ down the length of the flume is engaged to tilt the flume to the required slope before the flume is secured in position using jack stands. Immediately before the flume discharge, the sediment trap removes sediment from the flume and directs it through a light table and then into a screw conveyor to enable recirculation of sediment. The water level in the flume is controlled by a discharge weir that also directs the water into the tailwater tank where it can be pumped back to the headwater tank.

3.1.1 Flume Tilting Mechanism

The methods considered for tilting the flume include using screw jacks, scissor lifts, and hydraulics.

3.1.1.1 Multiple Jack Screws

The initial method explored for tilting the flume was to use multiple screw jacks (see Figure 14). Screw jack assemblies can be design to handle high loads in applications such as lifting complete trains for maintenance and elevating theatre stages using screw jacks available in capacities up to 2500 kN. The predominant applications using screw jacks involve lifting a load perfectly vertically, which is easily accommodated with a flat load pad and mounting plate (Figure 14).

Jack screws can also be equipped with double clevises (Figure 15) for applications where the upper and lower surface do not maintain alignment with each other as would be the application involving tilting the flume. To provide sufficient stability to support the entire flume, a four screw jack system as shown in Figure 16 was considered. The top view schematic diagram in Figure 16 shows the four jack screws (items 1 to 4), three mitre gear boxes (items 5 to 7) and a motor (item 8) with details provided in Appendix C. The jack screw 1 and 3 would be closer to the upstream pivot, while jack screws 2 and 4 would be twice the distance from the upstream pivot towards the discharge. Jack Screws 1 and 3 would extend at half the rate of jack screws 2 and 4. This could be accomplished by either choosing jack screws 1 and 3 with half the drive ratio or jack screws 2 and 4, or by selecting mitre box 7 with output B having twice the rotational speed of output A.

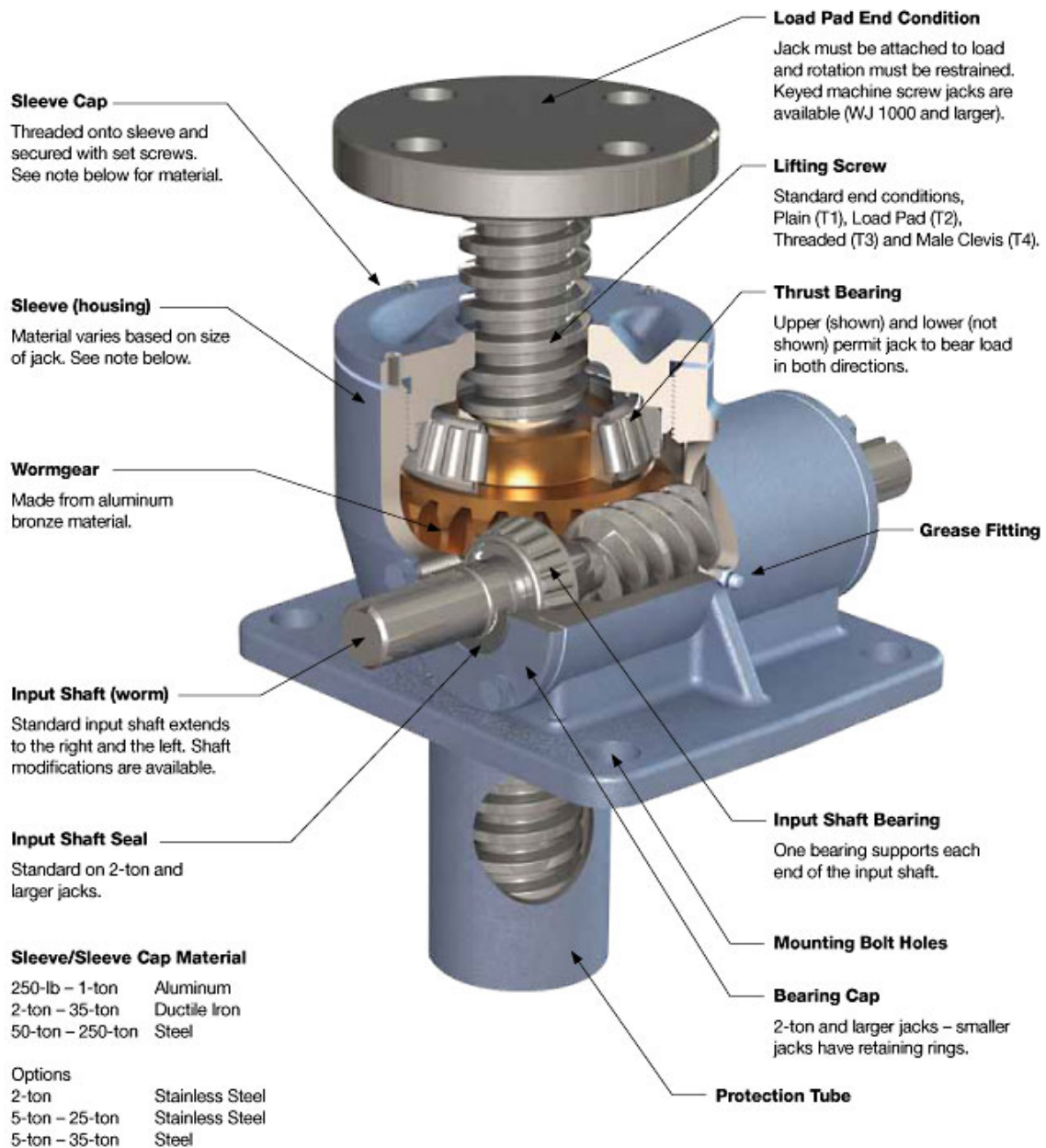


Figure 14 Screw Jack Construction (Joyce Dayton, 2013)

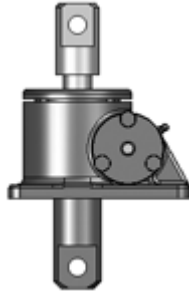


Figure 15 Double Clevis Jack Screw (Joyce Dayton, 2013)

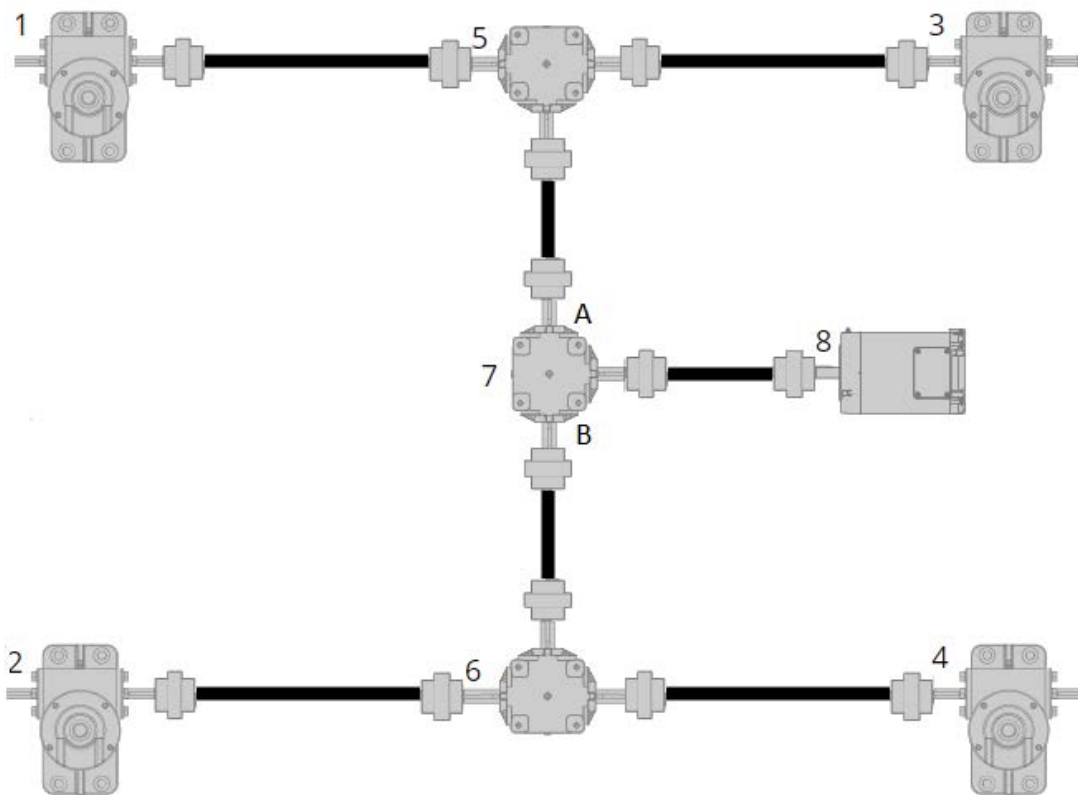


Figure 16 Jack Screw System with Mitre Gear Boxes and Motors

While jack screws combined with mitre gear boxes provide a convenient method of distributing lifting force over the length of the flume, the tilting of the flume resulting in the rotation of the jack screws causes 2 mm of lateral movement of the input shafts on the jack screws. Layout of the Joyce Dayton 5 ton jack screws, model JD-WJT65U4D-014_40-STDX-STDX-X on each side with a Three way mitre box model JD-RC-18_3-WAY in the middle indicates that there is 279 mm between the

faces of the input shaft for the jack screw and output shaft of the mitre box. This lateral movement of the jack screw input shaft must be accommodated by angular and parallel offset misalignment of the jack shafts between mitre gear box and jack screw, resulting in a 0.42° angular misalignment of the jack shaft.

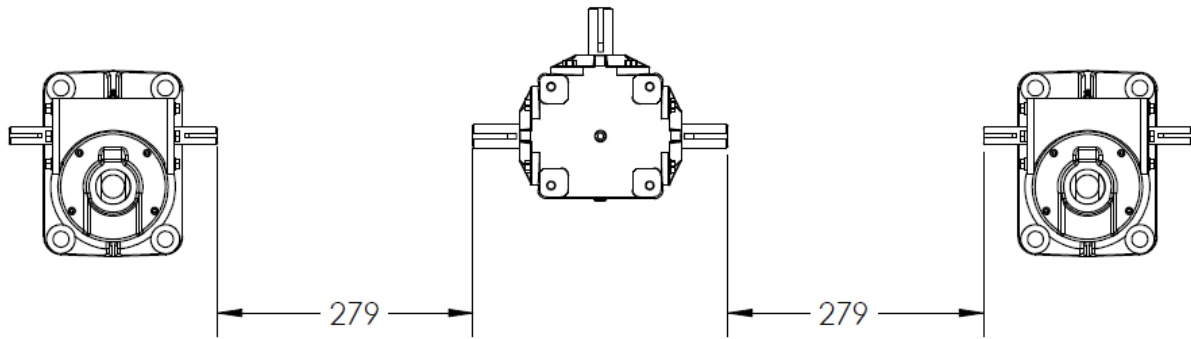


Figure 17 Jack Screw and Mitre Gear Box Distance

Machine grade couplings such as the Falk Gear Couplings (Rexnord, 2014) are designed to operate with maximum angular misalignment of 0.06° . The high level of misalignment in this application would cause rapid deterioration of the coupling along with the damage to the shaft bearings on the mitre box and jack screw, making this design unsuitable for long term operation.

3.1.1.2 Multiple Scissor Lift Jacking System

One of the techniques to avoid the shaft misalignment problems inherent in the jack screw design is to tilt the flume using two scissor lifts driven by a common shaft using rollers on the upper deck to support the flume (Figure 18).

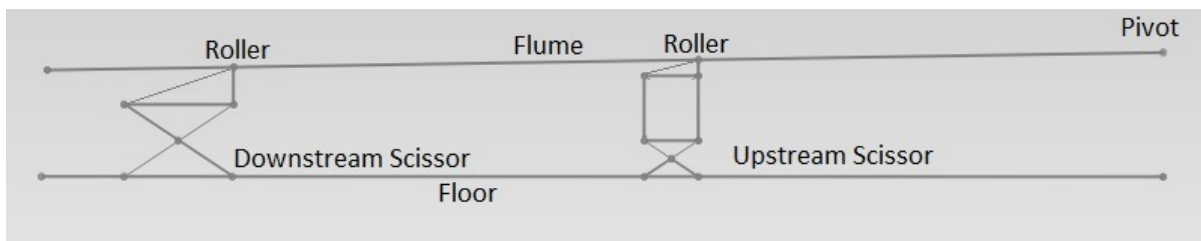


Figure 18 Schematic Diagram of Scissor Lift with common shaft

The upstream pivot location is at the top right. The length of scissor lift travel has to be proportional to the length that the scissor lift is away from the flume pivot. Thus the downstream scissor lift, being

twice the distance from the pivot as the upstream scissor, must be twice the size. To enable both scissor lifts to provide motion that is proportional to each other through the entire range of motion, the angular rotation of the legs on the larger lift need to match the angular rotation of the smaller legs. Traditionally, scissor lifts are driven by hydraulic cylinders. However, hydraulics cannot assure that the speeds of the two scissors are precisely matched. Hydraulics cylinders can also creep down over time as fluid slowly leaks past the seals on the pistons and valves, resulting in the angle of the flume changing over the course of the experiment and creating an unsafe work environment for any activities that must be accomplished under the flume.

Driving the scissors lifts with acme threads enables the speed of these two scissor lifts to be precisely controlled. Figure 19 shows isometric and elevation views of a proposed design of a scissor lift mechanism driven with an ACME thread. The right pivot on the bottom is secured to the floor structure while the right pivot on the top is attached to the deck structure, which moves up and down while staying horizontal. The left bottom roller moves along a track on the bottom frame structure while the top left roller moves along a track on the underside of the top deck. An acme thread pulls between the mid-span of cross bars connecting the right lower pivots and left lower rollers. Due to the magnitude of the bending force created by the acme thread, the cross bars need to be machined out of 6" (152 mm) steel bar stock to avoid deformation under load.

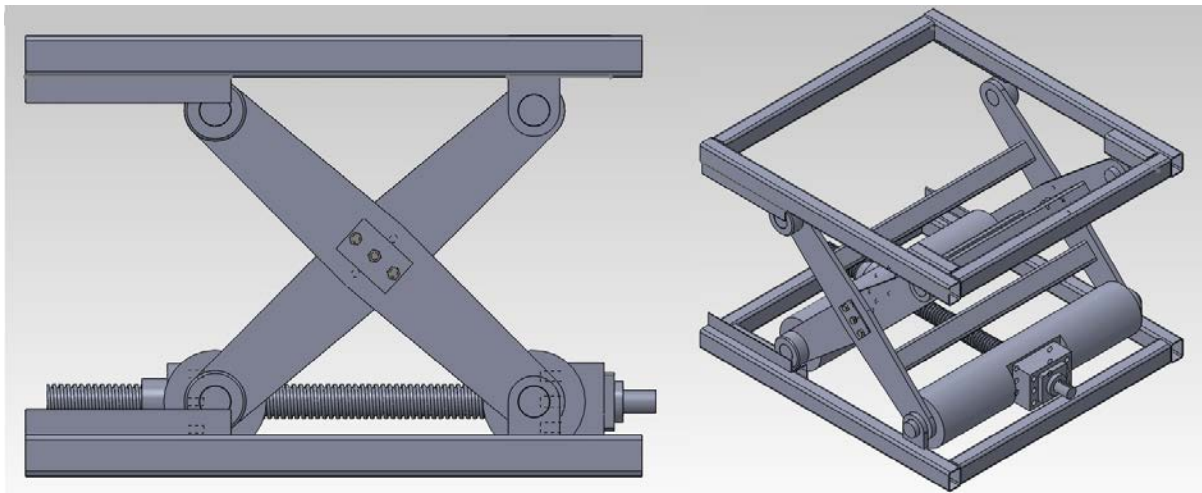


Figure 19 Scissor Lift Mechanism Driven by ACME Thread

For the larger downstream scissor lift to move at twice the speed of the smaller upstream one, the left lower pivot and right lower roller of the larger scissor assembly must be pulled together at twice the

rate as the smaller scissor lift. On smaller ACME threads (up to 2 1/2") it is possible to get threads in different pitches (threads per inch) - enabling the smaller scissor lift to have 2 treads per inch while the larger scissor lift has 4 threads per inch. However, with the pulling force required in this design, (40,000 lb on each scissor when the scissors are at the lowest extreme), 3-3/8" acme threads are required on each design. The limiting factor is the bearing mount on the end of the lead screw. The 3-3/8" acme thread only comes in one pitch. Therefore, the different speed of the two scissor lifts must be accomplished by a gear reducer between the two scissor lifts.

Since the scissor lift path of movement is purely vertical, rollers (see Figure 18) must be used where the scissor lift supports the flume. These rollers would be attached to a triangular structure on the top of the scissor lift deck allowing both a positive and negative slope of the flume to be accommodated as the flume tilts through its designed range of slope.

Even though the concept of multiple scissor lifts has an appealing simplicity, there are many design considerations that make it impractical for construction in facilities which do not have extensive experience in scissor lift construction. Since very high loads are transmitted through the pivot points, high strength bushings such as metal polymer composite bushings must be used rather than roller bearings or regular bronze bushings. Experience in properly fitting these bushings exceeds that available in a common machine shop. Due to the forces transmitted through the scissor lift, the assembly must be welded rather than bolted to minimize localized stress concentrations. The welding must be accomplished while maintaining alignment to ensure smooth operation after completion, requiring the creation of custom welding jigs. Often the degree of weld distortion is not fully anticipated until multiple similar structures have been welded. Since only one smaller scissor and one large scissor are required, this does not afford enough experience to refine the welding and securing techniques required to ensure the scissor lifts do not bind during operation. The heat generated in the entire assembly during the welding process must also be regulated to ensure the bushings do not experience heat damage. The degree of design and manufacturing considerations involved in establishing a functional multiple scissor lift design result in this being an un-feasible method for tilting the flume.

3.1.1.3 Single Hydraulic Support Tilting Design

With the view of reducing the mechanical complexity, reducing construction costs, along with reducing time to build the flume, an analysis was conducted on building the tilting structure using

only one hydraulic jack. Using a single lift point eliminates the need to use a mechanism to ensure that different lifting points are moving at rates that are proportional to their distance from the flume pivot.

A suitable hydraulic jack is the single acting general purpose Enerpac™ cylinder, model RC-2514 with a 232 kN (25 ton) capacity and 362 mm (14.25 inch) stroke. This cylinder can be activated with an Enerpac™ model P-80 hand pump with a maximum operating pressure of 700 bar (10,000 psi). To accommodate the pivot of the ends on the hydraulic cylinder, end cradles are built with pivot capacity (see Figure 20). The cylinder pivots 0.14° through its range of extension to tilt the flume from downward 2.0% slope (1.15°) to upwards 0.5% slope (0.29°).

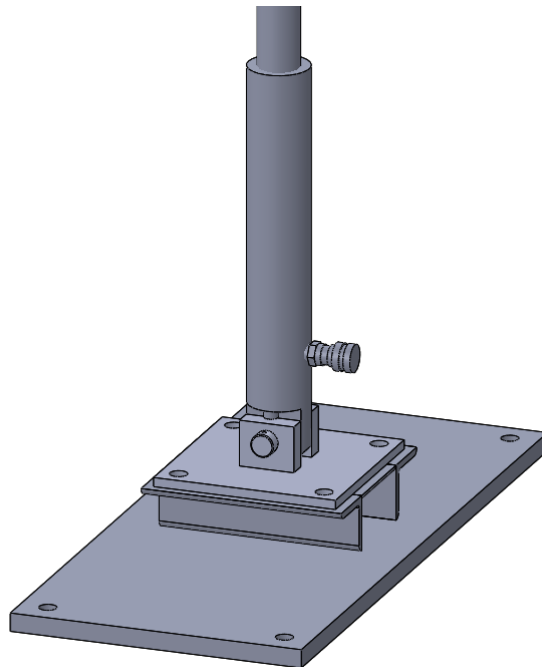


Figure 20 Hydraulic Cylinder Pivot and Floor Mount

After the flume is jacked in position, it is supported by the upstream pivot along 6 six jack posts (see Figure 21), each with a rated capacity of 80,000 N (18,000 lbs), that are in pairs under each W16x100 section down the length of the flume. With the jack posts in place, pressure is able to be taken off the hydraulic jack. During experiments, the load of the flume, water, and sediment will be fully supported by the upstream pivot and the jack posts.



Figure 21 Jack Post

Tilting of the flume and securing of the jack posts need to be carried out by lab personnel trained in operation of the hydraulic jack and adjusting the jack posts. Since the flume will normally be set at one slope for the duration of a series of experimental runs, it is anticipated that the use of lab personnel to occasionally set the flume slope is more cost effective than creating a fully automated mechanism for setting the slope and securing it in that position for the duration of the experiments.

3.1.2 Flume Structural Design

Based on the decision to tilt the flume using a single hydraulic support, the structural design was then completed to ensure that deflection of the structure was within acceptable limits. The structure was analyzed using SolidWorks™ solid modeling software with COSMOS finite element static stress analysis module.

While the flume is being tilted, it will only be supported by the upstream pivot and the hydraulic jack (Figure 22). The structural support for the flume would need to be made out of W16 x 100 wide flange beams (nominally 16" high, 100 lb/ft). The deflection plot using these beams indicates that the maximum deflection is 6 mm (deflection magnified for visualization).

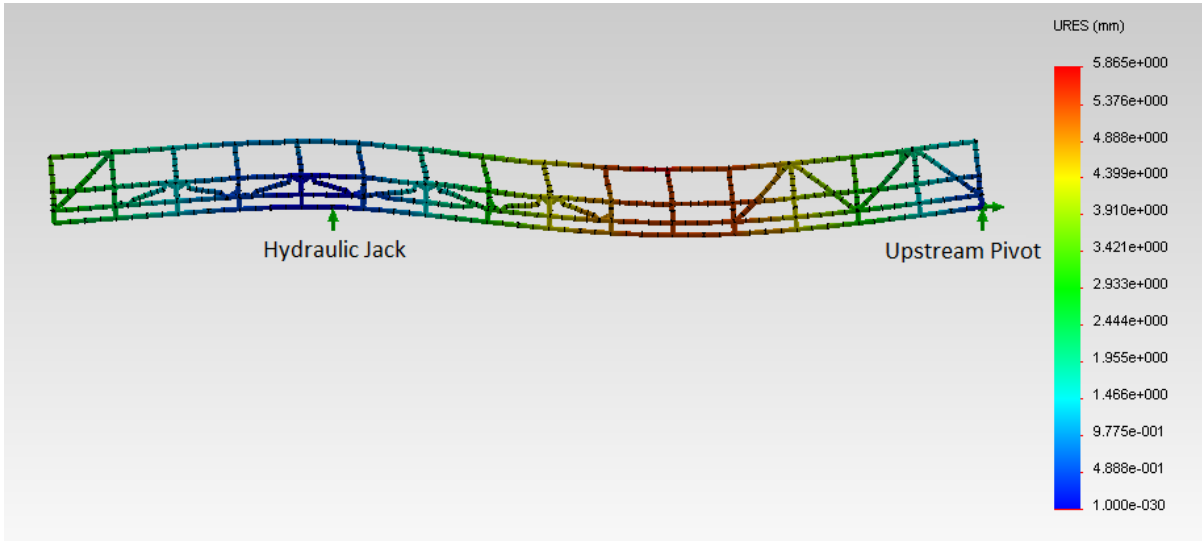


Figure 22 Deflection Plot of Flume Supported by Single Hydraulic Cylinder

The side view of the flume shown in Figure 23 provide more detail of the components.

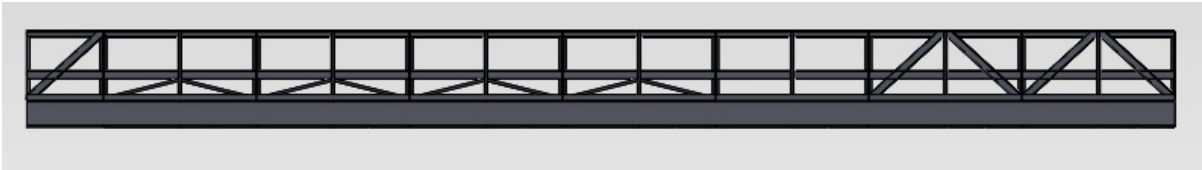


Figure 23 Flume Side View with Component Details

The water would flow from right to left. At the right end, diagonal bracing traverses from the top of the flume to the bottom of the flume. Then there is a section of flume with no bracing, facilitating access to the RFID carriage, which will be located under the flume. The function of the bracing is for shear load transfer between the structural angle iron along the top length of the flume and the W16x100 underneath the flume. Along the top of the flume, the tensile loads will be highest directly above the hydraulic jack while the compressive loads will be highest midway between the hydraulic jack and the upstream pivot. Along the W16x100 beam, the compressive loads will be highest at the hydraulic jack while the tensile loads will be highest midway between the hydraulic jack and the upstream pivot. The diagonal brace at the downstream end of the flume support the tensile load in the top of the flume with the compressive load in the W16x100, while the diagonal brace at the upstream end will support the compressive on the top of the flume with tensile load in the W16x100 at that point. Since the maximum load transfer will happen at the ends of the beam, by putting the no-bracing

section midway between the right end pivot and the hydraulic support point, the loss of strength is minimized.

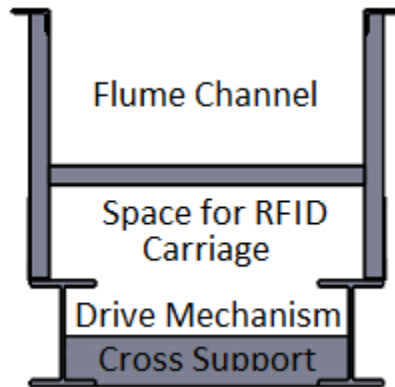


Figure 24 Flume Structure End View

The end view of the flume shows the proposed configuration of the beams and space for the RFID tracking. By having the upper structure of the flume directly bolted to the beams, there is not a requirement for cross beams at the base of the upper structure to provide rigidity against the lateral forces of water pressure on the side walls of the flume. This provides space for the RFID tracking carriage and drive mechanism.

The floor of the flume needs to provide the bottom sealing surface for the flume, support for the sediment and water, and also electro-magnetic transparency for the RFID tracking to enable detection of PIT tagged clasts in the flume while the antennas are mounted on the RFID carriage under the floor (see Figure 24). The RFID carriage will traverse up and down the length of flume on tracks underneath the flume floor so that the antennae traverse do not disturb water flow or instrumentation and experimental apparatuses in and over the flume.

The floor plates of the flume are PVC sheeting chosen for their imperviousness to water while providing rigidity and crack resistance and allowing transmission of RFID signals. Since this flume is 4 feet (1.2 meters) wide, un-supported PVC would need to be 3 inches (76 mm) thick (based on analysis of deflection in SolidWorks), which would be prohibitively expensive. By putting in intermediate floor supports similar to floor joists used in residential construction, the thickness of the PVC can be reduced. Steel intermediate supports provide the advantage of able to be welded to the flume frame and also provide a high degree of stiffness while using a small size structural member. However, each intermediate steel support would block transmission of electromagnetic radiation and

result in multiple detection shadows for the RFID scanning system. While some steel cross bracing is essential to tie in the side walls and ensure that the hydrostatic pressure does not cause excessive horizontal deflection of the walls, the RFID detection can be maximized by minimizing these steel cross braces. If steel cross bracing is limited to every 1.2 m (4'), intermediate floor supports could be created out of material that does not block electromagnetic radiation, allowing RFID tag tracking accuracy to be maintained while minimizing PVC floor thickness. The two intermediate support materials considered were PVC pipe and 2" x 4" framing lumber (2x4s).

Intermediate supports could be created out of PVC by inserting 2 ½" Schedule 40 ABS pipe inside 3" Schedule 40 ABS pipe and spacing these pipes every 0.3 m (12"). The static water and sediment load would result in a peak deflection of 11 mm (0.43") on the ABS pipe at mid-span where there are no joints. However, significant bowing of the ABS pipe and PVC floor will cause the ends of the PVC plate to pull in. For the end to end butt joints of one floor plate to another, this will result in the joints experiencing tensile load creating the potential for tensile cracks in the sealing material of the joint. For the joint between the floor and side wall, this pulling in of the floor plates will create shearing forces in the joint between the floor plates and side wall plates. The intermediate support deflection for the PVC pipe supports does not account for the deflection of the PVC floor plates due to loading. Even though this level of deflection is acceptable for PVC, the tensile forces experienced by the floor plate to floor plate joint and the shear forces experience by the floor plate to sidewall joint will increase the probability of crack formation in the joints, reducing the sealing of the flume.

Intermediate supports created out of spruce 2x4s joists was also analyzed with a spacing between joists of 0.4 m (1.3'), resulting in a deflection of 5.2 mm (0.20") at the mid span on the joists. These joists could be put either along the flow direction or perpendicular to the flow direction. If these joists were put along the flow direction of the flume, the steel cross bracing at every 4 feet would need to be larger to accommodate the joist load. Increased cross bracing height would reduce the space available for the RFID antennas, increase the distance that the RFID antennas are from the clasts containing PIT tags, and increase the amount of RFID detection shadows. Intermediate supports positioned across the flume can be supported by the structural members that are part of the sidewall structure and can be designed to handle the extra load of the intermediate supports without impinging on RFID detection. Thus, intermediate supports across the flume provide the superior orientation as shown in Figure 25.

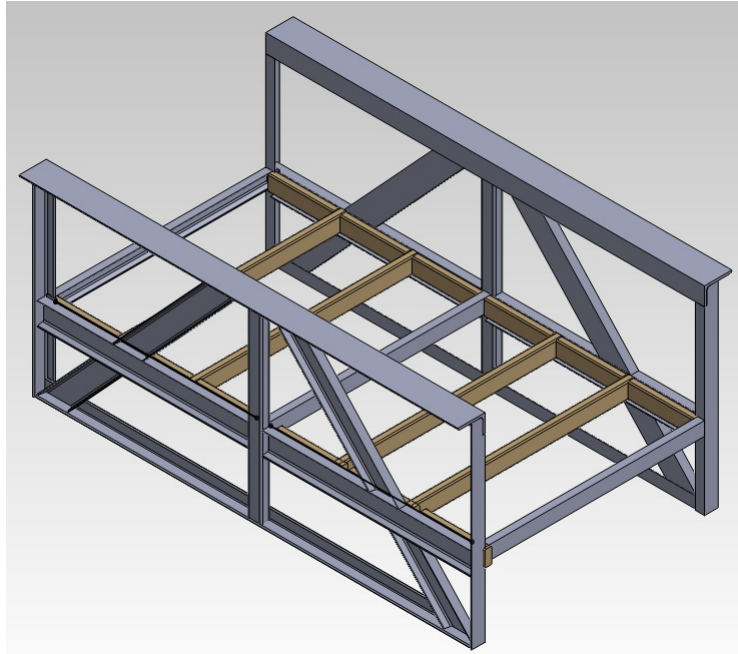


Figure 25 Framing Wood Intermediate Supports Shown in Flume Upper Section

The joists sit on an angle iron ledge what is welded to the horizontal C-Channels. Spacer blocks also sit on the angle iron ledge and maintain spacing between the joists. The wood intermediate supports and spacer blocks can be replaced from the underside of the flume without disturbing the PVC floor plates and sealing. Once the spacer blocks are pulled out, the wood intermediate supports can be turned diagonally and dropped down.

A Finite Element Analysis was conducted on the PVC floor plate 1.2m (4.0') wide and 0.4 m (1.3') long representing the full width of the flume and the length between floor joints. Using 3/4" PVC, the total deflection was 2.2 mm (0.09") as is show in Figure 26.

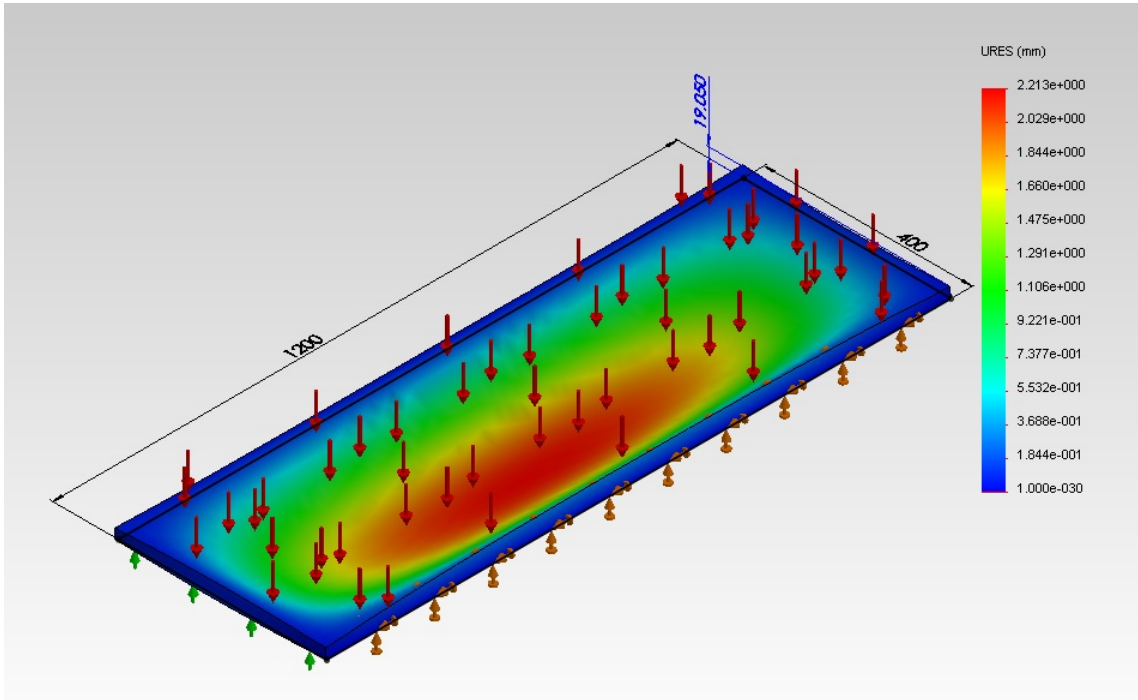


Figure 26 PVC Floor Plate Deflection Finite Element Analysis

Since the PVC floor plates are supported on the wood intermediate supports which also experience 5.2 mm (0.2") of deflection under water and sediment load, the total maximum deflection of the floor plates will be 7.4 mm (0.3") in the center of each section of floor plate (red section in Figure 26). The reduced deflection of the wood intermediate supports over the PVC supports will reduce the stresses on the joint seals while simplifying floor plate installation and maintenance of the intermediate supports.

3.1.3 Water Contact Surface Design and Sealing

Since the upper flume sections (see Figure 25) contribute to the overall structural rigidity of the flume as shown in Figure 22, any gasket material between sections would create weak points for forces being transmitted from one structural member to another. For this reason, each section of the upper flume must be bolted directly to the adjacent one. Rather than sealing one structural section to the next, the sealing for the water is between adjacent PVC/Acrylic sheets. The sheets are shorter than the welded flume sections to allow a 6 mm (1/4") sealing material gap between the sheets enabling sufficient space for the sealing material to expand or compress under the deflection of the flume structure and floor plates.

Rather than directly bolting the side walls to the flume structure and resulting in leak potentials at each bolt hole, the side plates are secured in place using top L brackets (see Figure 27) which are bolted to the top of the flume structure. The L brackets are designed to keep the side walls from collapsing into the center when there is no water in the flume. When water is in the flume, the hydrostatic pressure will push the side walls against the frame, thus the L brackets only need to be strong enough to keep the side walls in place. Holes drilled and threaded for 3/8-16 UNC bolts are spaced along the length of the stop structure of each flume section to facilitate securing the top L brackets to the flume structure and retaining the side wall.

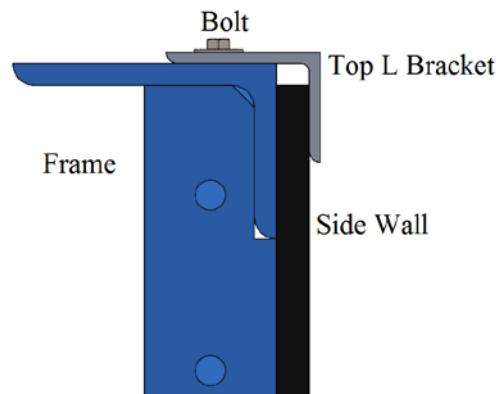


Figure 27 Top L Bracket to Retain Side Wall Plates

3.1.4 Sediment Supply with Vibratory Feeder

The sediment is supplied to the flume using a vibratory feeder located at the upstream end of the flume as shown in Figure 28. The vibratory feeder is equipped with a hopper to store the sediment and direct it down to the shaker table on the vibratory feeder. The vibratory feeder is designed to provide a constant feed rate of sediment into the flume. Since ultrasonic flow measurement equipment will be used in the flume, the vibratory feeder must be isolated from the flume so vibrations are not transmitted into the flume and to the ultrasonic equipment. The shaker table on the vibratory feeder is mounted on elastomeric isolation pads. In addition, the vibratory feeder is mounted on an independent support stand which is directly bolted to the concrete floor of the fluids lab with no contact with the flume.

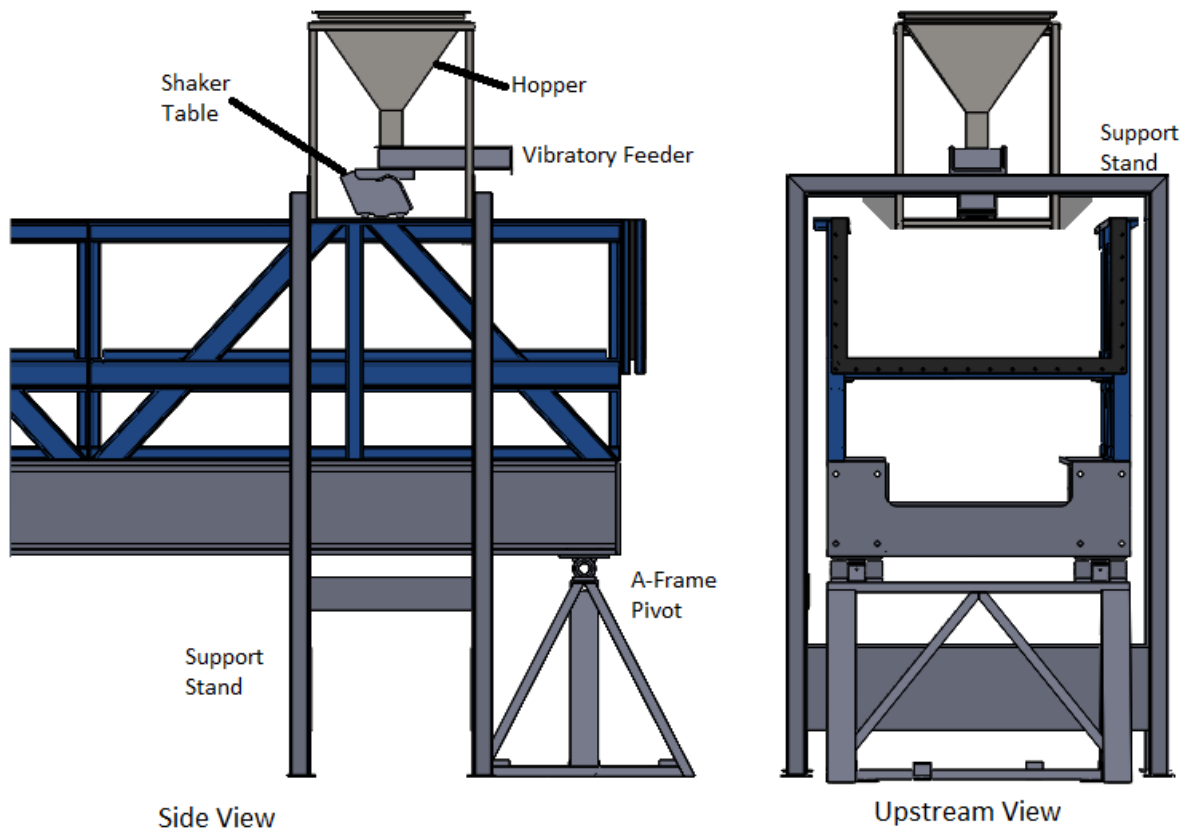


Figure 28 Vibratory Feeder

Sediment can be delivered to the hopper either manually or via a semi-automated method. A set of rolling stairs can be mounted adjacent to the vibratory feeder support stand (Figure 29). These could be secured to the side of the support stand by quick release clamps to secure the stairs while feeding sediment, but enabling removal of the stairs when equipment needs to be moved around the base of the flume. A step deck with railing would need to be added to the vibratory feeder support stand to ensure safe access to the lip of the hopper.

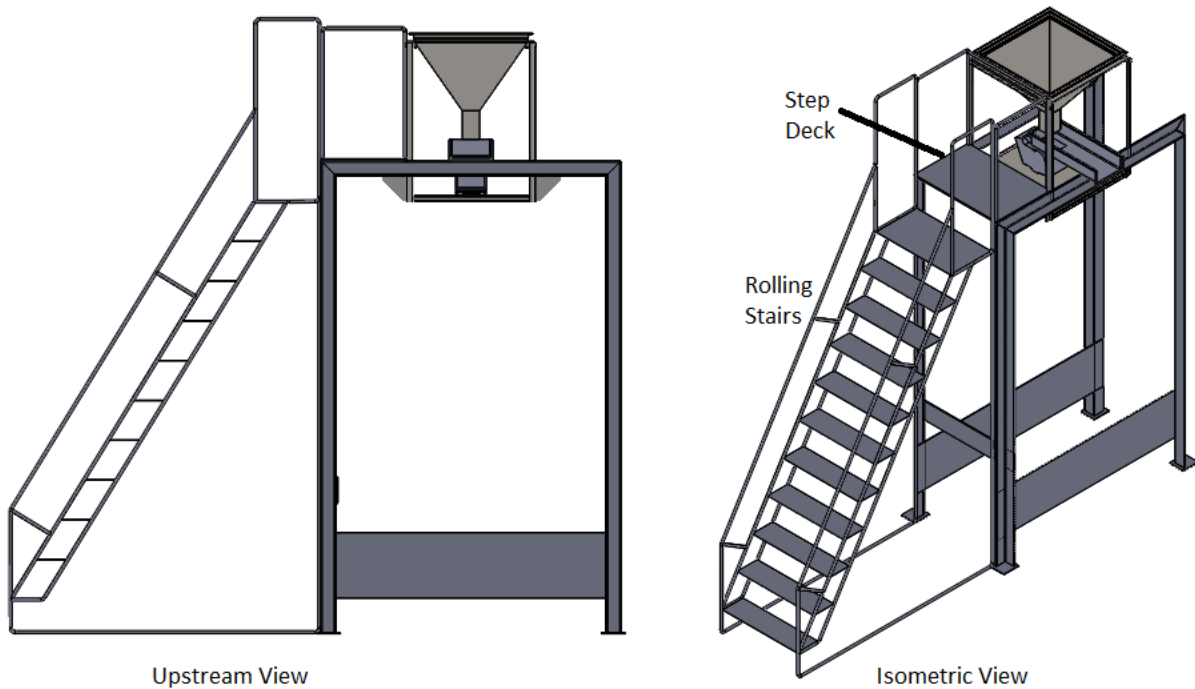


Figure 29 Vibratory Feeder with Rolling Stairs

The delivery of sediment to the hopper could also be semi-automated by installing an overhead beam and motorized trolley crane to lift a dump box up to the hopper (Figure 30). The dump box would be manually loaded on the ground. If the flume was in a recirculating mode, a wheel barrow could be placed under the screw conveyor discharge to be automatically filled up. Then the wheel barrow could be wheeled over to the dump box. A ramp could be installed adjacent to the dump box to enable the wheel barrow to dump directly into the dump box. The dump box would then be raised using the motorized trolley crane and moved into position with the dump box pivot pins in the guide slots on the guide plate (Figure 31). Once the dump box is located in the guide slots, the operator can use a pole and push upward in the pivot pole pocket on the back of the dump box, tilting the dump box and dumping the sediment into the hopper.

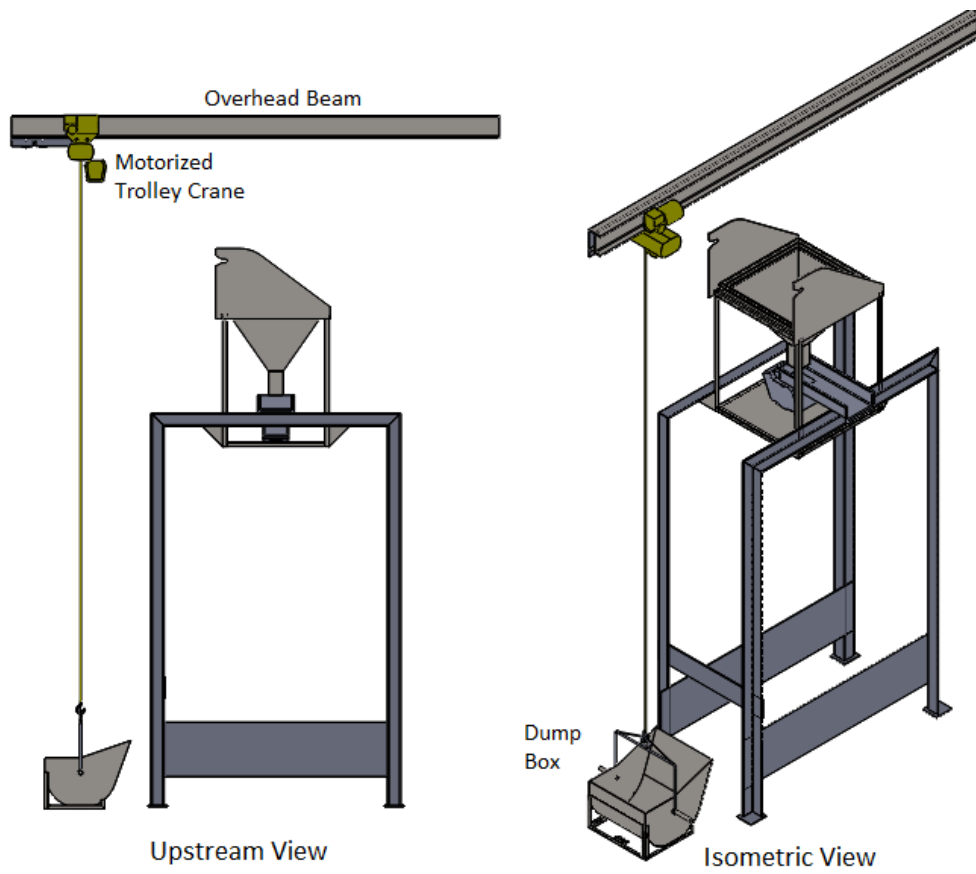


Figure 30 Vibratory Feeder with Motorized Trolley Crane with Dump Box at Floor level

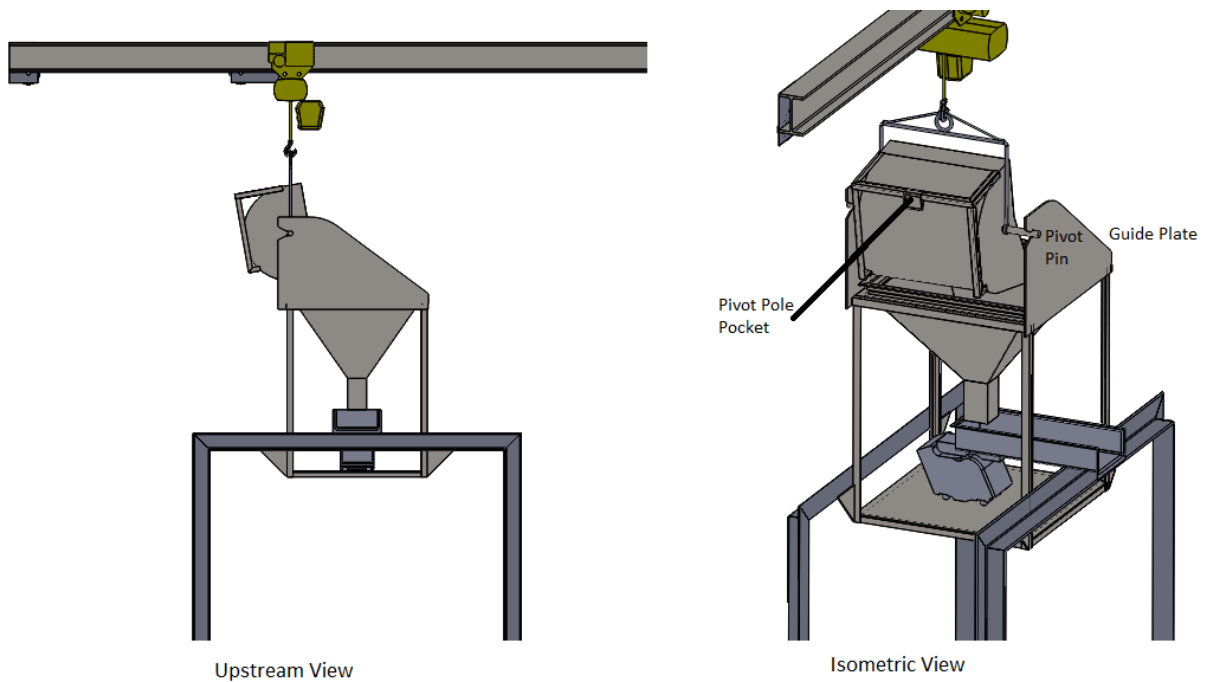


Figure 31 Vibratory Feeder with Dump Box Dumping into Hopper

The dump box with overhead beam and trolley crane provided an efficient method of transporting sediment to the vibratory feeder hopper.

3.1.5 Sediment Extractor with Light Table Measurement

A light table based on the concept demonstrated by Zimmermann et.al (2008) is proposed for continuous measurement of sediment quantity and size fractions discharging from the flume. While the light table in Zimmermann's experiments was located at the end of the flume (see Figure 9) with a step immediately before the light table altering the flow and sediment transport characteristics before the water and sediment pass over the light table, the proposed light table for the current flume will be incorporated into a sediment trap located under the flume floor as shown in Figure 32. This will allow water to flow over the sediment trap out the discharge of the flume.

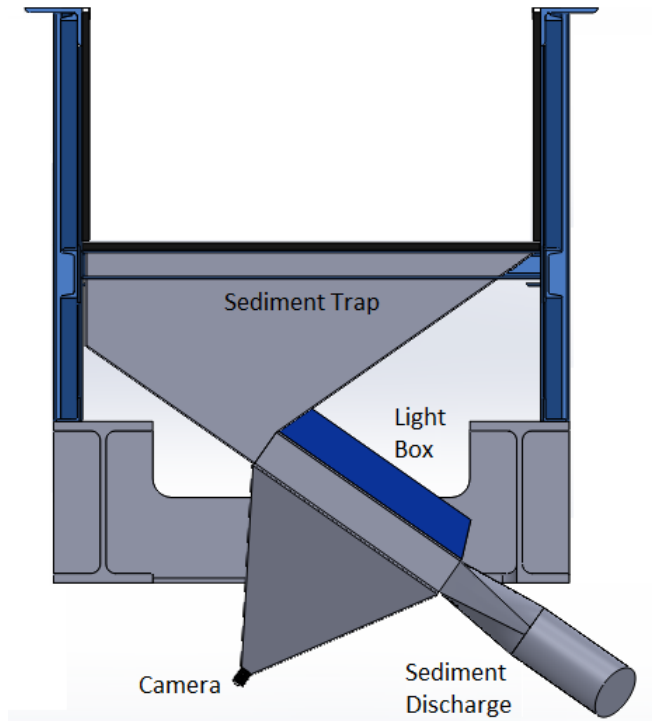


Figure 32 Light Table and Sediment Trap Arrangement End View

The sloping walls of the sediment traps are designed at an angle 35 degrees below the horizontal to allow sediment to slide down the sloping walls without aggrading while funneling it down to the entrance for the light table. The sediment trap and light box are laid out to ensure only the inner flange of the W16x100 beam on the right side needs to be notched while the webbing and visible flange of the W16x100 are continuous (see Figure 33).

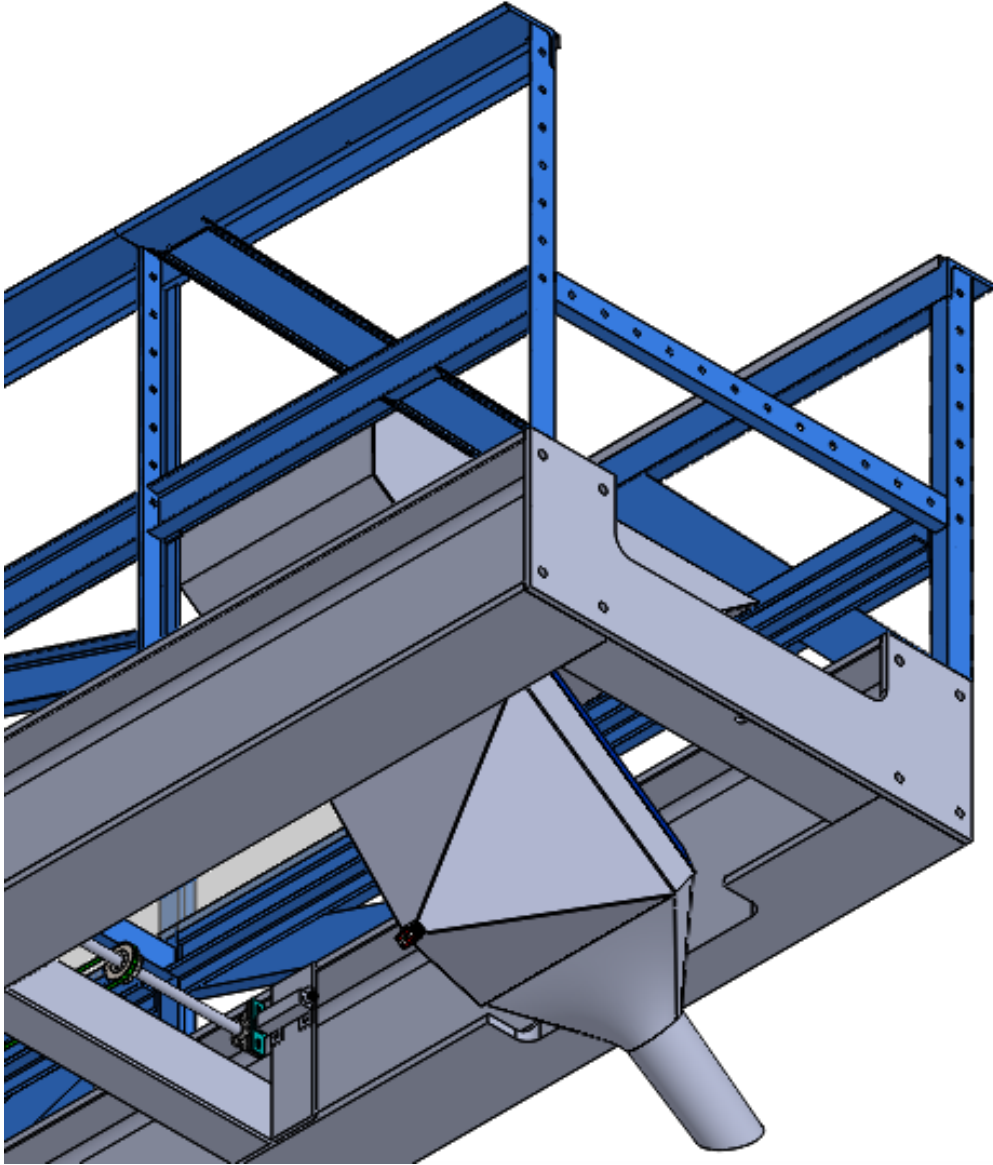


Figure 33 Light Table Bottom Isometric View

The tilted rectangular light table has translucent material on the top to allow light from the light box to enter the light table while maintaining sealing. Transparent material seals the bottom of the light table enclosing a channel for the sediment to pass through while enabling the camera to capture images of the sediment as it slides and rolls down the light table.

The screw conveyor delivers sediment from the sediment discharge below the light table (see Figure 32) to the screw conveyor discharge located above the water level in the flume (see Figure 34). This

will ensure that only sediment is being transported up the screw conveyor and out screw conveyor discharge. A movable bin will be located below the screw conveyor discharge to catch the sediment as it is transported up and out the screw conveyor.

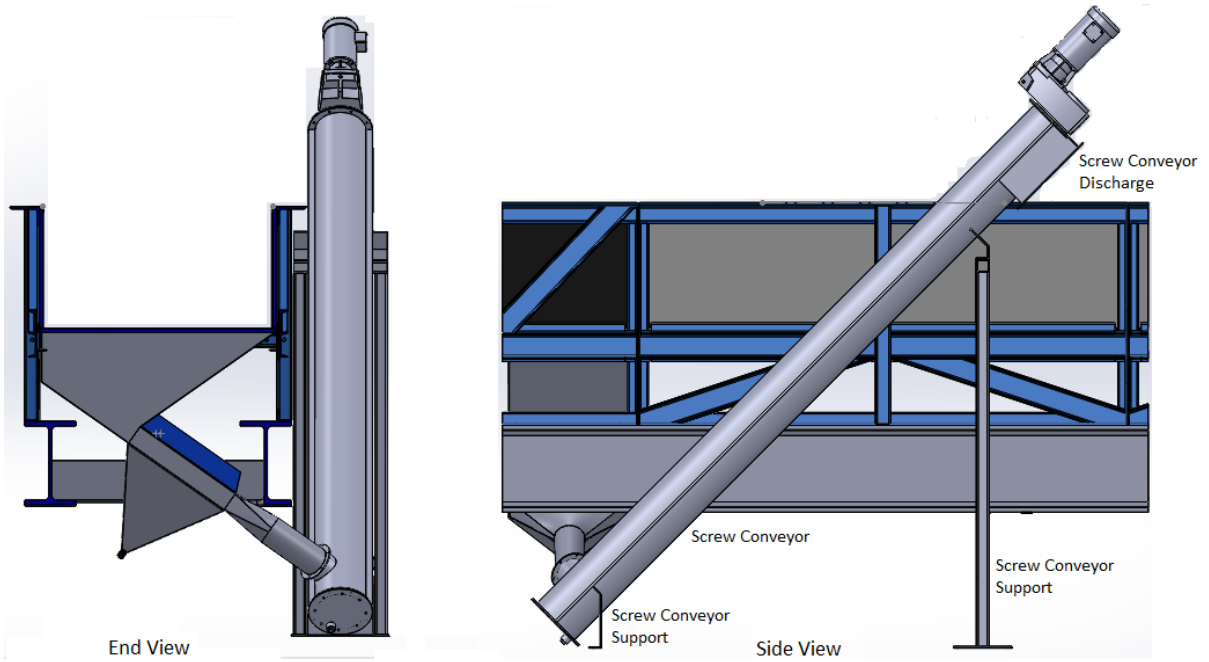


Figure 34 Screw Conveyor Arrangement

Chapter 4

Design and Construction of RFID Tracking System

The RFID tracking system involves the integration of electronics to multiplex 12 RFID antennas while sending the obtained RFID tag data to a computer, along with developing a motion mechanism and control system to traverse the antennas back and forth along the length of the flume.

4.1 RFID Background

4.1.1 RFID Operating Principals

Radio Frequency Identification (RFID) methods dates back to the World War II where they were used to identify planes as they flew over. The radar systems developed by the Americans, and British, Germans, Japanese, were capable of identifying the presence of a plane, but they were not able to determine whether it was an enemy or friendly plane. The British developed the *Identify Friend or Foe* system that would be mounted on a plane. It would receive a signal from a ground radar station, and respond back with a corresponding signal to identify it as friendly (Violino, 2016).

The technology for sediment tracking RFID is based in animal tracking RFID (Jones & Chung, 2007) developed by Los Alamos National Laboratories. It was initially intended to track cattle and ensure the individual cattle were receiving the intended dosage of hormones and medicine. Initially an Ultra High Frequency system was developed which could have a read range up to 6 m in air. However, the high frequency radio waves attenuate rapidly in natural water due to the dissolved solvents which act as conductors (Jiang & Georgakopoulos, 2011; Benelli, et al., 2009) as expressed in Equation 1:

$$\alpha = 0.0173\sqrt{f\sigma} \quad (1)$$

where α is the attenuation, f is the frequency of the radio waves, and σ is the conductivity. This attenuation is not as pronounced for lower frequency radio waves. This has led to the use of low frequency RFID technologies being preferred for animal tracking and sediment tracking in aqueous environments (Ruiz-Garcia & Lunadei, 2011).

Two general types of RFID technologies exist: passive and active systems. In an active transponder system, the tags are equipped with a battery and continually broadcasts electromagnetic radiation encoding their identification (Habersack, 2001) or broadcast when their orientation changes

(Habersack, 2002). Such systems have a limited time of use based on battery life. In contrast, transponders used in passive transponder do not store their energy. Rather, a coil on the tag receives energy in the form of electromagnetic radiation when a reader is energizing the device by broadcasting a 134.2 kHz radio wave. As the waves of electromagnetic radiation cut through the coil on the tag, a voltage is created across the length of the coil. This voltage then drives a current through a resonator circuit which further amplifies the voltage. This amplified voltage is fed through a rectifier and energizes the charge capacitor.

Passive RFID technologies can be classified as either full duplex (FDX) in which transmission from the reader and response from the tag can be happening simultaneously or half duplex (HDX) in which the transmission and response must occur asynchronously – with the response only starting once the transmission is finished. In a FDX system, the reader continuously generates electromagnetic energy which continuously powers any RFID tags that are within range. The tags then continuously broadcast a response up to 30 times per second. This results in the ability to make very small tags because they only have a coil, ferrite rod, and IC chip. However, the range for FDX systems is very small due to their use of amplitude shift keying (AM) technique which is susceptible to atmospheric noise. FDX antennas must have the insulated wires rigidly secured in place with an air gap between the insulated wires and any water, requiring antenna installed in a channel bed to be encased in sealed plastic tubing. In contrast, HDX systems operate more like a 2 way radio in which the reader sends out a charge signal then stops transmission and allows the tags to respond as shown in Figure 35. The HDX systems use frequency shift keying (FSK) techniques to transmit the response data with the typical low bit frequency at 134.2 kHz and the high bit frequency at 123.2 kHz (Texas Instrument, 2000). This technique has a higher immunity to atmospheric noise, enabling larger detection ranges. The antennas for HDX system can be composed of a simple coil of wire and can be placed directly in water, improving their suitability for construction and installation by field personnel rather than requiring professional antenna expertise as is the case for FDX antennas. The advantages of HDX systems have led to them being the preferred technology for use in sediment transport studies (Nichols, 2004; Lamarre, et al., 2005; Allan, et al., 2006; Bradley & Tucker, 2012).

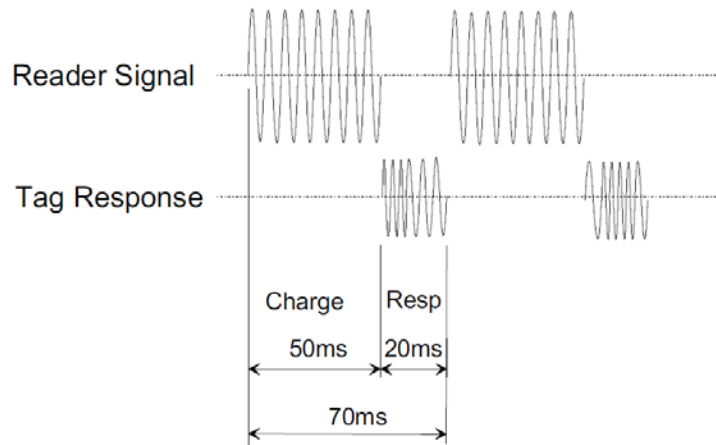


Figure 35 Low Frequency Half Duplex Charge and Tag Response (Texas Instrument, 2004)

In applications involving multiple antenna in a HDX system, each reader antenna must be synchronized to ensure that the period for transmitting the charge electromagnetic radiation is occurring simultaneously for each reader/antenna and then they stop transmission to enable receiving response signals from tags broadcasting their ID. Since the charge signal is larger than the response signal, if some of the readers were broadcasting a charge signal while the tags were responding their ID, the response signal would be lost and no tags could be read.

4.1.2 Elements of an RFID system

A typical application for reading the tags consists of an antenna, tuning module, reader module, and data logger or display as shown in Figure 36.

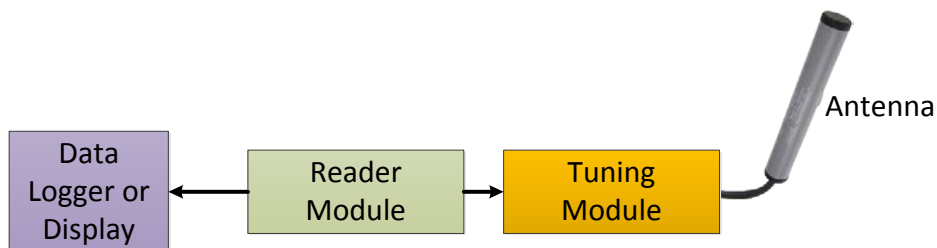


Figure 36 Typical reader components

Each antenna will have a unique inductance which is a function of the number of loops, tightness of the winds, and whether the volume surrounded by the coil is air or some other material interacting with the magnetic flux. The process of tuning a system involves matching the inductance on the antenna with the capacitors on the tuner, creating an electrically harmonic system that amplifies the electrical alternating current and resulting electromagnetic field.

The reader module broadcasts a charge signal and receives a response through the tuning module paired with the antenna. The radio frequency information is translated into digital information which is communicated with the datalogger or display unit.

4.1.2.1 RFID Transponder Design

The tags predominately used for tracking sediment (Lamarre, et al., 2005; Nichols, 2004; Chapuis, et al., 2014; Schneider, et al., 2010) are enclosed in a hermetically sealed glass housings ranging in length from 12 to 32 mm as shown in Figure 37. These tags can be either read only, or read/write (Texas Instrument, 2001). A cylindrical ferrite rod and coil are located at the one end of the tag with the charge capacitor and radio frequency IC chip at the other end.

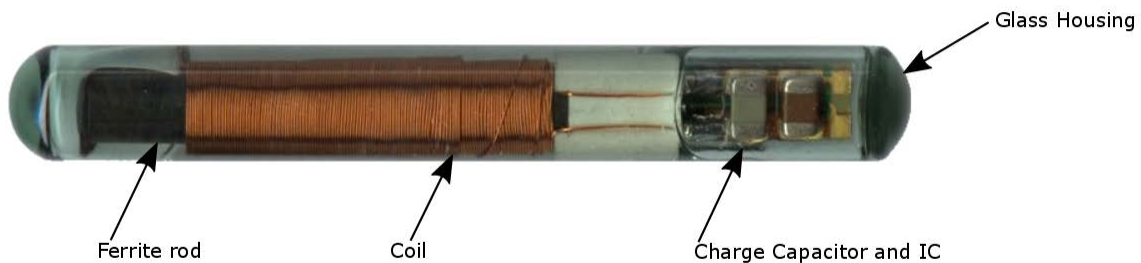


Figure 37 Layout of Glass Transponder (Finkenzeller, 2010)

4.1.2.2 Antenna Design and Detection Ranges

The predominate types of antennae used are stick, gate, and loop antennas. Stick antennas have a focused detection area but their range tends to be small.

With the cylindrical ferrite core and coil of stick antennas, the antenna demonstrate a 4 lobbed detection range profile that is further affected by the orientation of the tag relative to the antenna (see

Figure 38). Gate antennas demonstrate a more uniform detection range at the sides and front and back of the antenna but still have the lobbed characteristic.

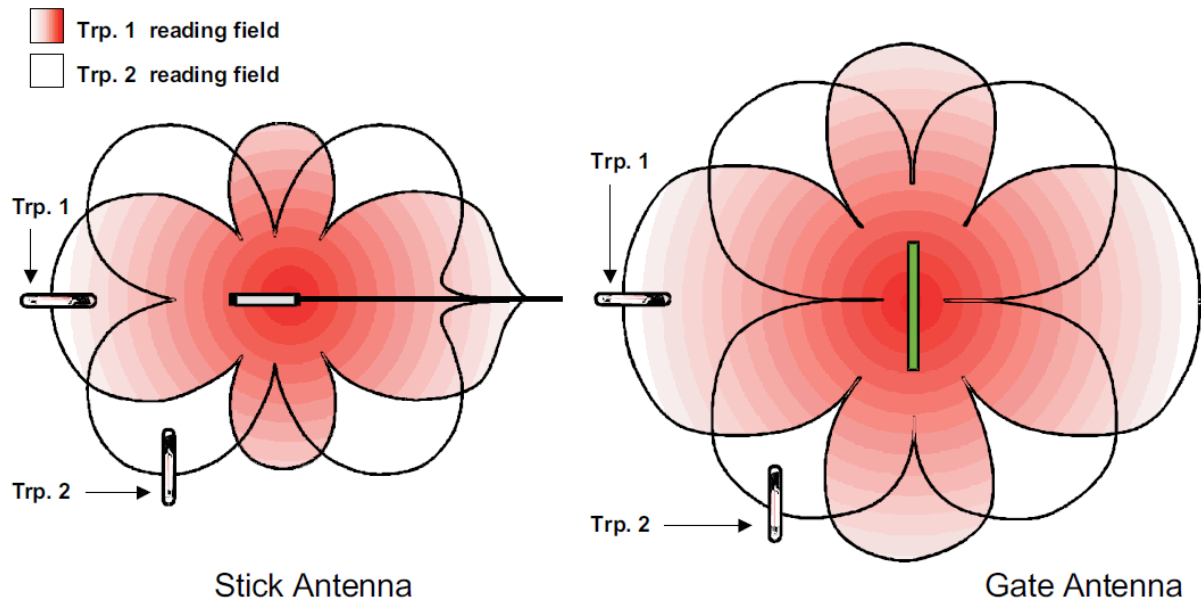


Figure 38 Transponder Reading Field With Stick and Gate Antenna (Texas Instrument, 2002)

Morhardt et al. (2000) conducted read range experiments using a TIRIS S2000 combined tuner, reader and controller using a RI-ANT-S02 stick antenna while testing 23 and 32 mm transponders. For the 32 mm transponders, tests were conducted with the transponder parallel to and perpendicular to the antenna as shown in Figure 39.

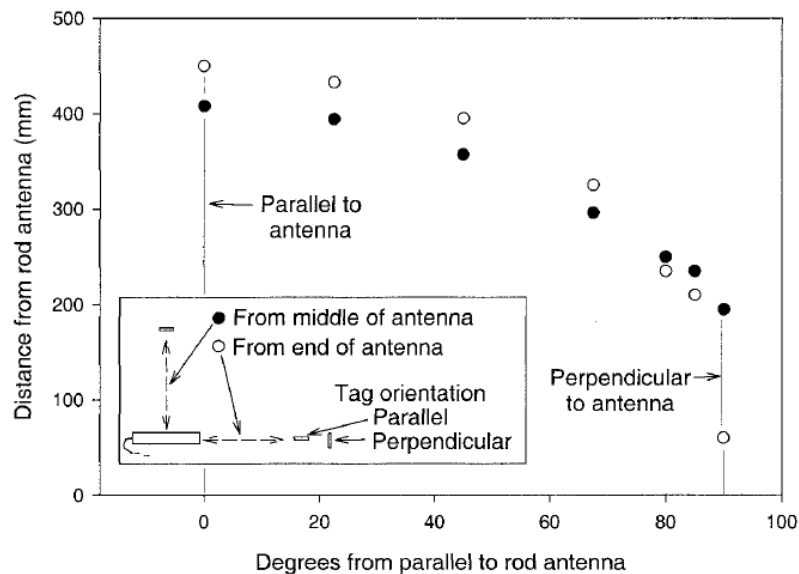


Figure 39 Range of 32 mm PIT tag with RI-ANT-S02 Ferrite Rod Antenna (Morhardt, et al., 2000)

While the maximum detection distance using 32 mm PIT tags was 44.1 cm, similar experiments conducted by Morhardt et al. (2000) on 23 mm PIT tags revealed that the detection distance dropped to 36.3 cm.

Detection range for Lauth and Papanicolaou (2008) study used an RI-ANT G01E gate antenna, RI-ACC-008B-00 tuning module, RI-RFM-008B-00 radio frequency module, RI-CTL-MB2A-03 control module, and 23 mm transponders. Detection range tests were conducted on transponders encased in the glass, concrete/tungsten, and with no casing. The ranges obtain from these tests for transponders oriented parallel and perpendicular with the antenna plane are shown in Table 2

Transponder orientation relative to antenna plane	Glass Casing (cm)	Concrete/Tungsten Casing (cm)	No Casing (cm)
Parallel	40.6	28.0	43.2
Perpendicular	63.5	53.3	67.3

Table 2 Detection Range with RI-ANT G01E antenna and 23 mm transponders (Lauth & Papanicolaou, 2008)

Detection range tests by Schneider et al. (2010) were conducted using 2 different sets of equipment. For one set of tests they used the same configuration as Lauth and Papanicolaou (2008) except for the

different antenna and the control module being RI-CTL_MB2B. The second set of tests were conducted with an Aquartis 53 cm and 84 cm loop antennas and with rectangular flat bed antennas. The read distance with the transponders oriented perpendicular to the antenna plane are provided in Table 3 for reading in air. The reading distance decreased when buried and/or submerged. Chapuis, et al. (2014) found that detection range can be as high as 0.7 m using a loop antenna with 23mm transponders or 0.38 m when using a stick antenna but it is highly anisotropic.

Antenna Design	Transponder Size	
	23 mm	32 mm
Aquartis 53 cm loop	33 cm	41 cm
Aquartis 84 cm loop	49 cm	61 cm
Flat Bed 350 cm x 100 cm	34 cm	66 cm
Flat Bed 400 cm x 100 cm	34 cm	61 cm

Table 3 Detection Range with Aquartis and Flat Bed Antennas (Schneider, et al., 2010)

Schneider, et al. (2010) also tested flat bed antennas where the length was increased from 100 cm to 125 cm, 140 cm, 150 cm, 175 cm and 200 cm. In all cases, the increased length of antenna resulted in reduced read range. Detection Range can be as high as 0.7 m using a loop antenna with 23mm transponders or 0.38 m when using a stick antenna but it is highly anisotropic (Chapuis, et al., 2014).

Using HiTAG readers with a collision avoidance system, two tags perpendicular to each other can be inserted in a clast to reduce the effects of reduce read range with the axis of the tag is not optimally aligned with the antenna (Papanicolaou, et al., 2010; Moustakidis, 2012). The reports by Papanicolaou et al. (2010) and Moustekidis (2012) state that they used a reader developed by “Phillips (HTRM-01 Long Range Reader)” that “incorporates the anti-collision feature, which enables the reader to communicate with a transponder when multiple transponders are located within the electromagnetic field of the excitation antenna”. However, further investigation of the Phillips HTRM-01 reader did not reveal any such product available on the internet. The collision avoidance feature provided promise for improved sediment tracking capabilities, but further clarification of the system details are required before widespread use can be realized.

4.1.2.3 RFID Reader Systems

The predominate sources of RFID reading systems suitable for sediment tracking in North America are Aquartis, which is no longer active, Texas Instruments, which has done substantial work in

developing RFID equipment but provides minimal technical support, Biomark, which actively markets to fish and wildlife research community, and OregonRFID who manufactures and distributes equipment for RFID tracking and provides substantial technical support both before and after sales of their products.

One of the common reader systems mentioned in RFID tracking literature is the Texas Instrument™ RI-STU-251B series 2000 combined tuner-reader-control module (Morhardt, et al., 2000; Lamarre, et al., 2005). The RI-STU-251B has an auto tuner coupled with reader and control module, with the auto tuner suitable for antennas with an inductance range between 26 – 27.9 μH at 134.2 kHz (Texas Instrument, 2000). This system is demonstrated for fish tracking by Morhardt et.al (2000) as shown in Figure 41. Since they use the Texas Instrument™ RI-ANT-S02 stick antenna with an inductance of 27 μH , the antenna can be directly connected to the auto tuning reader. The reader has a serial output which can be configured to automatically send the tag ID every time a tag is detected.

More control and flexibility of the system can be accomplished by using separate reader, controller, and tuner as accomplished by Schneider et.al (2010). They used the Texas Instrument™ RI-RFM-008B reader, RI-CTL-MB2B control module, and RI-ACC-008B tuning board; enabling them to use two different antenna of their own custom design. They experimented with flat bed antennas ranging in width from 3.5 m to 4 m and ranging in length from 1 to 2 m to determine the optimal geometry for maximizing read range. By using a separate tuner module, the range of inductances of the different antenna geometry could be accommodated and driven by the same reader.

To record detected RFID tag numbers, the data needs to be communicated from the reader to some other device via serial communication. There are many options for serial communication with the reader. The reader can be connected to a data logger which can periodically be downloaded to computer or stored on a removable SD card. The serial port from the reader can be directly connected to a palmtop computer (Allan, et al., 2006), connected to the serial port on a desktop computer, or connected through a serial to USB converter. Once the connection is established with a the computer, the serial data can be read on the COM port which the computer has assigned to the serial communication device by using a terminal emulator program such as HypterTerminal which comes with window versions prior Windows 7 or PuTTY (<http://www.putty.org/>) which will can be configured to log data from the serial port and record it to a text file.

The serial data from a reader can also be read by an Arduino micro controller. These are dedicated control units which are becoming popular in educational environments due to their low cost, ease of programming, and direct input and output capabilities. The Arduino can be coupled with an LCD for readout, enabling a low-cost field display to be created. When connecting to an Arduino, a voltage converter chip must be used because serial port standard is for a on bit (1) represented by a -13 volts and an off bit (0) represented by +13 volts (upper chart in Figure 40), wherein the Arduino uses TTL logic in which on bit (1) is +5 volts and an off bit (0) is 0 volts (lower chart in Figure 40). A Max 232 Serial to TTL module (<https://www.sparkfun.com/products/13029>) can provide this require conversion.

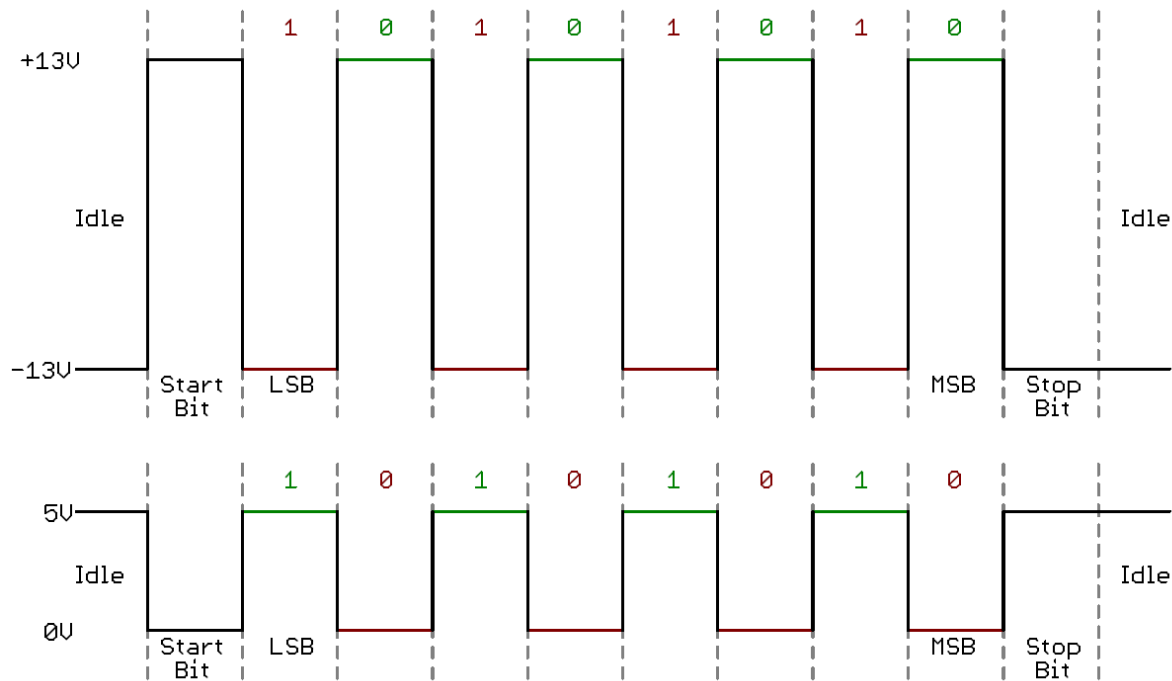


Figure 40 Serial and TTL levels (RS-232 vs. TTL Serial Communication, 2010)

A Bluetooth dongle can also be connected to the serial port on the reader to enable transmission to Bluetooth on a computer (Bradley & Tucker, 2012) or a smart-phone. Bluetooth is a wireless networking technology transmitting radio waves at 2.4 GHz and establishing a small network, referred as a piconet with 2 to 8 nodes. The range of communication is a function of the class of Bluetooth being used as shown in Table 4.

Device Class	Transmitted Power	Intended Range
Class 3	1 mW	Less than 10 meters
Class 2	2.5 mW	10 meters
Class 1	1000 mW	100 meters

Table 4 Bluetooth Device Transmitter Classes (Wright, n.d.)

If a Bluetooth device does not have the class stated, it will likely be a class 2 or 3 device. Because of the higher design requirements of Class 1 devices, the documentation on Class 1 devices commonly states their class designation as seen in products such as the GridConnect Serial to Bluetooth Adapter – Firefly (<http://gridconnect.com/serial-to-bluetooth.html>) or IOGear Long Range Bluetooth USB Adapter (<https://www.iogear.com/product/GBU321/>). The Firefly and IOGear USB adapter can be used together in conjunction with a computer to provide serial communication over Bluetooth. When using this method of communication, the GridConnect Serial to Bluetooth adapter needs to be configured to receive serial communication from the RFID reader at the baud rate set by the reader, while the computer needs to establish a serial connection with the IOGear using the baud rate set on the GridConnect for serial over bluetooth transmission (GridConnect, 2007).

Bluetooth communication can also be achieved between a reader and a cellphone equipped with Bluetooth. Wherein on a Windows based PC, the control panel indicates the COM port designated to the serial port over Bluetooth and the baud rate can be controlled by the user, cell phone users are not provided this level of control. A review of literature and websites indicates that the cell phone may automatically set the appropriate baud rate through the “Remote Port Negotiation Command” (Bluetooth, 2001). This would indicate that if the FireFly’s serial over Bluetooth baud rate is set to a common value such as 9600 or 115200 bps, then the terminal emulator application on the cell phone should automatically query the FireFly and establish port settings.

Rather than using wireless communication, the serial data has also be read directly by a Hewlett Packard 48GX programmable calculator with serial communication capabilities as shown in Figure 41 (Morhardt, et al., 2000). Rather than needing to connect all 9 pins of the DIN 9 serial port, the only pins required for communication are the transmit (TXD), receive (RXD), and ground (gnd) pins. The HP 48GX has been discontinued. However, an HP 50G graphing calculator has the programmable functionality and is equipped this a USB port. By purchasing an HP 50g RS-232 Serial Cable (<http://commerce.hpcalc.org/serialcable.php>) for US\$20, the HP 50C can be connected to read data from a serial device such as an RFID reader.

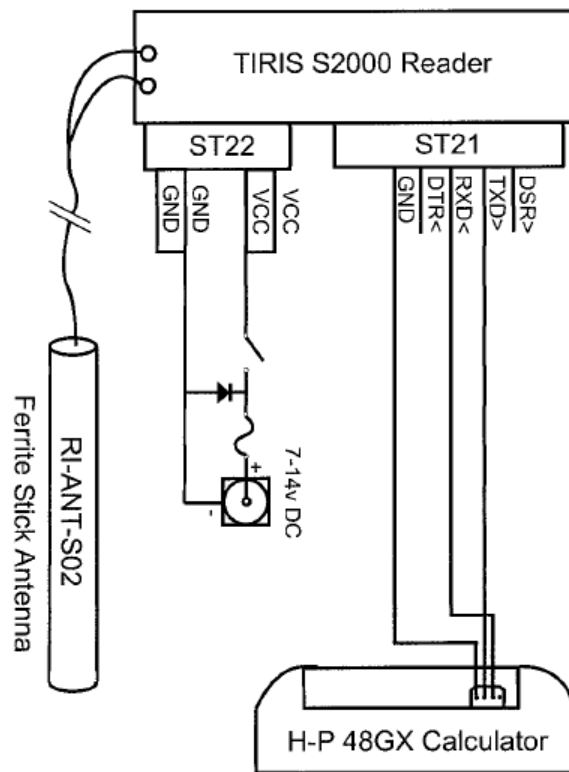


Figure 41 Schematic of connection between antenna, reader and data-logging calculator (Morhardt, Bishir, Handlin, & Mulder, 2000)

4.1.3 Multiplexer Units

While a single antenna is optimal for pinpointing a single PIT tag, due to the small range of these antennas, they can only cover a small area at a time. For wider coverage, multiple antennas can be used through multiplexing, whereby multiple antennas are connected to a single reader. The primary technology for creating a multiplexed antenna application are a data logger, reader module, multiplexer, tuners and antennas (see Figure 42).

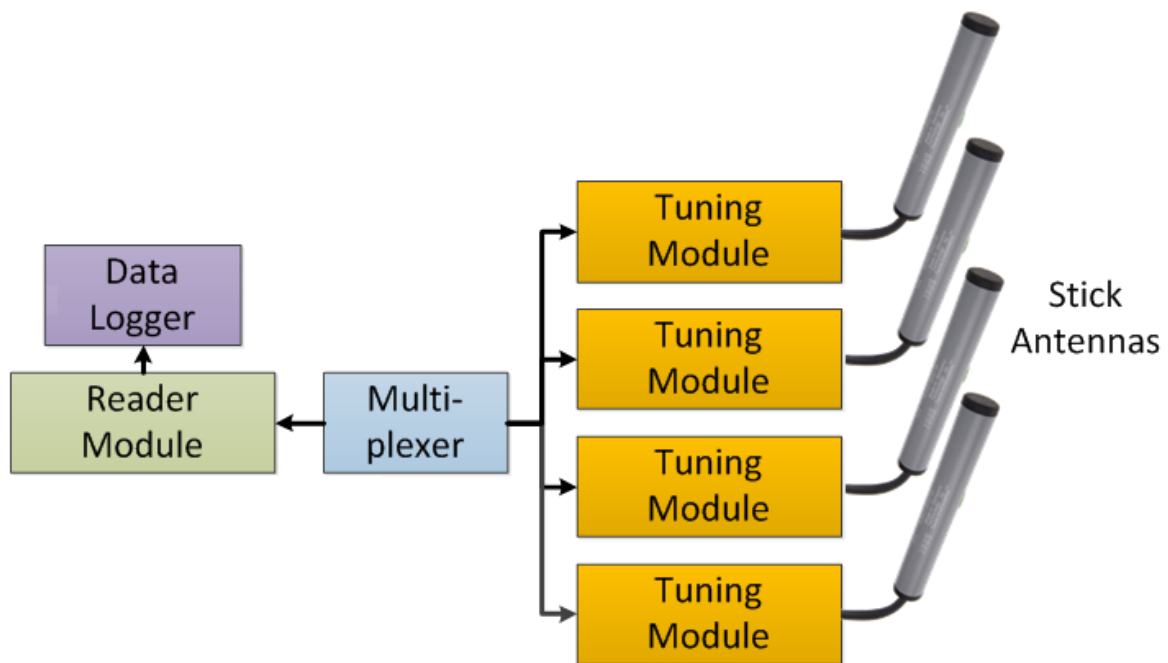


Figure 42 Typical Multiplexed System

Texas Instruments™ developed the RI-MOD-TX8A multiplexer (see Figure 43) for the Series 2000 134.2 kHz RFID product line with the capacity of multiplexing four antennas through tuners attached to the individual antennas, or through a Texas Instruments™ RI-ACC-008B tuning board.

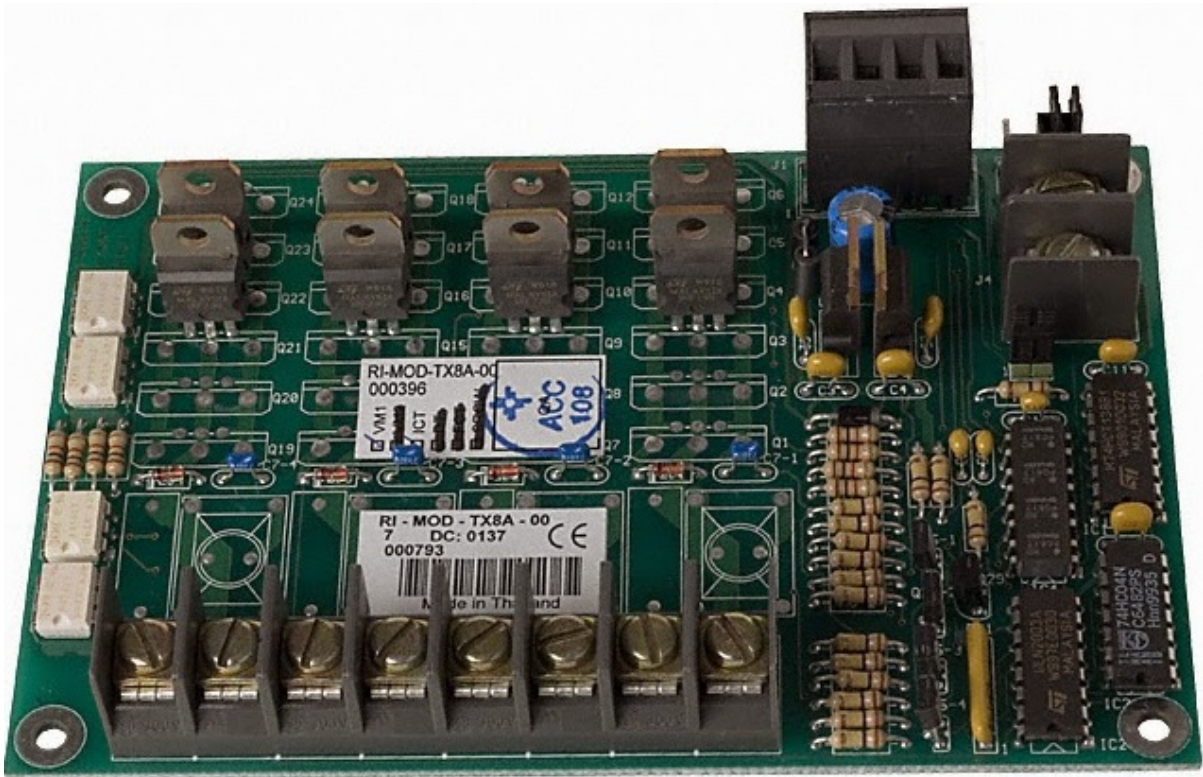


Figure 43 Texas Instruments™ RI-MOD-TX8A multiplexer

The multiplexer could then be connected to a Texas Instruments™ RI-RFM-008 RF module and controlled by Texas Instruments™ RI-CTL-MB2B control module (Figure 44). However, this product has been discontinued by Texas Instruments™ and Oregon RFID has obtained the rights to manufacture and sell this multiplexer as part of a system.

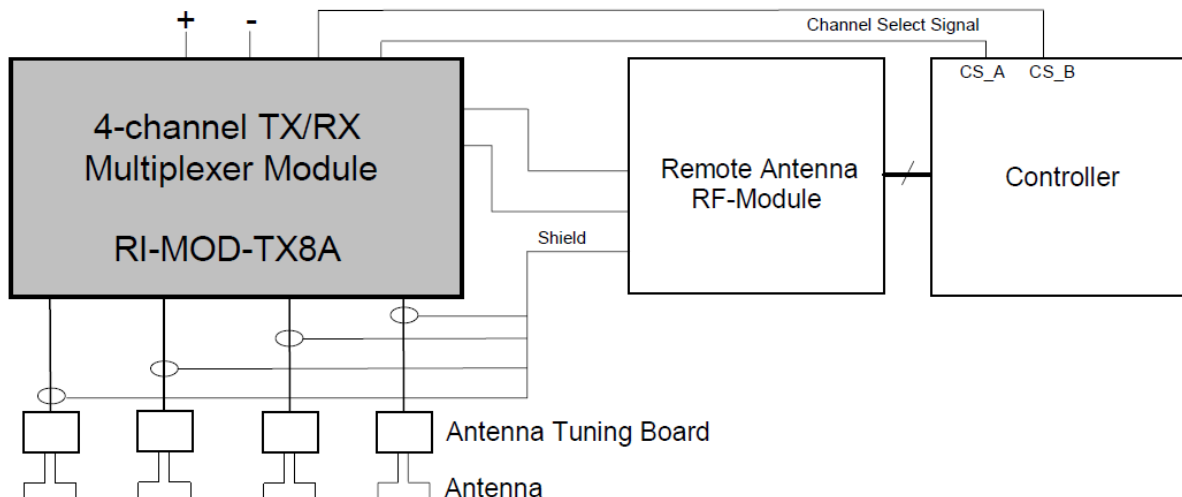


Figure 44 RI-MOD-TX8A Schematic with RF Module and Controller

In discussion with OregonRFID, this RI-MOD-TX8A is not available for sale as an individual module, but must be purchased as part of a package system. The two multiplexing systems considered in this investigation are the Biomark multiplexing transceiver and the OregonRFID reader and multiplexer.

4.1.3.1 BioMark™ Multiplexing Transceiver

BioMark™ specializes in providing RFID solutions for fish and wildlife tracking. They have a RFID reader/multiplexer option composed of the IS1001 (Figure 45) which is a reader and auto-tuner. One of these is required for each antenna. For a 12 antenna system, there would be (12) IS1001 readers controlled by (1) IS1001MTS Master control module which would multiplex all 12 readers and bring the data back to a central location to be read by USB computer interface. Costing details are provided in Table 5.



Figure 45 BioMark IS1001 Reader Module

Qty	Description	Price	Extended Price
12	Stick Antenna	US\$186	US\$2,232
12	IS1001 Reader	US\$1,385	US\$16,620
1	IS1001MTS Master control Module	US\$2,495	US\$2,495
1	Cabling	US\$500	US\$500
	Total Cost		US\$21,847

Table 5 Itemized Costing of BioMark Multiplexing System for 12 Antennas

The BioMark IS1001 and IS1001MTS system is a viable alternative for multiplexing all the readers and communicating back to a central computer with a total cost for the multiplexing at US\$21,847.

4.1.3.2 Oregon RFID HDS Reader Antenna and Multiplexer

As mentioned in section 4.1.3, the model RI-MOD-TX8A 132.4 kHz RFID multiplexer developed by Texas Instruments™ is now available exclusively through Oregon RFID. This product is only sold as part of a package together with control module, RF module, and data logger encased in a water resistant steel enclosure. One packaged unit is designed to multiplex, read, and store the data from up to 4 antennas, requiring external tuning modules for each antenna.



Figure 46 Oregon RFID Multiplexer with Control Module, RF Module, and Data Logger

Multiple multiplexers can be synchronized together to co-ordinate the charge/listen times to avoid interference between devices by declaring one reader as the master and the others as slaves. The multiplexing reader is powered by 12 volts, making it suitable for field applications where it could be powered by a deep cycle marine battery. The RFID tags data detected by the antennas are stored on the onboard data-logger equipped with a removable SD card and serial port. The RFID tag data can also be retrieved instantaneously through the serial port for RFID tracking applications as described in Appendix A for Bluetooth connection and Appendix D for USB connection. The technical support personnel at Oregon RFID have deep experience in building up the electronic solutions and field installations of RFID tracking systems for fish and sediment tracking. The pricing details for all the electronic components required for RFID tracking in the flume are listed in Table 6.

Qty	Description	Price	Extended Price
3	Multi-Antenna HDX Reader Package complete with multiplexer, reader, datalogger, 2 tuner boxes	US\$2,695	US\$8,0850
6	Slim Tuning Capacitor	US\$215	US\$1,290
12	Rod Antenna	US\$186	US\$2,232
1	Cabling	US\$500	US\$500
1	Inductance Meter (evaluate the inductance of the antenna)	US\$245	US\$245
1	HDX Antenna Tuning Indicator	US\$265	US\$265
1	Ceramic Tuning Tool (non-metalic screwdriver for antenna tuner)	US\$14	US\$14
			US\$12,631

Table 6 Itemized Costing of Oregon RFID Multiplexing System for 12 Antennas

The Oregon RFID multi antenna system is the preferred solution due to the lowest cost for a complete package system along with strong technical support and customer service to assist in installation and troubleshooting of the system.

4.2 Design of flume RFID sediment tracking carriage

4.2.1 RFID Carriage Movement Design

The Carriage containing the RFID equipment is designed to traverse back and forth along the length of the flume. As the RFID readers detects tags, this information must be correlated with the current position of the carriage to determine the location of the tagged clast. The carriage movement system needs to be able to move the carriage up and down the length of the flume while relaying back to a computer the position information to enable correlation between tag ID and position. The design involves both the mechanical design, which must ensure that the drive system has sufficient power to move the carriage, and the electronic design for controlling the motor and relaying position information back to a computer.

4.2.1.1 Carriage Movement Mechanical Design.

The mechanical design involved determining the forces required to move the carriage and the appropriate mechanical drive components to accomplish that movement. The maximum slope requirement of 2% for the flume along with friction estimates provides a basis for determining the require forces. Assuming a 200 kg RFID carriage when accounting for the batteries and electronics, an incline plane analysis indicates that the forces which must be overcome to drive the carriage up a

slope are $mg \sin\theta$, which is equivalent to 2% of mg since it is a small angle where m is the mass of the carriage and g is the gravitational force. This results in a force of 39.2 N (8.8 lbs) required to drive the carriage up the 2% slope assuming frictionless movement. Since the carriage will be mounted on neoprene rollers containing rolling contact bearings, the rolling friction could double the required driving force to 80 N (18 lbs).

Since the carriage must change directions, the forces required to accelerate and decelerate the carriage as it moves over 18 m (the 2m of flume at the discharge end have the sediment trap and will not be part of the travel distance) must be considered. The design intent is for the carriage to travel the length of the flume in 30 seconds. The acceleration is minimized by assuming constant acceleration for the first 9 meters and constant deceleration for the last 9 meters of travel in each direction. Therefore, 9 m will be covered with constant acceleration in 15 seconds. The applicable kinematic formula as described in equation 2 yields an acceleration of $a = 0.08 \text{ m/s}^2$.

$$d = \frac{1}{2}at^2 \quad (2)$$

The force required to accelerate the 200 kg carriage at this rate is 16 N or 4 lbs yielding a total required force of 96N (22 lbs).

To account for rolling surface irregularities, higher than anticipated friction rates and shorter acceleration times, the design will be based on 222N (50 lbs) of driving force.

The mechanical driving system needs to deliver the above determined force to the carriage to transport it back and forth along the flume. Among the potential options for delivering this movement are rack and pinion systems similar to the system used in steep mountain tram rail applications, ball screw or lead screws, and cogged timing belt systems.

4.2.1.1.1 Rack and Pinion Drive

The rack and pinion drive system would have a rack mounted along the length of the flume with the pinion and drive motor mounted on the RFID carriage. Since individual racks are supplied in maximum 2 m lengths, adjacent racks would need to be precision mounted to the flume structure to ensure the pinion did not jump a tooth between sections. By mounting 2 racks, one on each side of the flume support structure, balanced forces could be applied to both sides of the carriage to ensure the carriage rollers did not bind as they moved. The pinion drive would need to be part of the RFID

carriage with power either stored on the carriage or a retractable wire track used to move the wires along with the carriage. This system would result in mechanical vibrations from the meshing of the gears, operation of the pinion drive motor, and movement of the wire track. These vibrations would transmit into the flume and disrupt the ultrasonic flow measurement equipment. The rack and pinion systems are applicable to environments where a large amount of force is required and vibration considerations are not paramount in the decision process, but for the RFID carriage application this type of design is sub-optimal.

4.2.1.1.2 Screw Drive

A ball screw or lead screw drive design provides smoother operation than the rack and pinion design but the screws for these drives are limited in length to under 5 meters requiring a threaded joint at the interface of adjacent lead screw to enable attachment and power transfer to subsequent screws. Due to the precision machining required in manufacturing lead screws, the screws are very high cost. Lead screws and ball screws are commonly used in applications with movement under 2 meters and precision down to 0.01 mm. Our application required larger lengths of travel with the required precision of 10 mm, making the screw drive options excessively expensive and complex for this application.

4.2.1.1.3 Cogged Belt Drive

Cogged belt drive systems are available with either close loop or continuous belting. Closed loop cogged belts are applicable for designs where power is being transmitted between pulleys that are under 2 meters apart. The continuous belting can be used for creating a continuous loop system that incorporates a splice at the object being moved back and forth. For the RFID carriage application, a section of continuous belting could be formed into a loop around pulleys at each end of the intended travel distance with the ends of the belting spliced together at the RFID carriage. The continuous belting can accommodate driving the carriage over the length of the flume without requiring the connection of multiple drive components as is required for the rack or screw drives. Cogged belting is also available in Kevlar reinforced urethane designs, minimizing the mechanical vibrations created from driving the carriage. The drive motor would be mounted to the concrete floor with a closed loop timing belt connected to a drive shaft mounted between the W16x100 beams in flume support structure. This would minimize motor vibration transmission to the flume structure. The continuous belting could run on pulleys mounted at the center of the shafts located between the W16x100 beams

providing centerline force to the carriage and minimizing lateral forces caused by a system that only drives the carriage on one side. Since the cogged belt drive system is capable of driving the carriage the entire length of intended travel with a single piece of continuous belting while minimizing vibration and providing sufficient accuracy for this application, this is the preferred drive system for this application.

Cogged belts are available in a range of sizes based on the required drive force and the precision parameters. The XL style timing belt has a maximum load rating of 157 lb per inch of belt width for Kevlar reinforced urethane cording. This could be obtained in 1/2" wide belting with sufficient capacity to drive the carriage. However, the type XL Timing Belts pulleys are only supplied with key and set-screw designs for transmitting torque from the shaft to the pulley. With the repeated reversal in torque for this application, the key would start to rock back and forth in the keyway, gradually working the setscrew loose, widening the keyway in the shaft and bushing, and wearing down the key. This would eventually result in the pulley spinning on the shaft. This loosening over time can be eliminated by a system that creates a positive lock on the shaft. An interference fit between the shaft and hub would create this positive lock fit but pressing a hub down half the length of the shaft would result in hub to shaft assembly problems due to the required forces and the damage to the hub and shaft in pressing it this distance. The positive lock can also be accomplished by taper lock quick disconnect (QD) tapered hubs and bushings that use bolts on the face of the taper bushing to drive a taper between the shaft and hub and use a separate set of threaded holes on the face of the taper to pull the taper out from between the hub and shaft. The L and H Series timing belts come with QD bushings. The minimum load rating for L series is 207 lb/in and is available in 1/2" wide stock. The preferred cogged belt design for the RFID drive system is type L series belting with QD type bushings drive pulleys as detailed in Appendix E.

4.2.1.2 Automation of Motion Control

The design of the automation for motion control involves selection of a type of motor and gear drive, method for controlling that motor, and communication about position of the carriage back to the computer to correlate position with RFID tag detection. The motor choices considered include servo motor and DC motors. Each control scenario involved a motor attached to a gear reducer which drive a cogged pulley belt connected to the drive pulley for moving the RFID carriage (see Figure 47,

Figure 48, and Figure 50). The method for controlling the motor include a PLC and Arduino micro controller.

4.2.1.2.1 Servo Drive with PLC

The motion control by a servo motor includes a PLC which controls a servo drive and receives position information from an optical encoder mounted to the servo motor (see Figure 47).

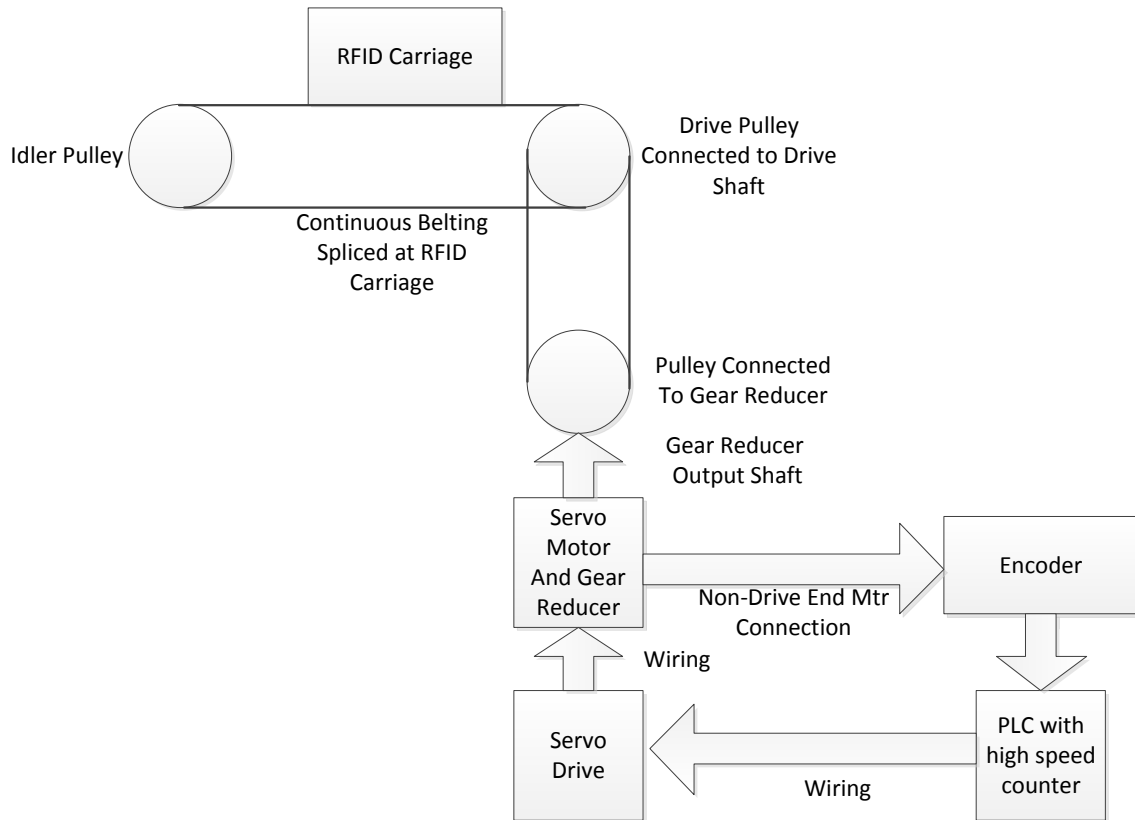


Figure 47 Servo Motor and PLC Schematic Diagram

The pricing details for a servo motor and drive system are provided in Appendix F, with a total cost of \$7,712 for the servo drive and matching PLC control system. The model R88M-K40030T-S2 servo motor in this system is equipped with an incremental encoder with an accuracy of 262,144 pulses per revolution or 0.00137 degrees. The servo is attached to a 25:1 gear reducer resulting in an output shaft accuracy of 6,553,600 pulses per revolution. There is a 1:1 drive ratio between the gear reducer shaft output and the shaft driving the continuous belting. The pulley driving the continuous belting is 18 teeth, 3/8 pitch resulting in a circumference of 6.75". This results in a positional accuracy of 1 μInch

or 26 μM . The servo system has a much higher level of accuracy than required which affects the high cost for the system.

4.2.1.2.2 DC Motor with Arduino

Motion control could also be achieved using an Arduino micro controller. For this investigation, an Arduino is coupled to a DC motor which can be controlled by an analog voltage level input to a DC motor controller as shown in Figure 48. Position information would be obtained from an ultrasonic distance sensor providing information on the location of the RFID carriage directly back to the Arduino.

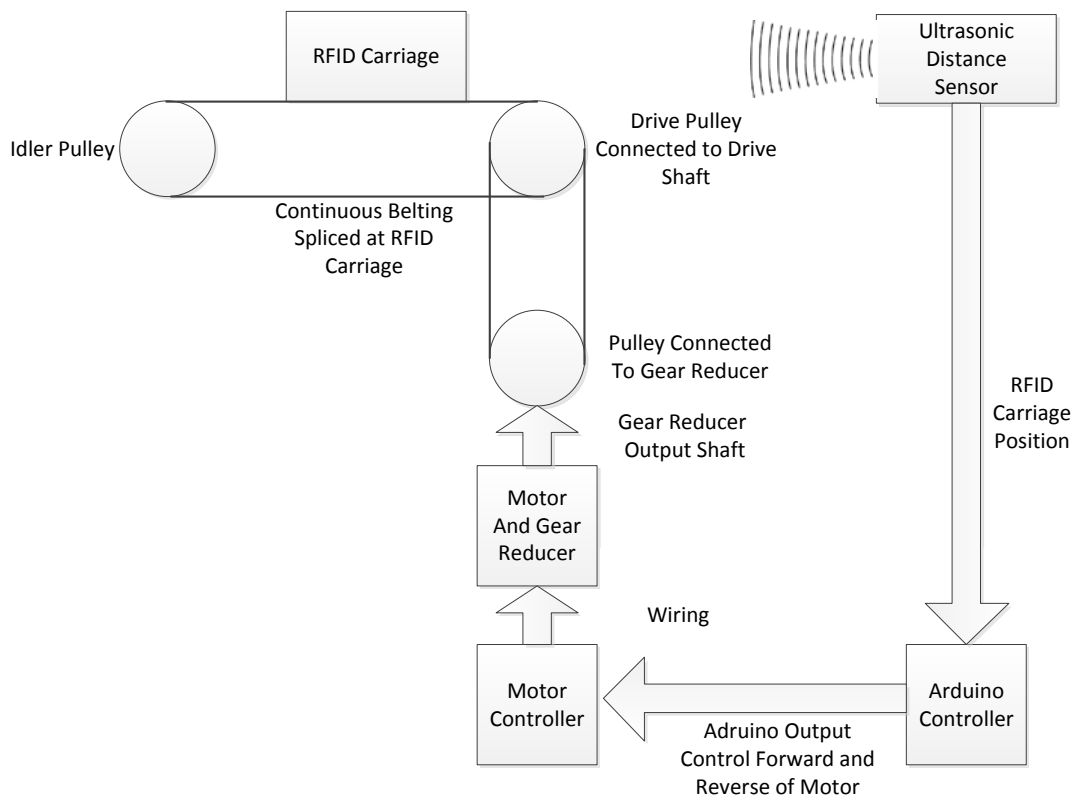


Figure 48 Arduino Motion Control Schematic Diagram

Arduino are microchip controllers that have been mounted on a printed circuit board with inputs and outputs directly wired to the microchip. They are designed for low cost educational applications, enabling an Arduino to be purchased for under \$50. Due to their simplicity, they do not have isolation circuitry for their inputs and outputs, meaning that voltages spikes coming from the motor or other equipment can conduct back to the Arduino and burn out the microchip. The Arduino is also not

equipped with a true analog output, rather they use pulse width modulation (PWM) to simulate analog voltage as show in Figure 49 where a 0% duty cycle would be 0 volts, a 25% duty cycle is simulating 1.25 volts, up to a 100% duty cycle simulating 5 volts. This form of control can be applicable for managing a light where the reduced duty cycle effectively reduces the quantity of illumination created, but PWM waveforms applied to a dc motor controller would cause the motor controller to be rapidly switching between full voltage and no voltage which would burn out the motor controller and motor.

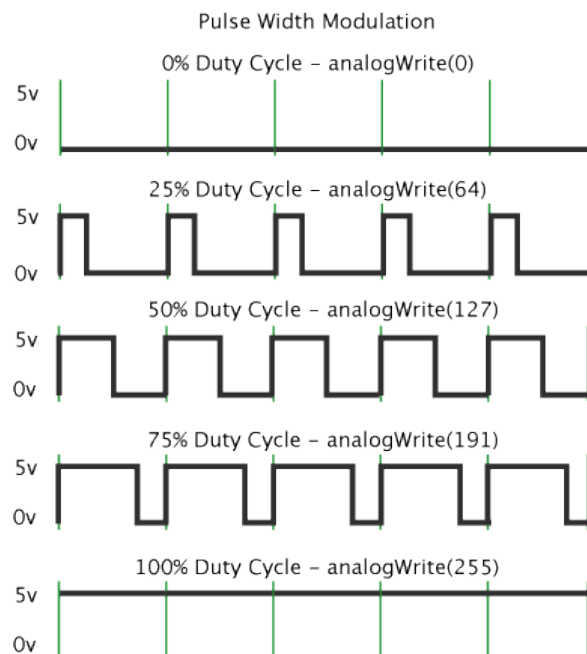


Figure 49 Pulse Width Modulation (PWM, n.d.)

For the Arduino to be used effectively in the control of the DC motor, it would need to be coupled with isolation circuitry and a digital to analog converter. Such circuitry can be rapidly prototyped on a breadboard circuit project, but to provide the reliability required for continuous operation of the RFID carriage in sediment transport experiments, a custom printed circuit board would need to be built with all the components soldered in place. After the entire circuit is soldered together, testing and troubleshooting would need to be conducted on the entire system to ensure the design intent was being realized. Even though the Arduino presents a low cost control alternative, the amount of development time and dedicated skill required to implement this design are outside the skills of the regular personnel involved in sediment transport research.

4.2.1.2.3 DC Motor with PLC and 4 state Motor Controller

The third design considered was to use a PLC with limit switch inputs to indicate when the motor needed to change direction, and directly switch between preset voltage levels supplied to the motor controller to switch between forward and reverse motion. An Allan Bradley Micro810 series PLC can control a DC motor by its 4 relay outputs controlling a KB8833 multispeed board with 4 preset speed and direction settings directly mounted on the KBMB 212D DC motor drive (see Figure 50).

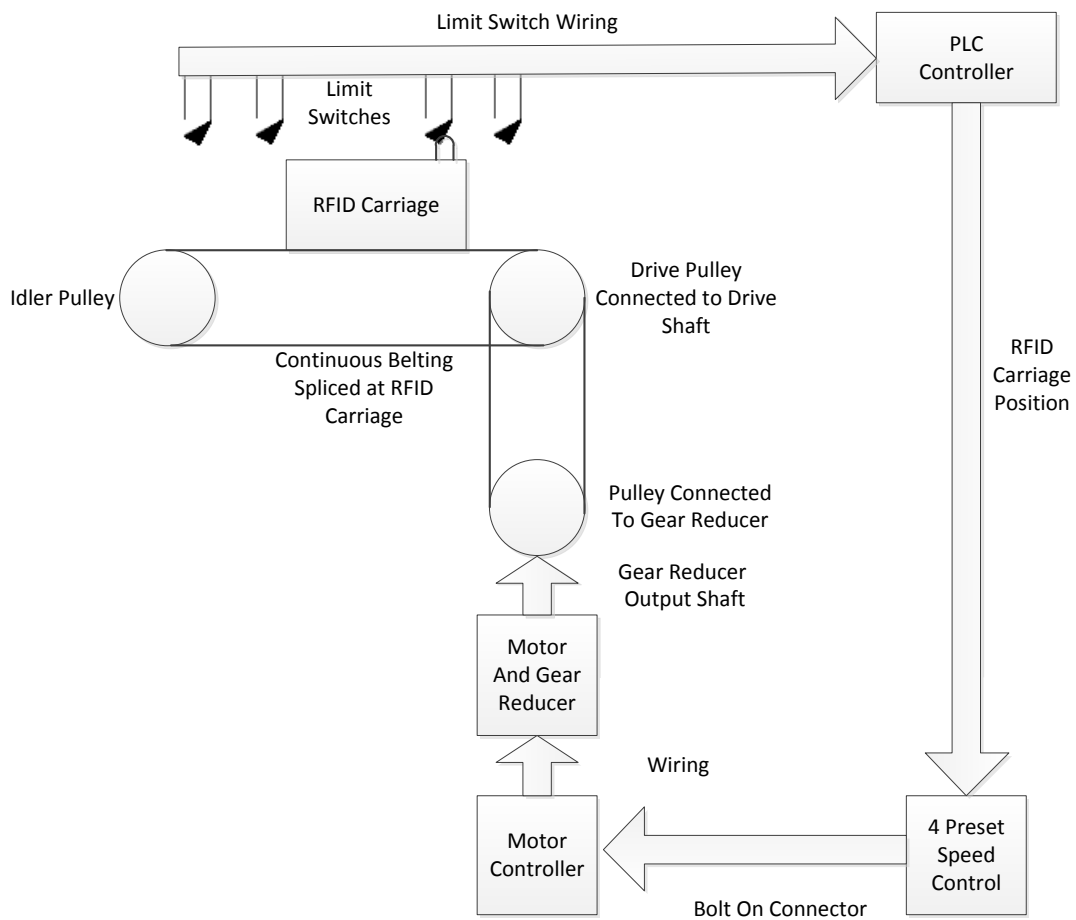


Figure 50 DC Motor with PLC Control Schematic Diagram

The PLC functions to move the carriage back and forth between the end point limit switches. Additional limit switches are used within 1 m of the end points to communicate to the PLC that the carriage is approaching the endpoint and needs to reduce speed as described in Appendix B.

Exact position information is provided by a Flue 414D laser range finder modified with a Porcupine LR4 USB interface transmitting instantaneous carriage position to a personal computer through a USB connection.

The PLC controlled a DC motor, when coupled with the laser range finder, provides 1 mm accuracy while enabling an economical PLC and drive system to be employed that has built in isolation circuitry to enable it to withstand voltage spikes common in motor control applications. The PLC program (refer to Appendix B), requires only 8 lines of logic making it easy for personnel to understand the PLC program and make future modifications. The software used to program the PLC, Rockwell Connected Components Workbench, is free for download, enabling subsequent researchers to install the software on their computers and modify the PLC logic to suit individual experiments.

4.2.2 RFID Carriage Assembly

The RFID electronics, antenna, and power supply are contained in the carriage assembly (see Figure 51). The aluminum frame supports the entire assembly on wheels to facilitate transport of the RFID electronics down the length of the flume. While the wheels on the outside of the frame provide vertical support, wheels located on the underside of the frame in each of the 4 corners maintain alignment of the carriage during travel. The drive belt is mounted to a bracket on the centerline of the underside of the frame underside to minimize torque applied to the frame. The antennae are mounted on a PVC support frame with 6 of the antennae angled forward 30° and the other 6 antennas angled backward 30°. This configuration allows the antennae to detect RFID tags before and after steel frames even if detection is blocked while directly under the steel frames. Each antenna is paired with a tuner, with the banks of four tuner outputs going to each multiplexing RFID reader. Each multiplexing reader cycles through sending a charge single to each of its antennas and listening for a response single from RFID tags within detection range. The three multiplexing readers are synchronized together so charge signals transmission and response signal reception on each antenna occur simultaneously. The multiplexing readers are powered by 3 deep cycle marine batteries connected in parallel. The serial port on each multiplexing reader data logger is connected to a Bluetooth dongle to communicate tag ID and antenna ID to the stationary computer (Appendix A).

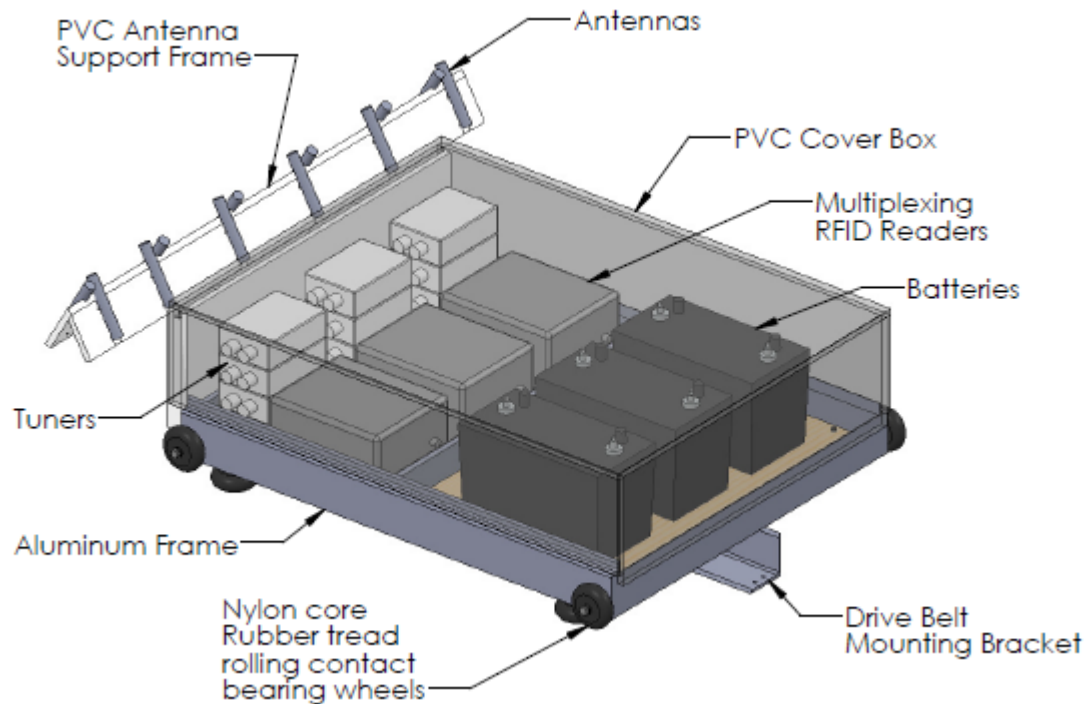


Figure 51 RFID Carriage Assembly

By reading from the twelve antennas which span the width of the flume while the carriage traverses down the length of the flume, the identification of any RFID tags which are detected by the RFID reader system are instantaneously transmitted via Bluetooth to the stationary computer logging the time when each transmission occurs. Carriage motion is achieved by a DC motor driving a cogged belt system. Control of the motor is accomplished by a PLC which reads limit switches at the ends of the travel to determine when to change direction and can also be overridden by user activated pushbuttons to only scan a portion of the flume (see Appendix B for details). The exact position of the carriage at any time is fed to the computer using the laser range finder, where the distance and time are continuously logged. Predictions of the exact location for the RFID tags is accomplished by post processing detailed further in Chapter 5.

Chapter 5

Experimental Results Demonstrating RFID Carriage determined Positions of Particles.

Experiments were conducted with the RFID carriage to confirm the viability of tracking the location of PIT tagged sediment and the overall success of the flume and carriage design. Previous studies quantifying the detection range of RFID tags (Schneider, et al., 2010) have established that the detection range is not substantially affected by air or water, so the tests were conducted in the dry flume. These tests were conducted with a 23 mm RFID tag mounted vertically in the RFID test assembly (Figure 52) with the test assembly on the PVC flume floor. The test assembly had holes spaced 1 cm apart in the stream wise and lateral direction, which allowed the precision placement and orientation of the RFID tags. This assembly also enabled tests with multiple tags to observe their effect on detection accuracy. The RFID test base had a light friction fit with the support legs, enabling the test base to be moved up and down to evaluate the height of the detection range without requiring clamps to hold the test base at the required height.

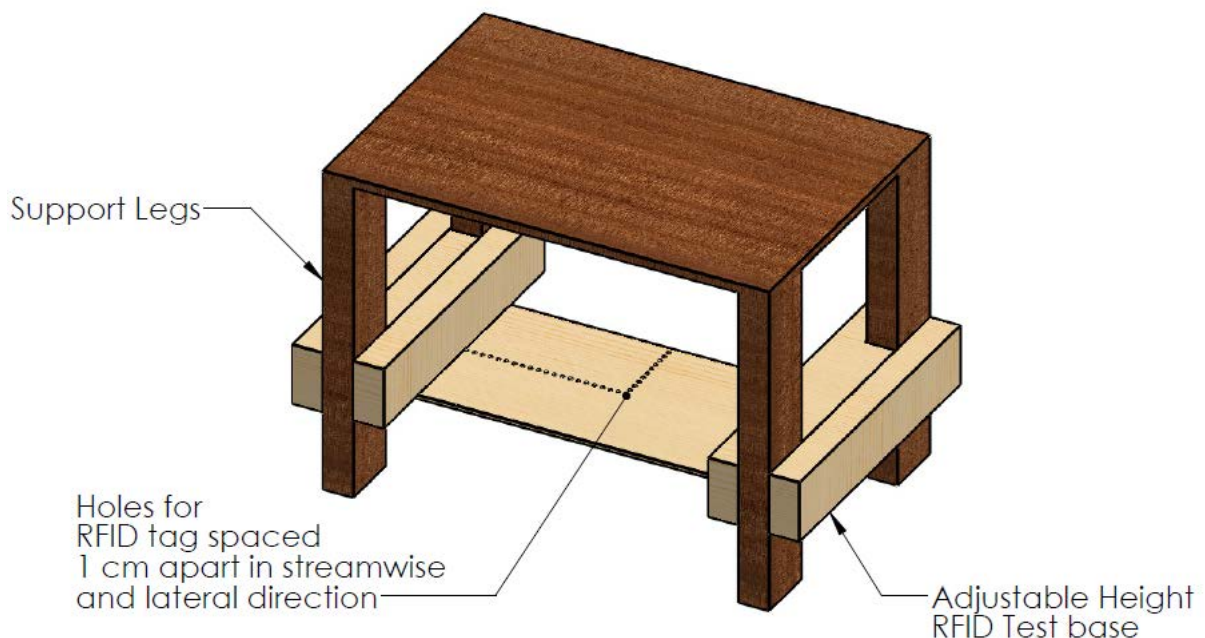


Figure 52 RFID Test Assembly

Initial tests were conducted with the RFID tag located in an area of no steel cross bracing within 60 cm of the RFID tag to identify the optimal detection scenario. Tests were subsequently conducted with the RFID tag directly over a 7.6 cm wide steel cross brace to quantify the effect of the steel brace on blocking RFID tag detection. Tests were also conducted with the RFID tag traversed across the width of the flume to quantify the lateral position prediction capabilities of the rack of antennas. Lastly, tests were conducted with two RFID tags to quantify the effects of collision on tag detection.

All twelve antenna were activated to detect RFID tags during each of the tests. The antennas were giving a descriptive identifier based on the location relative to the flume centerline and whether the antenna is angled forward or backwards as provided in Table 7. Lateral position is measured relative to the flume centerline with positive values towards the left when viewing in the downstream direction.

Antenna Number	1	2	3	4	5	6	7	8	9	10	11	12
Lateral Position (cm)	+53.3	+50.2	+34.5	+31.4	+12.6	+9.4	-9.4	-12.6	-31.4	-34.5	-50.2	-53.3
Angle	-30°	+30°	+30°	-30°	+30°	-30°	+30°	-30°	+30°	-30°	-30°	+30°

Table 7 Antenna Number, Position, and Angle

5.1 RFID Tag Detection with no Steel within detection range.

Detection tests were conducted with the RFID tag located midway between support beams at 3.05 m from the head of the flume. The multiplexing readers on the RFID carriage would transmit a tag ID every time a tag was detected on one of the antennas. The RFID tag was located along the centerline of the flume resulting in antennas 5 to 8 (controlled by the second multiplexer) receiving response signals. A series of tests were conducted with the RFID tag maintaining the same stream wise, and lateral position while the height of the RFID tag above the flume bed was varied. As can be seen in Figure 53, the RFID tag was detected up to 21 cm above the flume bed with the range of detection markedly decreasing when the elevation of the tag was above 10 cm. Detection range may be reduced by up 10% to 15% when detecting through a bed of sediment and water (Schneider, et al., 2010).

The detection range for antennas 5 (+12.6 +30°) and 7 (+12.6 +30°) are wider than the range for antennas 6 (+9.4 -30°) and 8 (-12.6 -30°) with the centroid of detection for antennas 6 and 8 biased towards the upstream direction. However, the average of all the detection points are within 0.02 m of the actual RFID tag location (see Table 8).

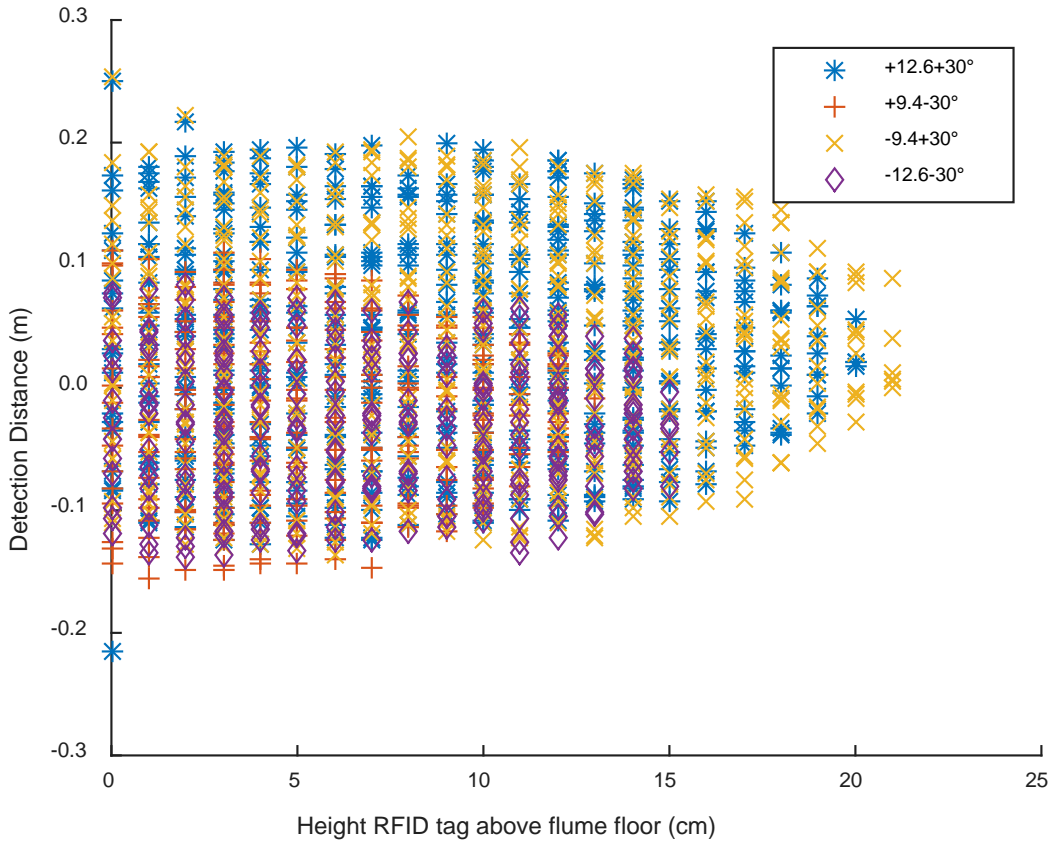


Figure 53 Detection Cloud with no steel shadowing

Minimum Detection Location (m)	Maximum Detection Location (m)	Average Distance of Detection (m)
-0.21	0.25	0.02

Table 8 Detection Range with no steel shadowing

Bar charts representing the minimum and maximum location of detection for each of the antenna at 0, 5, 10, 15, and 20 cm above the flume bed are provided in Figure 54 and summarized in Table 8.

Using the average of the maximum and minimum detection range of each antenna that detected a tag, the estimated stream wise position was found to be within 1 cm of the actual position for heights up to 15 cm above the flume bed, provided that only one RFID tag was present and no steel cross beams were located within 60 cm of the RFID tags. The prediction accuracy obtained from these test indicate that any time delays occurring in the multiplexing reader processing information,

transmitting it via serial communication over Bluetooth, and reading and logging data from the serial ports on the stationary computer are not resulting in a noticeable loss in precision. All tests were conducted with the RFID carriage traversing in both directions. This meant that any time delay occurring when transmitting the ID of a detected tag in the downstream direction would also occur when transmitting in the upstream direction. By averaging the maximum detection distance along with minimum detection distance, any consistent time lag in the system would be averaged out. The accuracy of the predicted location indicated that any time lag which occurs is predominately consistent even though the multiplexer is continually switching between 4 different antennas, and the data is being received and logged by a computer with a Windows 7© operating system doing multitasking. The tests demonstrate that a standard personal computer with a Windows© operating environment simultaneously reading from 3 multiplexing and a laser range finder can provide sufficient accuracy to predict the stream wise position of RFID tags in the flume.

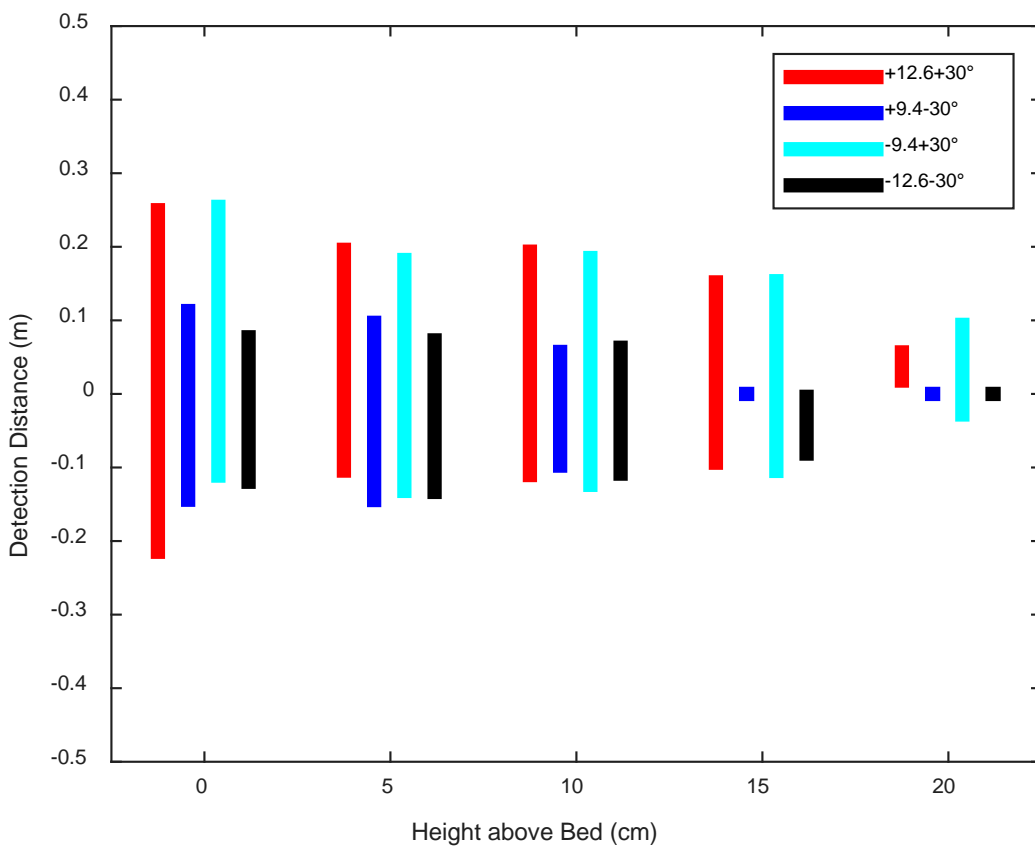


Figure 54 Minimum and Maximum Detection with no steel shadowing

Height (cm)		Antenna Number, Position (cm), Minimum and Maximum Detection Location (m)				Avg. (m)
		5	6	7	8	
		+12.6 +30°	+9.4 -30°	-9.4 +30°	-12.6 -30°	
0	Min	-0.215	-0.144	-0.111	-0.119	0.01
	Max	0.250	0.113	0.254	0.077	
5	Min	-0.104	-0.144	-0.132	-0.133	0.00
	Max	0.196	0.097	0.182	0.073	
10	Min	-0.110	-0.097	-0.124	-0.108	0.01
	Max	0.193	0.057	0.185	0.063	
15	Min	-0.093		-0.105	-0.081	0.00
	Max	0.152		0.153	-0.004	
20	Min	0.018		-0.028		0.04
	Max	0.056		0.094		

Table 9 Minimum and Maximum Detection with no steel shadowing

5.2 RFID Tag Detection with Steel Support Beam

Detection tests were conducted with the RFID tag located at 2.44 m from the head of the flume, directly over a steel support beam. These tests were conducted in the same manner as those documented in section 4.1 with only the height above the flume floor varied for the subsequent tests. Detection results are shown in Figure 55 and summarized in Table 10. The same general detection envelop observed without the steel bracing was observed with the steel bracing. One small difference was that RFID tags were only detected up to 20 cm above the flume floor rather than at 21 cm above the flume floor. Detection was also achieved when the tag was directly on the flume floor at which point the centroid of the RFID tag was 3 cm above a 7.6 cm wide steel beam.

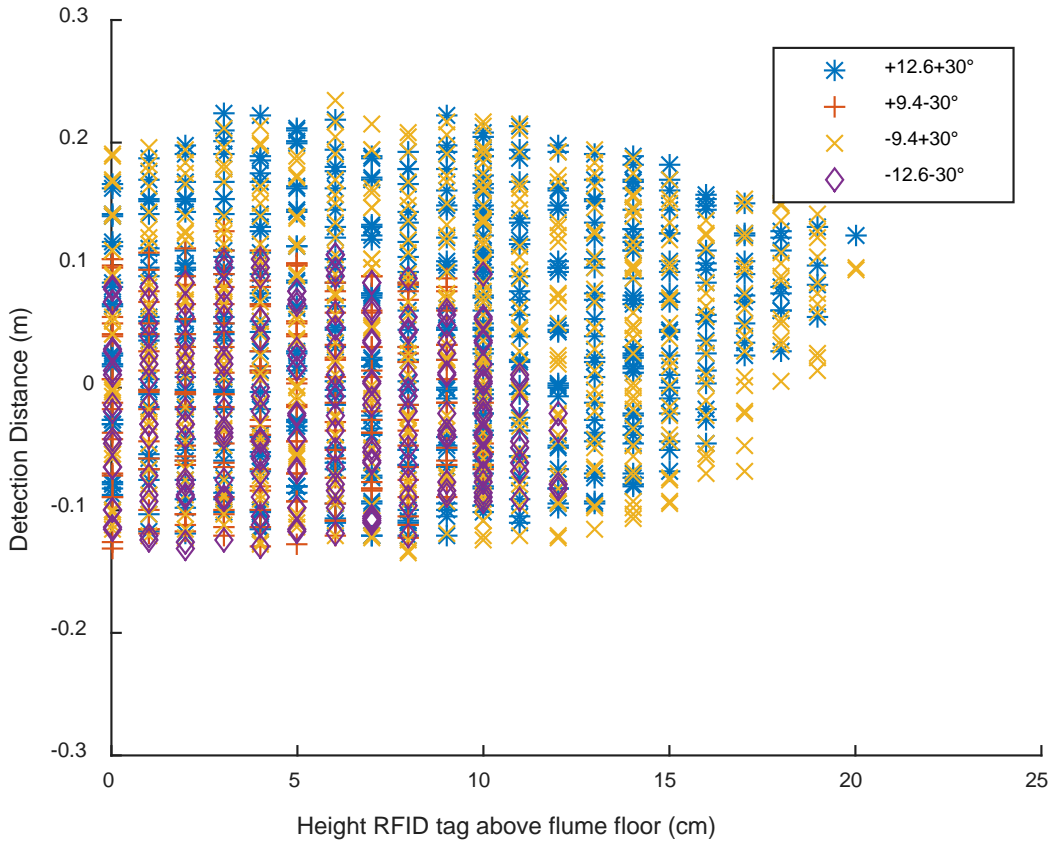


Figure 55 Detection Cloud at steel seam of flume sections.

Minimum Detection Location (m)	Maximum Detection Location (m)	Average Distance of Detection (m)
-0.13	0.23	0.03

Table 10 Detection Range at steel seam of flume sections

Bar charts representing the minimum and maximum location of detection for each of the antenna at 0, 5, 10, 15, and 20 cm above the flume bed are provided in

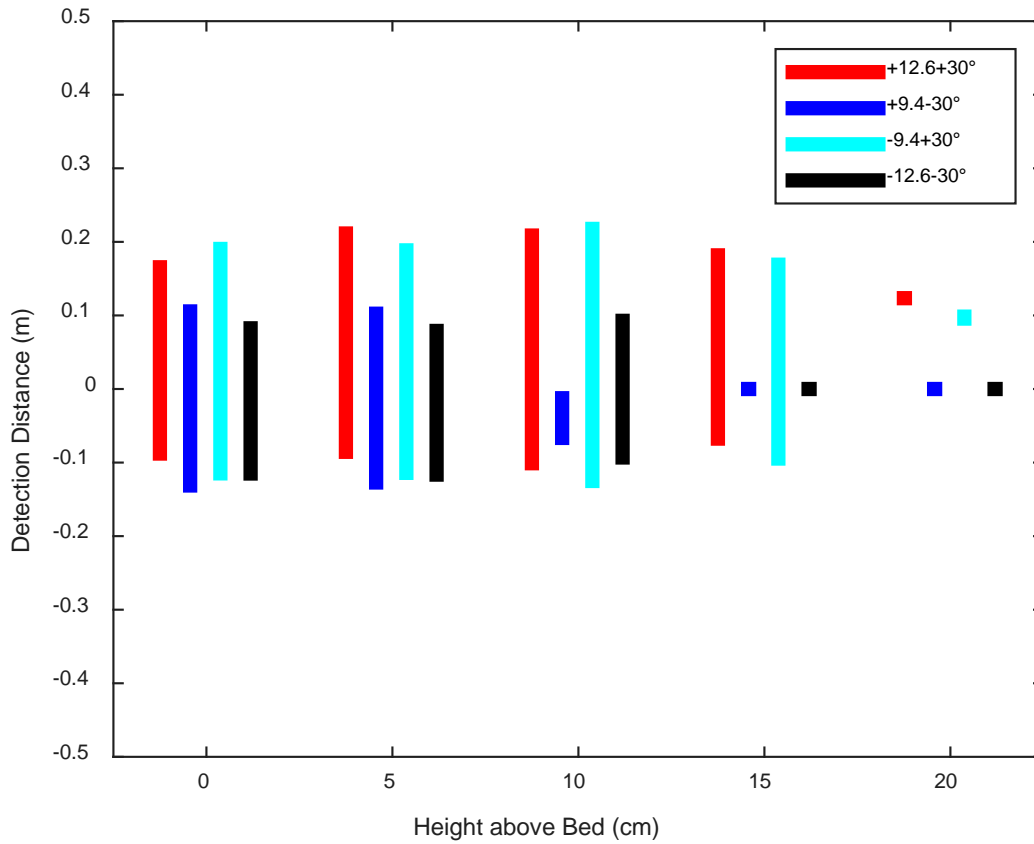


Figure 56 and summarized in Table 11. The detection range for individual antennas varied more as the height above the flume increased. The prediction of RFID tag stream wise position was within 2 cm of actual position up to 10 cm above the flume floor. At 15 and 20 cm height above the flume floor, less of the antennas provided a detection range then in the tests in Section 4.1 where no steel beams were present.

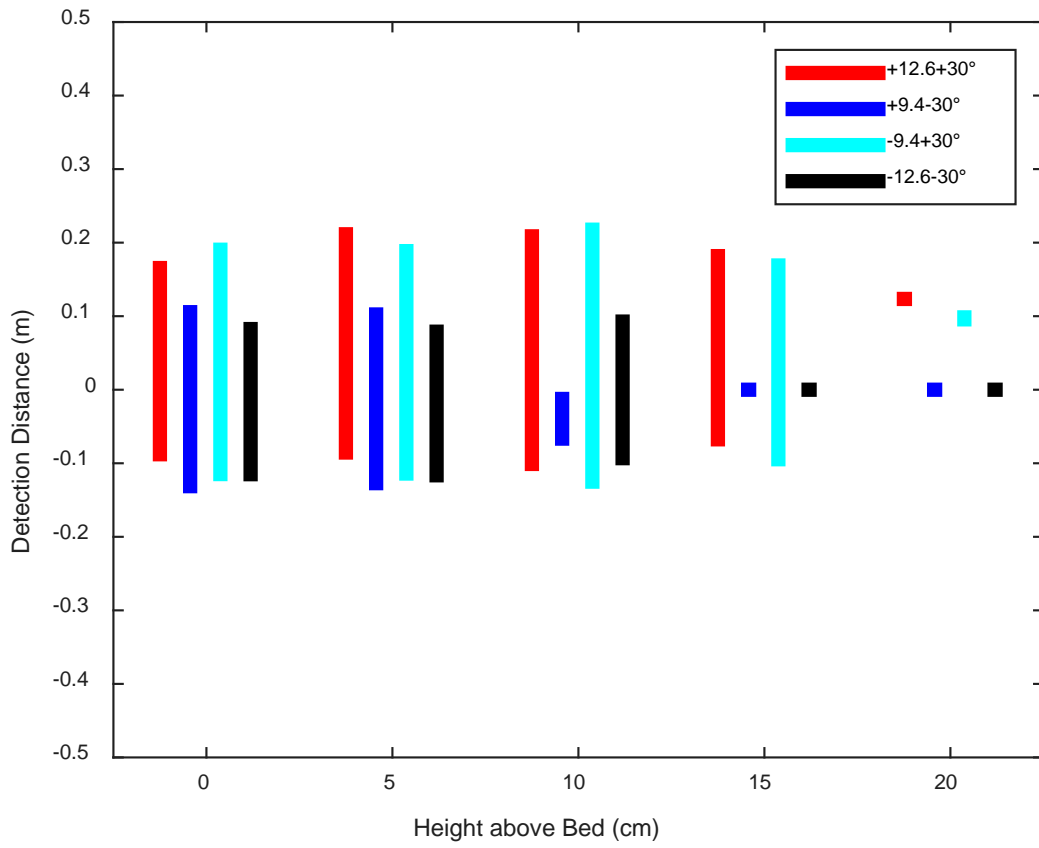


Figure 56 Minimum and Maximum Detection at steel seam of flume sections

Height (cm)		Antenna Number, Position (cm), Minimum and Maximum Detection Location (m)				Avg. (m)
		5	6	7	8	
		+12.6 +30°	+9.4 -30°	-9.4 +30°	-12.6 -30°	
0	Min	-0.088	-0.131	-0.115	-0.115	0.01
	Max	0.165	0.105	0.190	0.082	
5	Min	-0.085	-0.127	-0.114	-0.116	0.02
	Max	0.211	0.102	0.188	0.079	
10	Min	-0.101	-0.066	-0.125	-0.093	0.02
	Max	0.209	-0.013	0.218	0.093	
15	Min	-0.067		-0.095		0.05
	Max	0.182		0.169		
20	Min	0.123		0.096		0.11
	Max	0.123		0.098		

Table 11 Minimum and Maximum Detection at steel seam of flume sections

The detection bar chart and summarizing table indicate that in the presence of a steel beam, RFID tag detection still occurs but the error in predicting the stream wise location increased to 2 cm rather than 1 cm as is the case when no steel beam interferes with RFID detection.

5.3 Traverse RFID tag across flume

Detection tests were conducted traversing the RFID tag across the width of the flume at 2.94 m downstream incorporating all 12 antennas. The results of RFID tag detection are shown graphically in a surface plot (Figure 57) that shows the detection range along with traverse test location and antenna position. Traverse test location and antenna locations are measured from the flume centerline with the east direction right side when looking downstream (east direction) representing the negative measurements and the left side being positive. Tests were conducted every 5 cm across the flume starting with -55 cm from the centerline and finish with +55 cm from the centerline for a total of 23 tests. Antenna #1 is the left-most while antenna 12 is the right-most as described in Table 7. The irregular ridge extending from (Traverse Location 55, Antenna Location 65) to (Traverse Location -55, Antenna Location -55) indicates the correlation between location of antenna detecting a tag and location of test.

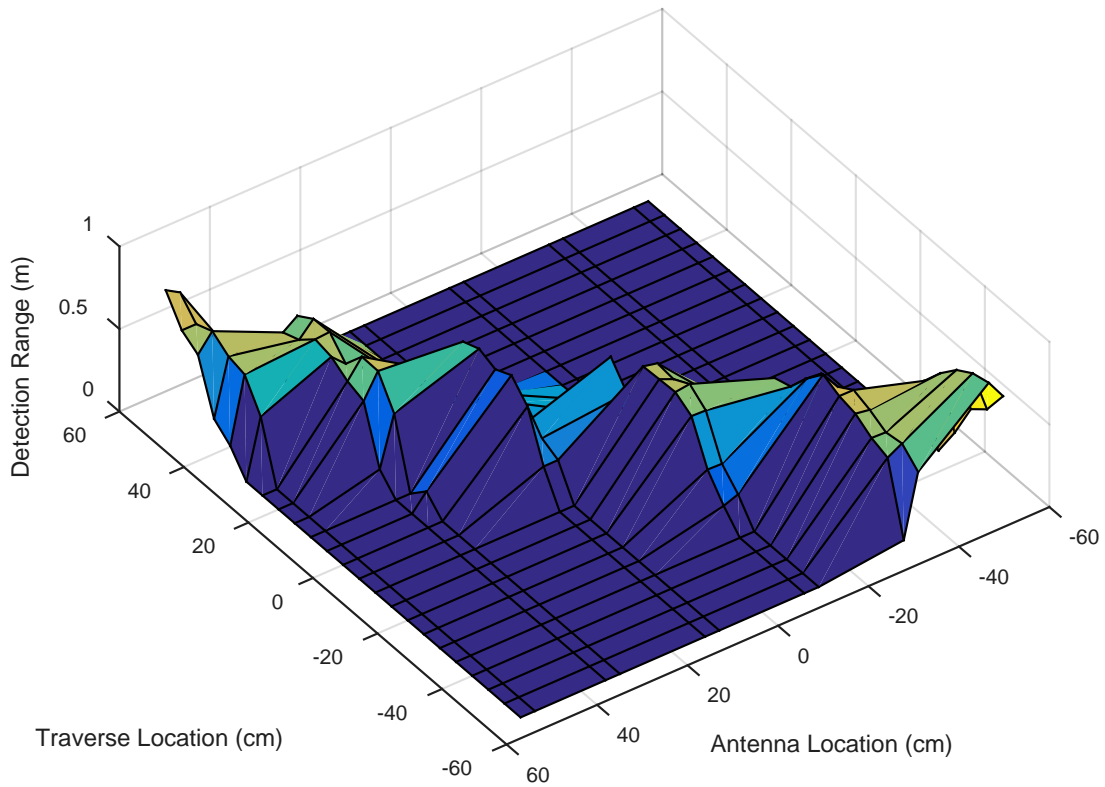


Figure 57 RFID Tag Location Traversing across width of flume

The accuracy of twelve antenna in predicting the location of an RFID tag was evaluated by calculating the centroid of area as follows

$$Centroid = \frac{\sum_{i=1}^{12} y_i w_i}{\sum_{i=1}^{12} w_i}$$

where y_i is the location of the antenna relative to the flume centerline and w_i is the width of the detection range for that antenna (Figure 58). The predicted locations are provided in Table 12 for each of the 23 tests. The actual RFID tag location for each test is compared with the predicted location using the centroid of area method.

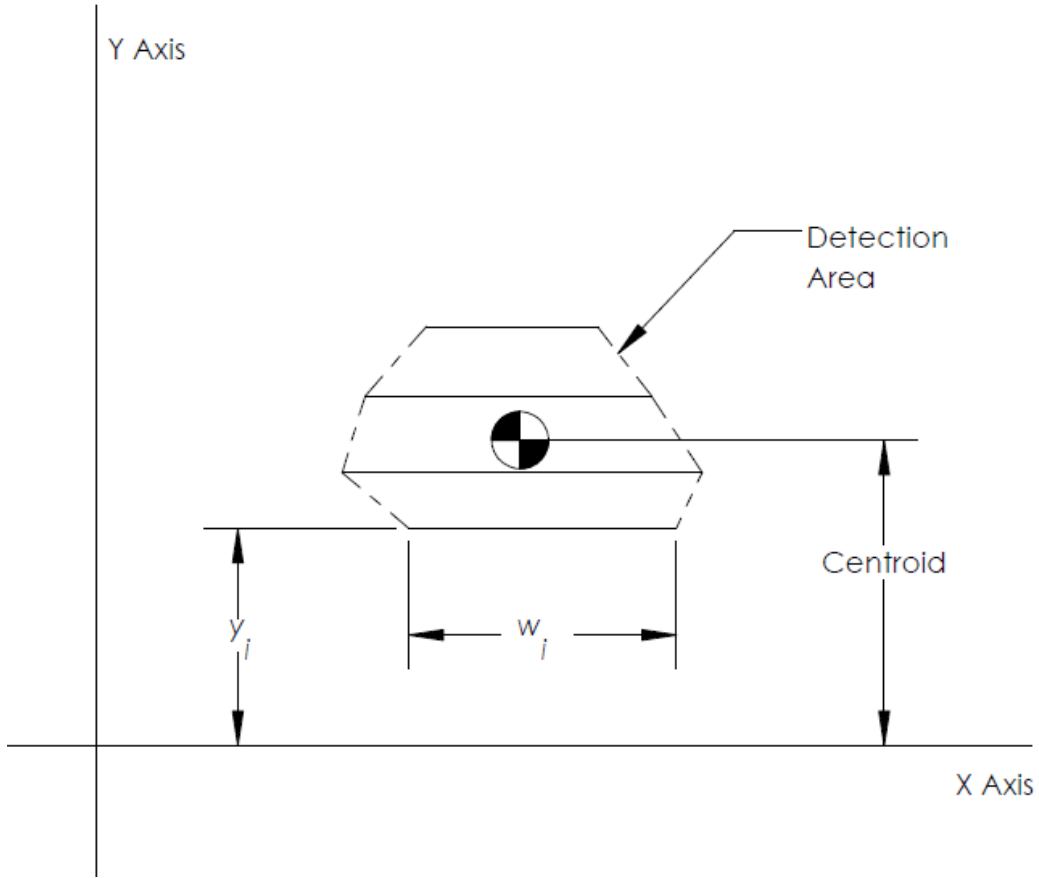


Figure 58 Centroid of Detection Area

Test #	Actual (cm)	Antenna Number, Position (cm), and Detection Range												Predicted (cm)	%Error
		1	2	3	4	5	6	7	8	9	10	11	12		
		+53.3 -30°	+50.2 +30°	+34.5 +30°	+31.4 -30°	+12.6 +30°	+9.4- 30°	-9.4 +30°	-12.6 -30°	-31.4 +30°	-34.5 -30°	-50.2 -30°	-53.3 +30°		
1	-55									0.058	0.434	0.786	0.667	-47.21	6.7%
2	-50									0.474	0.522	0.760	0.503	-43.32	5.7%
3	-45									0.509	0.506	0.696	0.42	-42.59	2.1%
4	-40									0.572	0.558	0.592	0.194	-40.33	0.3%
5	-35									0.595	0.594	0.462	0.001	-37.78	2.4%
6	-30							0.11	0.142	0.641	0.53			-28.99	0.9%
7	-25							0.245	0.242	0.533	0.525			-26.01	0.9%
8	-20							0.485	0.481	0.401	0.409			-21.00	0.9%
9	-15							0.546	0.557	0.368	0.048			-16.69	1.4%
10	-10							0.540	0.503	0.104				-12.78	2.4%
11	-5					0.192	0.192	0.534	0.515					-5.08	0.1%
12	0					0.471	0.24	0.289	0.215					2.27	1.9%
13	5				0.097	0.576	0.249	0.425						6.42	1.2%
14	10					0.528	0.290							11.45	1.2%
15	15			0.101	0.401	0.568	0.258							19.31	3.7%
16	20			0.431	0.574	0.527	0.143							24.40	3.8%
17	25			0.467	0.577	0.257								28.79	3.2%
18	30		0.356	0.531	0.450	0.114								35.67	4.9%
19	35	0.133	0.527	0.553	0.559									36.60	3.9%
20	40	0.212	0.553	0.466	0.554									40.63	0.5%
21	45	0.516	0.621	0.426	0.489									43.24	1.5%
22	50	0.580	0.580	0.087										50.55	0.5%
23	55	0.740	0.688											51.81	2.7%

Table 12 Predicted RFID Tag Lateral Location

The centroid method for predicting the lateral position resulted in a position prediction error ranging from 0.1 to 6.7% of the width of the flume, with the average error of 2.3% or 2.7 cm. The highest amount of prediction error occurred for test #1 and #2. Since there is not a significant error for tests #22 and #23 at the other side of the flume, the effect of steel support structures on both sides of the flume cannot be considered as a contributor to prediction error.

The minimum and maximum detection location method of predicting stream wise location employed in Sections 5.1 and 5.2 was applied to the traverse tests to determine the accuracy of detecting stream wise position as shown in Table 13

Test #	Antenna Number, Minimum and Maximum Detection Location (m)												Avg. (m)	
	1	2	3	4	5	6	7	8	9	10	11	12		
1	Min									-0.235	-0.062	-0.236	-0.405	0.01
	Max									-0.177	0.371	0.550	0.262	
2	Min									-0.378	-0.151	-0.264	-0.317	0.00
	Max									0.095	0.371	0.496	0.187	
3	Min									-0.369	-0.177	-0.234	-0.290	0.00
	Max									0.140	0.329	0.462	0.130	
4	Min									-0.349	-0.230	-0.179	-0.082	0.03
	Max									0.224	0.328	0.413	0.112	
5	Min									-0.396	-0.225	-0.127	0.008	0.02
	Max									0.199	0.369	0.335	0.009	
6	Min							-0.027	-0.087	-0.393	-0.166			0.01
	Max							0.083	0.055	0.249	0.364			
7	Min							-0.094	-0.150	-0.363	-0.219			-0.01
	Max							0.151	0.092	0.170	0.306			
8	Min							-0.291	-0.155	-0.228	-0.112			0.03
	Max							0.194	0.326	0.173	0.297			
9	Min							-0.317	-0.227	-0.250	0.218			0.05
	Max							0.229	0.330	0.119	0.266			
10	Min							-0.324	-0.191	-0.314	0.210			-0.01
	Max							0.217	0.311	-0.210	0.210			
11	Min					-0.064	-0.119	-0.311	-0.181					0.01
	Max					0.127	0.073	0.223	0.334					
12	Min				0.197	-0.303	-0.134	-0.096	-0.132					0.03
	Max				0.197	0.168	0.106	0.193	0.083					
13	Min				0.197	-0.362	-0.135	-0.282						0.02
	Max				0.295	0.214	0.114	0.143						
14	Min				-0.057	-0.326	-0.148							0.06
	Max				-0.057	0.202	0.142							
15	Min			0.007	-0.096	-0.340	-0.156							0.12
	Max			0.109	0.305	0.228	0.102							
16	Min			-0.278	-0.182	-0.272	-0.089							0.10
	Max			0.153	0.393	0.255	0.053							
17	Min			-0.314	-0.180	-0.082								0.12
	Max			0.153	0.397	0.175								
18	Min		-0.285	-0.289	-0.160	-0.012								0.09
	Max		0.072	0.241	0.290	0.102								
19	Min	-0.082	-0.356	-0.313	-0.196									0.08
	Max	0.052	0.171	0.239	0.363									
20	Min	-0.130	-0.357	-0.277	-0.191									0.08
	Max	0.082	0.196	0.189	0.363									
21	Min	-0.204	-0.373	-0.241	-0.145									0.12
	Max	0.312	0.248	0.186	0.343									
22	Min	-0.178	-0.389	-0.009										0.12
	Max	0.402	0.191	0.079										
	Min	-0.210	-0.442											0.13
	Max	0.530	0.246											

Table 13 Minimum, Maximum and Average Streamwise Detection Location Across Flume

The prediction error for the streamwise position ranged from -0.01 m to +0.03m of the actual position.

5.4 RFID tag proximity and collision

When multiple tags are in close proximity, detection of one of the tags may be blocked (Bright, 2014) or no tag data may be successfully obtained due to the interference between the two response signals, an effect that is referred to as signal collision. Multiple tag tests were conducted with two vertically oriented tags at different positions to observe the effect of collision on detection. When the tags were placed within 1 cm of each other in either the stream wise, or lateral direction, neither of the RFID tags were detected. When the tags were spaced at least 2 cm apart in either the stream wise or lateral direction, both tags were detected.

Minimum and maximum detection ranges for the tests involving lateral spacing between RFID tags is provided in Figure 59 and summarized in Table 14. Tag 78 was located at the flume centerline while tag 76 was moved laterally in the positive direction. For each test shown (2 cm, 3 cm, and 4 cm separation), tag 78 is only detected on the two antennas which are located in the laterally negative direction of the centerline, namely antennas #7 located at $-9.4 +30^\circ$ and antenna #8 located at $-12.6 - 30^\circ$. The presence of tag 76 located between 2 to 4 cm west of the flume centerline was blocking antennas # 5 ($+12.6 +30^\circ$) and #6 ($+9.4 -30^\circ$), which are both located in the laterally positive side of the centerline, from detecting tag 78. In the same manner, tag 78 was completely blocking antennas #7 and #8 from detecting tag 76 when the separation was 3 and 4 cm and there was only a small amount of detection from antenna #7 with 2 cm separation.

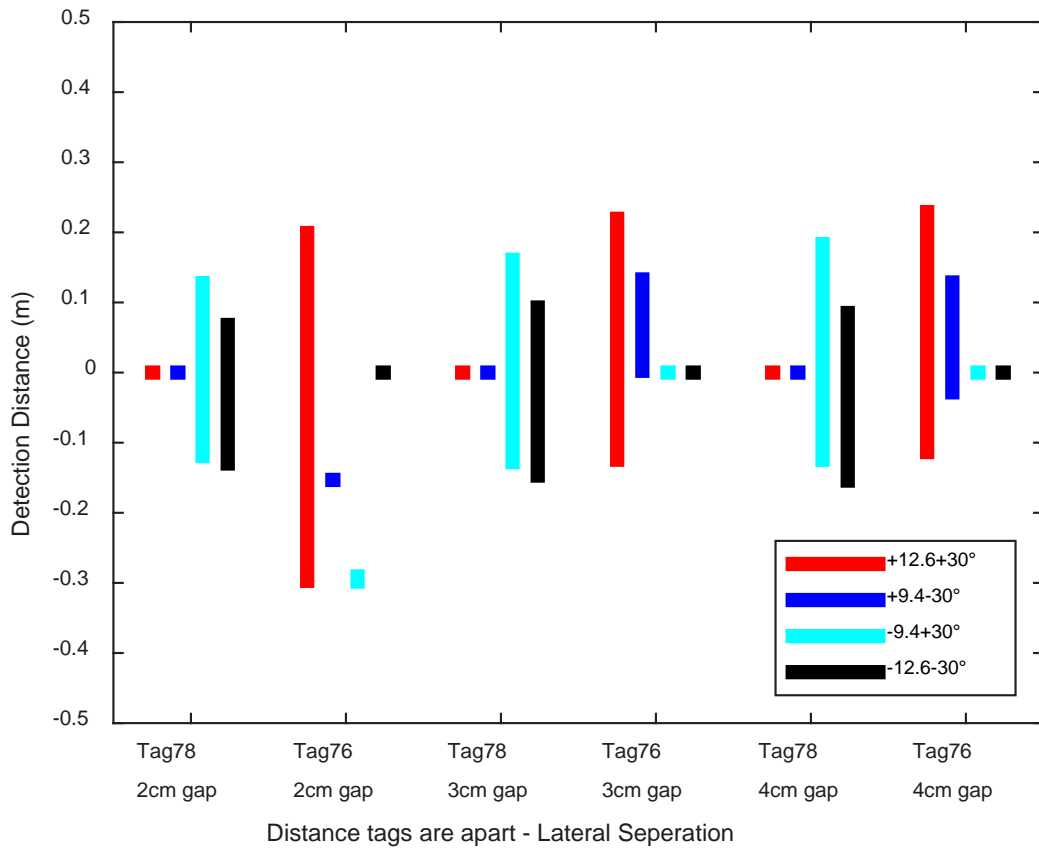


Figure 59 Two Tag Detection at 3.05 m downstream with Lateral Separation

The stream wise position prediction method used in sections 5.1 to 5.3 was applied to the data from multiple RFID tag tests to assess the prediction accuracy with the data provided in Table 14. The predicted stream wise position ranged from -0.17 to +0.06 m of the actual position.

Lateral Separation		Antenna Number, Position (cm), Minimum and Maximum Detection Location (m)				Average (m)	
		5	6	7	8		
		+12.6 +30°	+9.4 -30°	-9.4 +30°	-12.6 -30°		
2 cm	Tag78	min			-0.119	-0.130	-0.01
		max			0.128	0.068	
	Tag76	min	-0.297	-0.153	-0.298		-0.17
		max	0.199	-0.153	-0.291		
3 cm	Tag78	min			-0.128	-0.147	0.00
		max			0.161	0.093	
	Tag76	min	-0.124	0.003			0.06
		max	0.219	0.133			
4 cm	Tag78	min			-0.124	-0.154	0.00
		max			0.183	0.085	
	Tag76	min	-0.113	-0.028			0.05
		max	0.229	0.128			

Table 14 Minimum, Maximum, and Average Detection for 2 tags with Lateral Spacing

Minimum and maximum detection ranges for the tests involving stream wise spacing between RFID tags is provided in Figure 60 and summarized in Table 15. Tag 78 was located at 3.05 m downstream while tag 76 was located at 3.07, 3.08, and 3.09 m downstream for 2 cm, 3 cm and 4 cm separation tests. Wherein lateral spacing of the RFD tags blocked detection by antennas not directly under the tag, stream wise spacing resulting in the detection range being skewed while all scenarios except tag 78 with 2 cm gap were detected on all 4 antennas. The detection range for tag 76 is positive (farther down the flume from the actual tag location) while the detection range for tag 78 was negative. These results indicate that for most of the test while the antennas are sweeping down the flume, when the antennas are closer to the flume head, detection of only tag 78 is occurring and as the carriage moves downstream, detection of only tag 76 occurs. The only exceptions to this are at tag 76 with a 2 cm gap and tag 78 with a 4 cm gap.

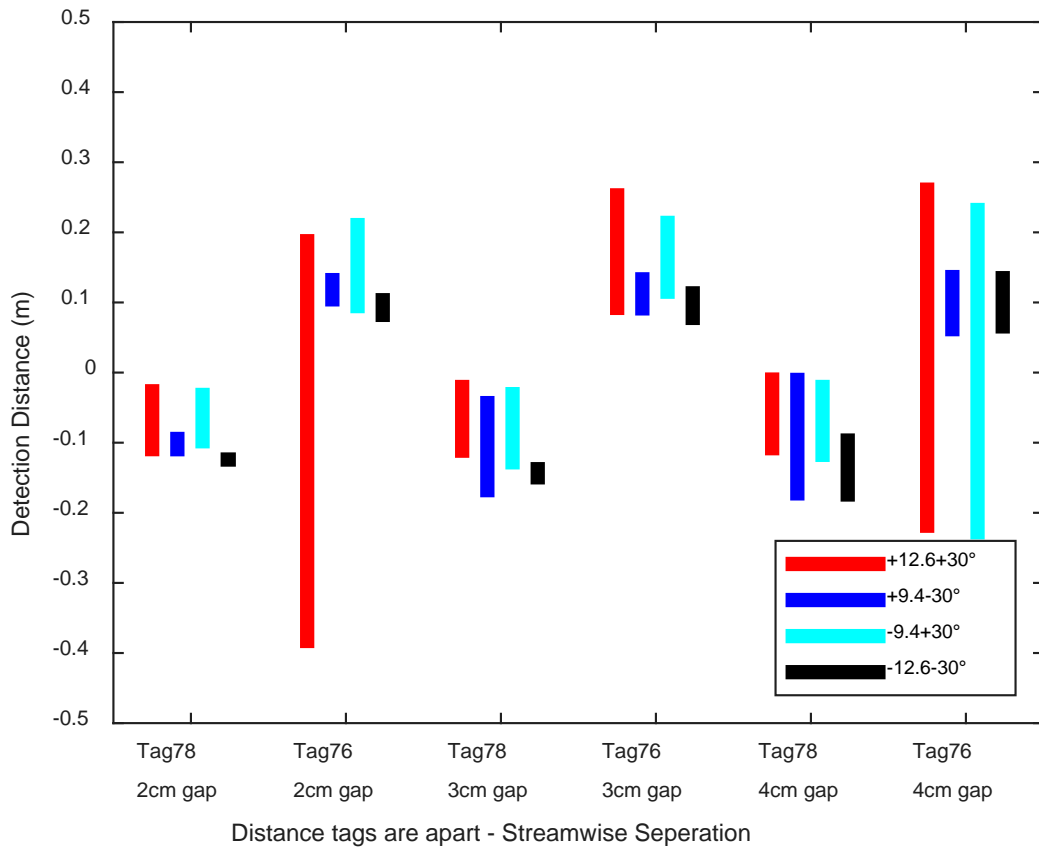


Figure 60 Two Tag Detection at 3.05 m downstream with Stream wise Separation

The prediction of downstream position provided in Table 15 indicate that predictions using average of maximum and minimum detection consistently under estimate the location of tag 78 and over estimate the location of tag 76. The prediction error for tag 78 location is 9 to 10 cm shorter than the actual position while the error for tag 76 is 6 to 14 cm greater than the actual position.

Downstream Separation		Antenna Number, Position (cm), Minimum and Maximum Detection Location (m)				Average (m)	
		5	6	7	8		
		+12.6 +30°	+9.4 -30°	-9.4 +30°	-12.6 -30°		
2 cm	Tag78	min	-0.109	-0.109	-0.098	-0.124	-0.09
		max	-0.027	-0.095	-0.032	-0.124	
	Tag76	min	-0.383	0.104	0.095	0.082	0.07
		max	0.187	0.132	0.210	0.103	
3 cm	Tag78	min	-0.111	-0.168	-0.128	-0.149	-0.10
		max	-0.021	-0.044	-0.031	-0.138	
	Tag76	min	0.092	0.092	0.115	0.078	0.14
		max	0.253	0.133	0.214	0.113	
4 cm	Tag78	min	-0.108	-0.202	-0.117	-0.174	-0.09
		max	-0.010	-0.010	-0.021	-0.097	
	Tag76	min	-0.218	0.062	-0.228	0.066	0.06
		max	0.261	0.136	0.232	0.135	

Table 15 Minimum, Maximum, and Average Detection for 2 tags with Stream Wise Spacing

When multiple tags are being detected simultaneously, detection can occur if the tags are separated at least 2 cm apart but the accuracy of predicting the location using the average of the minimum and maximum detection is lower than scenarios in which only one tag is present.

While the tests with a single tag demonstrate the capacity of multiplexing readers coupled with a stationary personal computer to accurately predict the location of RFID tags, the tests with steel cross brace present, traverse tests across the width of the flume, and test with multiple tags demonstrate the performance of the system under a range of scenarios which may occur during sediment transport experiments.

Chapter 6

Summary and Conclusions

Successful implementation of river engineering projects requires guidelines to ensure designs are sustainable through the ranges of flood conditions and sediment supply experienced by the river. While classifying and comparing rivers provides a basis for creating sustainable channels if the slope, valley profile, hydrograph, and geology are similar, the need for more flexibility in the application of river designs motivates the pursuit of a better understanding of the mechanics driving bedload sediment transport. Such understanding is significantly constrained by the quality and type of data that can be collected using existing methods. While bulk sampling methods such as sediment traps, screened gates and baskets, and Helley-Smith type bedload samplers provide information about the total quantity of sediment being transmitted, they do not provide information on the movement of the individual clasts comprising the overall movement. Indirect transport measurements methods such as motion picture photography, painted sediment tracking, acoustic Doppler profiler bedload velocity measurements, piezoelectric bedload impact sensors, and video analysis of light tables all provided improved spatial detail information on the movement of particles. Most of the indirect transport measurement methods have been used to refine our understanding so that we now recognize that partial mobility is the most common type of transport in gravel-bed rivers. However, these methods are limited in the data they can provide because of their labour intensive nature or extensive calibration requirements.

Sediment transport measurement using tracers provides the ability to gain information on the step size and frequency of steps which comprise the sediment transport. Radioactive tracers can be used on sand sized grains while magnetic and iron tracers can be used on larger particles. If all the particles are seeded at the same location, dispersion information representative of the entire bed can be obtained but information on movement of individual particles is unavailable. RFID tracing provides tracking of individual particles, with the technology continually developing to enable tracking of smaller and smaller particles. Since being demonstrated for sediment transport in 2004, RFID tracking has developed increasing acceptance as a method to quantify the travel distances of sediment between flood events in field studies by sweeping the bed between flood events with an antenna. It has also been used with stationary antennas in natural channels and flumes to observe when the RFID tagged sediment have passed a certain point. However, there is a need for a system that could

combine the sweeping techniques used between floods with the real-time capabilities of stationary antennas to enable the position of the RFID tagged sediment to be tracked over the course of flume sediment transport experiment.

A flume was designed and built with an integrated RFID tracking system to enable sediment transport experiments to be conducted in the flume while continuously tracking the position of RFID tagged sediment. The flume was designed with tilting capabilities to adjust the slope between +.5% (upward sloping) and -2% using a single hydraulic jack located 2/3 down the length of the flume while pivoting at the upstream end. The flume was designed to receive sediment supply from a vibratory feeder equipped with a sediment hopper and water supply from a head tank which was flexibly connected to the flume. Sediment removal from the flume will occur through a sediment trap that will guide the sediment through a light table for video measurement of flux and size distribution. The sediment will be extracted by a screw conveyor that will transfer it above the waterline and then dump it into a bin. The water discharges into a tailwater tank from where it can be pumped back to the head tank.

The flume was designed with space to accommodate an RFID tracking system under the floor of the flume to detect sediment. The tracking system consists of a carriage containing the antennas, tuners, multiplexing RFID readers, batteries, and rollers to enable the carriage to roll along the flanges of the beam supporting the flume. A drive system was developed for the flume to transport the carriage back and forth the length of the flume using cogged belts and pulleys powered by a DC motor with gear reducer. The motion was governed by a PLC with limit switch inputs and manual overrides to control the range of travel. The identification of RFID tags detected by the carriage was transmitted via Bluetooth to a stationary computer which also received carriage position information from a laser range finder.

Validation tests were conducted on the RFID tracking system to establish the detection range and accuracy of the RFID carriage for estimating RFID tag position. Tests conducted with a single tag oriented vertically indicated that predicted tag position was within 1 cm of the actual position when the tag was on the flume centerline with no steel bracing interfering with detection. Tests conducted in the presence of the steel support beam shows that detection would still occur but the prediction error increased to 2 cm for tags located up to 10 cm above the flume floor. Further tests were conducted with the single tag traversed across the width of the flume and it was shown that stream

wise position estimates had an error of up to 4 cm depending on the location across the flume while lateral position estimates had an average error of 3 cm with a maximum error of 8 cm. Finally, tests were conducted with two tags in close proximity and it was found that when the tags are at least 2 cm apart, detection of both tags occurs even though the prediction error increased up to 14 cm.

The method developed for tracking the position of RFID tagged sediment during a flume based sediment transport experiment provides improved sediment tracking capabilities over existing sediment transport measurement techniques by providing continuous data on the location of the sediment over the course of the experiment. This has the potential to provide enhanced data on the step size and step length of particle paths and enable correlation with changing flow conditions in the flume and localized flow conditions obtained from velocity profiling equipment. Further refinement to this technique could be achieved by experimenting with different antenna designs which may provide a larger detection range and by using different types of RFID tags to enable tracking of smaller sized sediment.

Bibliography

- Allan, J. C., Hart, R., & Tranquili, J. V. (2006). The use of Passive Integrated Transponder (PIT) tags to trace cobble transport in a mixed sand-and-gravel beach on the high-energy Oregon coast, USA. *Marine Biology*, 232, 63-86.
- Armstrong, J. D., Braithwaite, V. A., & Rycroft, P. (1996). A flat bed passive integrated transponder antenna array for monitoring behaviour of Atlantic salmon parr and other fish. *Journal of Fish Biology*, 48, 539-541.
- Ashworth, P. J., & Ferguson, R. I. (1989). Size selective entrainment of bed load in gravel bed streams. *Water Resources Research*, 25(4), 627-634.
- Aymes, J. C., & Rives, J. (2009). Detection efficiency of multiplexed Passive Integrated Transponder antennas is influenced by environmental conditions and fish swimming behaviour. *Ecology of Freshwater Fish*, 18(4), 507-513.
- Bagnold, R. A. (1966). An approach to the sediment transport problem from general physics. *Physiographic and Hydraulic Studies of Rivers*, 231-291.
- Bagnold, R. A. (1995). Some flume experiments on large grains but little denser than the transporting fluid, and their implications. *ICE Proceedings: Engineering Divisions*, (pp. 174-205).
- Benelli, G., Pozzebon, A., Raguseo, G., Bertoni, D., & Sarti, G. (2009). An RFID based system for the underwater tracking of pebbles on artificial coarse beaches. *3rd International Conference on Sensor*, (pp. 294–299).
- Biron, P., Carver, R., & D.M., C. (2012). Sediment transport and flow dynamics around a restored pool in a fish habitat rehabilitation project: field and 3d numerical modelling experiments. *River Research and Applications*, 28(7), 929-939.
- Bluetooth. (2001, February 22). Serial Port Profile. *BLUETOOTH SPECIFICATION Version 1.1*. *Bluetooth technology basics*. (n.d.). Retrieved from Bluetooth: <https://www.bluetooth.com/what-is-bluetooth-technology/bluetooth-technology-basics>
- Bradley, D. N., & Tucker, G. E. (2012). Measuring gravel transport and dispersion in a mountain river using passive radio tracers. *Earth Surface Processes and Landforms*, 37(10), 1034-1045.

- Bright, C. J. (2014). *Development of an RFID approach to monitoring bedload sediment transport and a field case study*. Waterloo, ON: University of Waterloo.
- Brown, M., Zeisel, E., & Sabella, R. (2006). *RFID Exam Cram 2*. Pearson.
- Buffington, J. M., & Montgomery, D. R. (1997). A systematic analysis of eight decades of incipient motion studies, with special reference to gravel-bedded rivers. *Water Resources Research*, 33(8), 1993-2029.
- Bunte, K., Abt, S. R., Potyondy, J. P., & Swingle, K. W. (2008). A comparison of coarse bedload transport measured with bedload traps and Helley-Smith samplers. *Geodinamica Acta*, 21(1/2), 53-66.
- Cabrera, E. e. (2010). *Water Engineering and Management Through Time: Learning from History*. CRC Press.
- Carling, P. A., Kelsey, A., & Glaister, M. S. (1992). Effect of Bed Rroughness, Particle Shape and Orientation on Initial Motion Criteria. In R. H. P. Billi, *Dynamics of Gravel Bed Rivers* (pp. 24-39). John Wiley New York.
- Carré, D., Biron, P., & Gaskin, S. (2007). Flow dynamics and bedload sediment transport around paired deflectors for fish habitat enhancement: a field study in the Nicolet River. *Canadian Journal of Civil Engineering*, 34(6), 761-769.
- Chapuis, M., Bright, C. J., Hufnagel, J., & MacVicar, B. (2014). Detection ranges and uncertainty of passive Radio Frequency Identification (RFID) Transponders for sediment tracking in gravel rivers and coastal environments. *Earth Surface Processes and Landforms*, 39, 2109-2120.
- Church, M. (2006). Bed Material Transport and the Morphology of Alluvial River Channels. *Annual Review of Earth and Planetary Sciences*, 34, 325-354.
- Corino, E. R., & Brodkey, R. S. (1969). A visual investigation of the wall region in turbulent flow. *Journal of Fluid Mechanics*, 1-30.
- Damborg, J., & Pellett, K. (2012). *Salmon River Diversion Steelhead and Coho Passage Evaluation*. BC Hydro Fish and Wildlife Compensation Program.

- Diplas, P., Celik, A. O., Valyrakis, M., & Dancey, C. L. (2010). *Some thoughts on measurements of marginal Bedload transport rates based on experience from laboratory flume experiments*. US Geological Survey Scientific Investigations Report, No.5091.
- Diplas, P., Dancey, C. L., Celik, A. O., Valyrakis, M., Greer, K., & Akar, T. (2008). The role of impulse on the initiation of particle movement under turbulent flow conditions. *Science*, 322(5902), 717-720.
- Drake, T. G., Shreve, R. L., Dietrich, W. E., Whiting, P. J., & Leopold, L. B. (1988). Bedload transport of fine gravel observed by motion-picture photography. *Journal of Fluid Mechanics*, 193-217.
- Edwards, T. K., & Glysson, G. D. (1988). *Field methods for measurement of fluvial sediment*. Open-File Report 86-531. Reston, Va: Department of the Interior US Geological Survey.
- Einstein, H. A. (1950). The Bed-load Function for Sediment Transportation in Open Channel Flows. *Technical bulletin No. 1026 (United States. Dept. of Agriculture)*.
- Emmett, W. W. (1980). *A field calibration of the sediment-trapping characteristics of the Helley-Smith bedload sampler* Technical report 1139. Washington: U.S. Geological Survey, United States Government Printing Office.
- Engelund, F., & Hansen, E. (1697). *A monograph on sediment transport in alluvial streams*. Copenhagen: : Teknik Vorlag.
- Ettema, R., & Mutel, C. (2004). Hans Albert Einstein: Innovation and Compromise in Formulating Sediment Transport by Rivers. *Journal of Hydraulic Engineering*, 130(6), 477-487.
- Fetherman, E. R., Avila, B. W., & Winkelman, D. L. (2014). Raft and Floating Radio Frequency Identification (RFID) Antenna Systems for Detecting and Estimating Abundance of PIT tagged Fish in Rivers. *North American Journal of Fisheries Management*, 34, 1065-1077.
- Finkenzeller, K. (2010). *RFID Handbook: Fundamentals and applications in contactless Smart Cards, Radio Frequency Identification and Near Field Communication*. Wiley.
- Friedkin, J. F. (1945). Laboratory study of the meandering of alluvial rivers.
- Ghasemi, A., Abedi, A., & Ghasemi, F. (2012). *Basic Principles in Radiowave Propagation*. New York: Springer .

- Gilbert, G. K., & Murphy, E. C. (1914). *The transportation of debris by running water (USGS Professional Paper 86)*. US Government Printing Office.
- Graf, W. H. (1984). *Hydraulics of sediment transport*. Littleton, Colorado: Water Resources Publication.
- Grass, A. J. (1971). Structural features of turbulent flow over smooth and rough boundaries. *Journal of Fluid Mechanics*, 223-255.
- GridConnect. (2007, June 21). Firefly User Guide Part Number GC-800-314. Retrieved from https://gridconnect.com/media/documentation/roving_networks/Firefly_800314_d.pdf
- Habersack, H. M. (2001). Radio tracking gravel particles in a large braided river in New Zealand A field test of the stochastic theory of bed load transport proposed by Einstein. *Hydrological Processes*, 15, 377-391.
- Habersack, H. M. (2002). The use of radio tracking techniques in bed load transport investigations. *Erosion and Sediment Transport Measurements in Rivers: Technological and Methodical Advances.*, (pp. 172-180). Oslo.
- Haschenburger, J. K., & Church, M. (1998). Bed material transport estimated from the virtual velocity of sediment. *Earth Surface Processes and Landforms*, 23(9), 791-808.
- Hassan, M. A., & Church, M. (2001). Sensitivity of bed load transport in Harris Creek: Seasonal and spatial variation over a cobble gravel bar. *Water Resources Research*, 37(3), 813-825.
- Hassan, M. A., Church, M., & Ashworth, P. J. (1992). Virtual rate and mean distance of travel of individual clasts in gravel bed channels. *Earth Surface Process and Landforms*, 17, 617-627.
- Hassan, M. A., Church, M., & Schick, A. P. (1991). Distance of movement of coarse particles in gravel bed streams. *Water Resources Research*, 503-511.
- Hassan, M. A., Voepel, H., Schumer, R., Parker, G., & Fraccarollo, L. (2013). Displacement characteristics of coarse fluvial bed sediment. *Journal of Geophysical Research: Earth Surface*, 118(1), 155-165.
- Helley, E. J., & Smith, W. (1971). Development and calibration of a pressure-difference bedload sampler. *US Geological Survey Open File Rep.* , 73-108.

- Houbrechts, G., Levecq, Y., Vanderheyden, V., & F., P. (2012). Comparison of methods for quantifying active layer dynamics and bedload discharge in armoured gravel-bed rivers. *Earth Surface Processes and Landforms*, 37, 1501–1517.
- Hubbell, D. W. (1964). *Apparatus and techniques for measuring bedload*. US Government Printing Office.
- Hubbell, D. W., & Sayre, W. W. (1964). Sand transport studies with radioactive tracers. *Journal of the Hydraulics Division*, 90, 39-68.
- Imhol, J. G., Fitzgibbon, J., & Annable, W. K. (1996). A hierarchical evaluation system for characterizing watershed ecosystems for fish habitat. *Canadian Journal of Fish Aquatic Science*, 53(S1), 312-326.
- Intro/Background: Low Frequency RFID Technology*. (n.d.). Retrieved 2016, from Montana State University: <http://www.ece.montana.edu/seniordesign/RFIDFishTracking/intro-background/index.html>
- Jiang, S., & Georgakopoulos, S. (2011). Electromagnetic Wave Propagation into Fresh Water. *Journal of Electromagnetic Analysis and Applications*, 3, 261-266.
- Johnston, J. (n.d.). Work in Progress: RFID Sports Timing System.
- Johnston, P., Bérubé, F., & Bergeron, N. E. (2009). Development of a flatbed passive integrated transponder antenna grid for continuous monitoring of fishes in natural streams. *Journal of Fish Biology*, 74, 1651-1661.
- Jones, E. C., & Chung, C. A. (2007). *RFID in Logistics: A Practical Introduction*. CRC Press.
- Joseph, T. (2014, November). Signal Attenuation from Multiplexing RFID Antennas. *GAO RFID*. Retrieved from <http://www.gaorfid.com/>
- Joyce Dayton. (2013). *Joyce Dayton*. Retrieved from Machine Screw Jacks: <http://joycedayton.com/products/machine-screw-jacks>
- Keller, E. A. (1971). Areal Sorting of Bed-Load Material: The Hypothesis of Velocity Reversal. *Geological Society of America Bulletin*, 82(3), 753-756.
- Keller, E. A. (1999). The transportation of debris by running water, by Grove Karl Gilbert. In D. S. Eldridge M. Moores, *Classic Cordilleran Concepts: A View from California* (pp. 253-256).

- Kesseli, J. E. (1941). The Concept of the Graded River. *The Journal of Geology*, XLIX(6), 561-588.
- Kironoto, B. A., & Graf, W. H. (1995). Turbulence characteristics in rough non uniform open channel flow. *Proceedings of the Institution of Civil Engineers - Water Maritime and Energy*. 112, pp. 336-348. ICE Publishing.
- Kline, S. J., Reynolds, W. C., Schraub, F. A., & Runstadler, P. W. (1967). The structure of turbulent boundary layers. *Journal of Fluid Mechanics*, 741-773.
- Kostaschuk, R., Best, J., Villard, P., Peakall, J., & Franklin, M. (2005). Measuring flow velocity and sediment transport with an acoustic Doppler current profiler. *Geomorphology*, 68, 25-37.
- Kuhnle, R. A., & Southard, J. B. (1988, February). Bed load transport fluctuations in a gravel bed laboratory channel. *Water Resources Research*, 24(2), 247-260.
- Lamarre, H., MacVicar, B., & Roy, A. G. (2005). Using Passive Integrated Transponder PIT Tags to Investigate Sediment Transport in Gravel Bed Rivers. *Journal of Sediment Research*, 75, 736-741.
- Lauth, T., & Papanicolaou, A. (2008). Experimental/Feasibility Study of Radio Frequency Tracers for Monitoring Sediment Transport and Scour around Bridges. *World Environmental and Water Resources Congress 2008*, (pp. 1-10).
- Lauth, T., & Papanicolaou, A. (2009). Application of Radio Frequency Tracers to Individual and Group Particle Displacement within a Laboratory. *World Environmental and Water Resources Congress 2009*, (pp. 1-8).
- Lenzi, M. A., D'Agostino, V., & Billi, P. (1999). Bedload transport in the instrumented catchment of the Rio Cordon Part I Analysis of bedload records conditions and threshold of bedload entrainment. *Catena*, 36(3), 171-190.
- Lenzi, M. A., Mao, L., & Comiti, F. (2004). Magnitude frequency analysis of bed load data in an Alpine boulder bed stream. *Water Resources Research*, 40(7).
- Lenzi, M. A., Marchi, L., & Scussel, G. R. (1990). Measurement of coarse sediment transport in a small alpine stream. *IAHS Publ. No. 193*, (pp. 283-290).
- Leopold, L. B., & Emmett, W. W. (1997). *Bedload and river hydraulics inferences from the East Fork River Wyoming*. U.S. Geological Survey Professional Paper 1583.

- Leopold, L. B., Wolman, M. G., & Miller, J. P. (1964). *Fluvial processes in geomorphology*. San Francisco and London: W H Freeman.
- Lisle, T. E., Iseya, F., & Ikeda, H. (1993). Response of a Channel with alternate bars to a decrease in supply of mixed size bed load. A Flume Experiment. *Water Resources Research*, 29(11), 3623-3629.
- Mackin, H. J. (1948). *Concept of the Graded River*. Geological Society of America Bulletin 59(5).
- MacVicar, B. J., & Roy, A. G. (2007). Hydrodynamics of a forced riffle pool in a gravel bed river: 1. Mean velocity and turbulence intensity. *Water Resources Research*, 43(12).
- MacVicar, B. J., & Roy, A. J. (2011). Sediment mobility in a forced riffle-pool. *Geomorphology*, 125(3), 445-456.
- Mcgee, W. J. (1908). Outlines of hydrology. *Geological Society of America Bullitins*, 19(1), 193-220.
- Meyer-Peter, E., & Müller, R. (1948). Formulas for bed-load transport. (pp. 39-64). Stockholm: IAHR.
- Milan, D. J. (2013). Sediment routing hypothesis for pool-riffle maintenance. *Earth Surface Process and Landforms*, 38(14), 1623-1641.
- Morhardt, J. E., Bishir, D., Handlin, C. I., & Mulder, S. D. (2000). A Portable System for Reading Large Passive Integrated Transponder Tags from Wild Trout. *North American Journal of Fisheries Management*, 20(1), 276-283.
- Moustakidis, I. V. (2012). *Detection of erosion/deposition depth using a low frequency passive radio frequency identification (rfid) technology*, Masters Thesis. University of Iowa.
- National Instruments. (2005). *NI Vision for LabView User Manual*.
- Nichols, M. H. (2004). A Radio Frequency Identificaiton System for Monitoring Course Sediment Particle Displacement. *Applied Engineering in Agriculture*, 20(6), 783-787.
- Nikora, V. (2006). Hydrodynamic effects in gravel-bed rivers: from micro- to macro-turbulence. *National Institute of Water and Atmospheric Research*.
- Nunnallee, E. P., Prentice, E. F., & Jonasson, B. F. (1998). Evaluation of a flat plate PIT tag interrogation system at Bonneville Dam. *Aquacultural Engineering*, 17(4), 261-272.

- Papanicolaou, A. N., Elhakeem, M., & Tsakiris, A. (2010). "Autonomous Measurements of Bridge Pier and Abutment Scour Using Motion-Sensing Radio Transmitter" *IIHR Rep. No. 479*. IIHR: Hydrosience and Engineering.
- Parker, G., & Wilcock, P. R. (1993). Sediment Feed and Recirculating Flumes: Fundamental Difference. *Journal of Hydraulic Engineering*, 119(11), 1192-1204.
- Parker, G., Dhamotharan, S., & Stefan, H. (1983). Model experiments on mobile, paved gravel bed streams. *Water Resources Research*, 18(5), 1395-1408.
- Powell, D. M., Reid, I., & Laronne, J. (2001). Evolution of bed load grain size distribution with increasing flow strength and the effect of flow duration on the caliber of bed load sediment yield in ephemeral gravel bed rivers. *Water Resource Research*, 37(5), 1463-1474.
- PWM. (n.d.). Retrieved from Arduino: <https://www.arduino.cc/en/Tutorial/PWM>
- Reid, I., Laronne, J. B., & Powell, D. M. (1995). The nahal yatir bedload database: Sediment dynamics in a gravel bed ephemeral stream. *Earth Surface Processes and Landforms*, 20, 845-857.
- Reid, I., Layman, J. T., & Frostick, L. E. (1980). The Continuous Measurement Of Bedload Discharge. *Journal of Hydraulic Research*, 18(3), 243-249.
- Rennie, C. D., Millar, R. G., & Church, M. A. (2002). Measurement of Bed Load Velocity using an Acoustic Doppler Current Profiler. *Journal of Hydraulic Engineering*, 128(5), 473-483.
- Rexnord. (2014). *Falk Lifelign Gear Couplings*. Retrieved from Rexnord Gear Coupling Catalog: http://www.rexnord.com/ContentItems/TechLibrary/Documents/451-110_Falk-Lifelign-Gear-Couplings_Catalog-pdf.aspx
- Richenmann, D. (1990). Bedload Transport Capacity of Slurry Flows at Steep Slopes (Doctoral dissertation). Retrieved from <http://e-collection.library.ethz.ch/eserv/eth:37849/eth-37849-02.pd>.
- Rickenmann, D., & McArdell, B. W. (2007). Continuous measurement of sediment transport in the Erlenbach stream using piezoelectric bedload impact sensors. *Earth Surface Processes and Landforms*, 32, 1362-1378.

- Roseberry, J. C., Schmeeckle, M. W., & Furbish, D. J. (2012). A probabilistic description of the bed load sediment flux: 2. Particle activity and motions. *Journal of Geophysical Research*, *117*(F3), F03032.
- Roussel, J.-M., Haro, A., & Cunjak, R. A. (2000). Field test of a new method for tracking small fishes in shallow rivers using passive integrated transponder PIT technology. *Canadian Journal of Fisheries and Aquatic Sciences*, *57*(7), 1326-1329.
- Roy, M. L., Roy, A. G., Grant, J. W., & Bergeron, N. E. (2013). Individual variability of wild juvenile Atlantic salmon activity patterns effect of flow stage temperature and habitat use. *Canadian Journal of Fisheries and Aquatic Sciences*, *70*, 1082-1091.
- RS-232 vs. TTL Serial Communication. (2010, November 23). Retrieved from SparkFun: <https://www.sparkfun.com/tutorials/215>
- Ruiz-Garcia, L., & Lunadei, L. (2011). The role of RFID in agriculture: Applications, limitations and challenges. *Computers and Electronics in Agriculture*, *79*(1), 42-50.
- Schmidt, K.-H., & Ergenzinger, P. (1992). Bedload entrainment, travel lengths, step lengths, rest periods - studied with passive (iron, magnetic) and active (radio) tracer techniques. *Earth Surface Processes and Landforms*, *17*, 147--165.
- Schneider, J., Hegglin, R., Meier, S., Turowski, J. M., Nitsche, M., & Rickenmann, D. (2010). Studying sediment transport in mountain rivers by mobile and stationary RFID antennas. *River Flow 2010*, (pp. 1723-1730).
- Schumm, S. A. (1977). *The fluvial system*. Wiley New York: Wiley.
- Sear, D., Lee, M., Oakey, R., Carling, P., & Collins, M. (2000). Coarse sediment tracing technology in littoral and fluvial environments: Review. In I. Foster, *Tracers in Geomorphology* (pp. 21-55). Chichester, U.K.: John Wiley.
- Shields, A. (1936). Anwendung der Aehnlichkeitsmechanik und der Turbulenzforschung auf die Geschiebebewegung,. *Mitt. Preuss. Versuchsanst. Wasserbau Schiffbau*,(26).
- Simons, D. B., & Richardson, E. V. (1966). Resistance to flow in alluvial channels (Geological Survey Professional Paper 422-J).

- Slaven, S., Slaven, I., & Anders, A. M. (2014). New Gripping and Binding Device Greatly Improves Preparation of Natural Clasts for RFID Tracking. *Journal of Hydraulic Engineering*, 140(12), 06014017.
- Teruhiko Akanuma, M. E. (1989). *United States of America Patent No. US4804932 A*.
- Texas Instrument. (1996). SCBU025. *Antenna Reference Guide TIRIS Technology*.
- Texas Instrument. (2000). SCBU019. *32-mm Glass Transponder Read Only, Read/Write Reference Guide*. Dallas, TX.: Texas Instrument.
- Texas Instrument. (2000). SCBU035. *Series 2000 Reader System Reader S251B RI-STU-251B*.
- Texas Instrument. (2001). SCBS841. *Low Frequency 23mm Glass Transponder RITRP-REHP-30, TI-TRP-WEHP-30*. Dallas, TX.
- Texas Instrument. (2002, March). SCBS845. *Series 2000 Antennas*.
- Texas Instrument. (2004). SCBA019. *LF Reader Synchronization Application Report*.
- Texas Instrument. (2004, July). SCBA019. *LF Reader Synchronization*.
- Texas Instrument. (2005). SCBS851. *Series 2000 Stick Antenna RI-ANT-S01C, RI-ANT-S02C*.
- Violino, B. (2016, April 12). *The History of RFID Technology*. Retrieved from RFID Journal: <http://www.rfidjournal.com/articles/view?1338>
- Wilcock, P. R. (2001). Toward a practical method for estimating sediment transport rates in gravel bed rivers. *Earth Surface Processes and Landforms*, 26, 1395-1408.
- Wilcock, P. R., & McArdell, B. W. (1993). Surface-based fractional transport rates: Mobilization thresholds and partial transport of a sand-gravel sediment. *Water Resources Research*, 29(4), 1297-1312.
- Wilcock, P. R., & McArdell, B. W. (1997). Partial transport of a sand gravel sediment. *Water Resources Research*, 33(1), 235-245.
- Wilcock, P. R., Kenworthy, S. T., & Crowe, J. C. (2001). Experimental study of the transport of mixed sand and gravel. *Water Resources Research*, 37(12), 3349-3358.
- Wright, J. (n.d.). *Dispelling Common Bluetooth Misconceptions*. Retrieved from SANS Technology Institute: <https://www.sans.edu/research/security-laboratory/article/bluetooth>

Yang, C. T. (1976). Minimum unit stream power and fluvial hydraulics. *Journal of Hydraulics Division*, 102, 919-934.

Zimmermann, A. E., Church, M., & Hassan, M. A. (2008). Video-based gravel transport measurements with a flume mounted light table. *Earth Surf. Processes Landforms*, 33, 2285-2296.

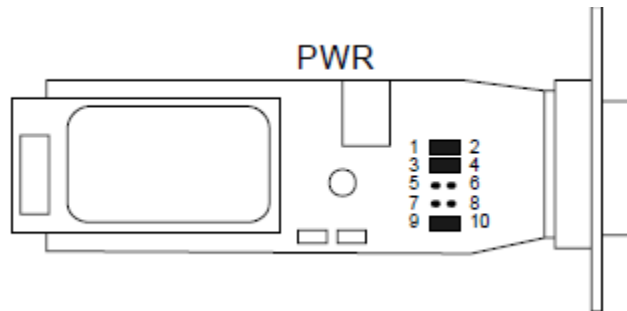
Zydlewski, G. B., Horton, G., Dubrueil, T., Letcher, B., Sean, C., & Zydlewski, J. (2006). Remote monitoring of Fish in Small Streams: A Unified Approach Using PIT Tag. *Fisheries*, 31(10), 492-502.

Appendix A

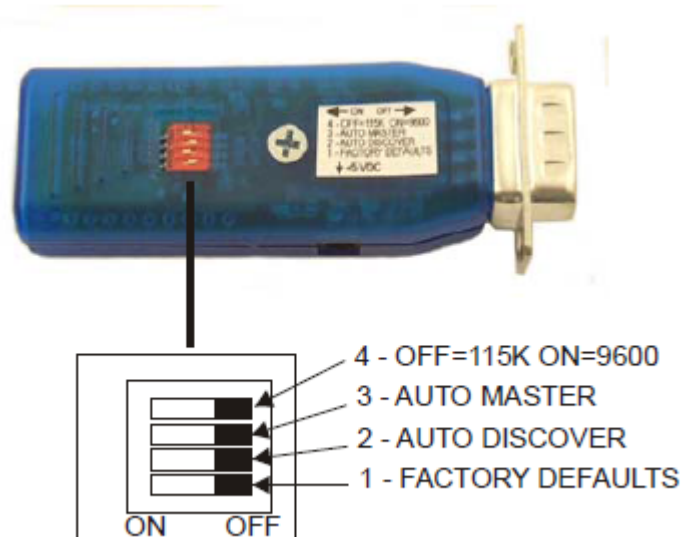
Bluetooth Connection to Oregon RFID Multiplexer

Use AZIO Bluetooth USB dongle. The Windows 7 drivers automatically installed the relevant drivers for this dongle. Use a Null Modem Cable attached between the serial port on the OregonRFID and the GridConnect FireFly, or directly connect the FireFly to the OregonRFID serial port.

Set the jumper settings on the FireFly as follows:

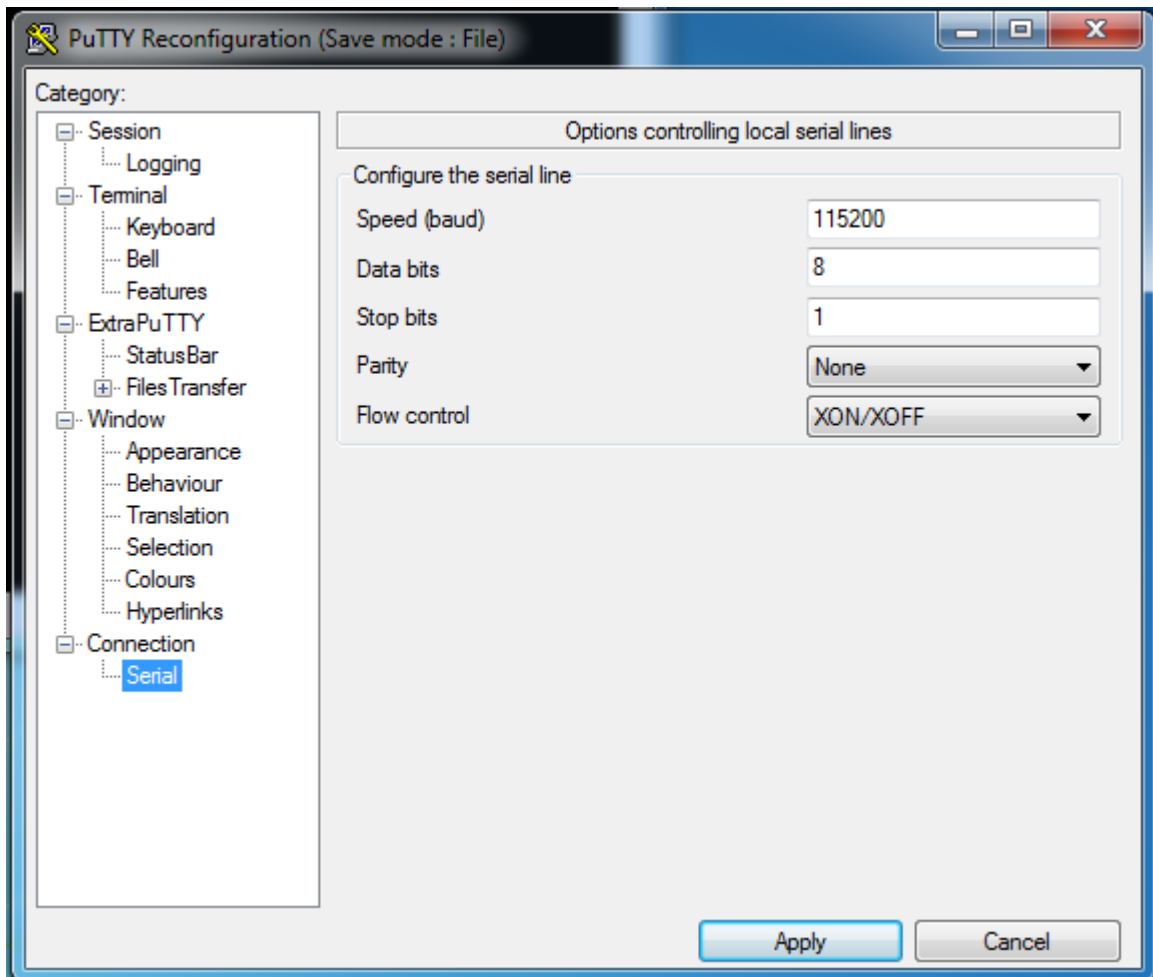


Set the external dip switches on the FireFly as follows:



The multiplexer provides power to the serial connection, so no external power is required for the FireFly Bluetooth dongle.

Before connecting the Firefly to the Null Modem cable, the Firefly was connected via Bluetooth to set up the configuration. The Bluetooth connection was established to the FireFly using a pairing code of 1234 (note, if multiple bluetooth dongles are being used, unique pairing codes for each dongle may need to establish). Serial connection using ExtraPuTTY to the FireFly was obtained using the following parameters:



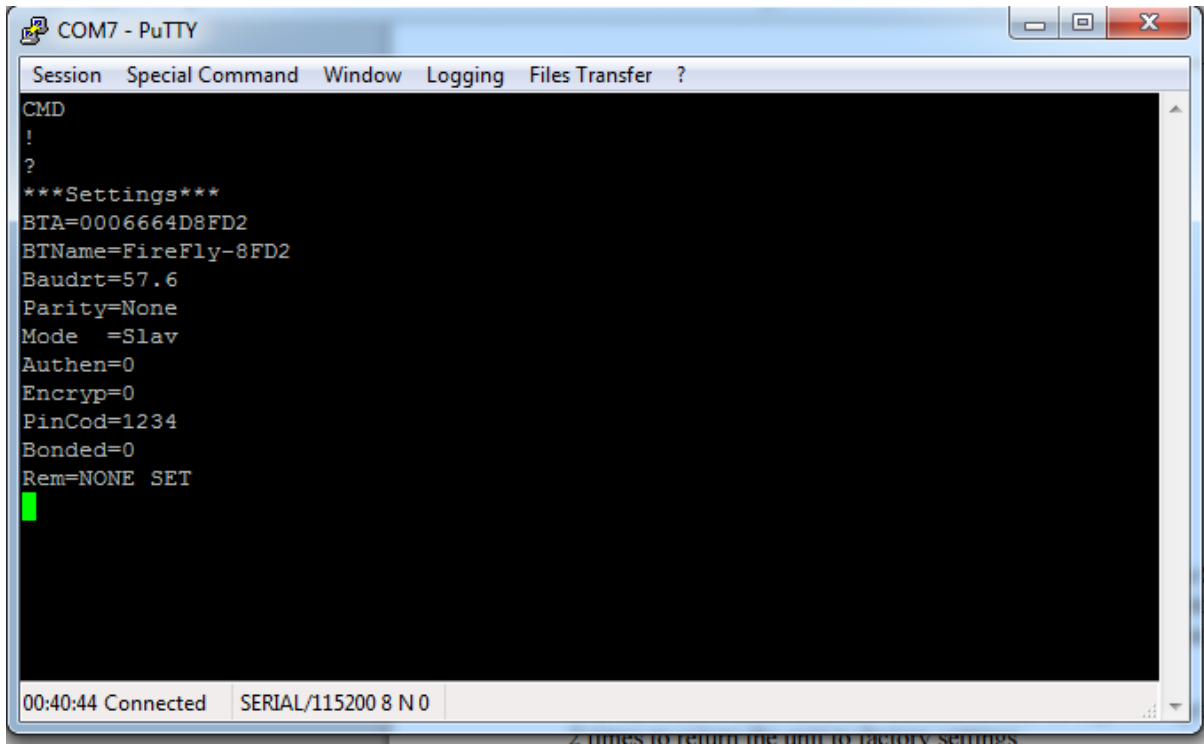
Immediately upon connecting, the \$ key is held down so it FireFly enters command mode. Then the baud rate is set to 57600 to match the baud rate of the OrigonRFID multiplexer using the command:
SU,57 <cr>

To confirm that the setting were entered, enter command:

D <cr>

Note that <cr> stands for carriage return or Enter

The settings should be:



```
COM7 - PuTTY
Session Special Command Window Logging Files Transfer ?
CMD
!
?
***Settings***
BTA=0006664D8FD2
BTName=FireFly-8FD2
Baudrt=57.6
Parity=None
Mode =Slav
Authen=0
Encryp=0
PinCod=1234
Bonded=0
Rem=NONE SET
00:40:44 Connected SERIAL/115200 8 N 0
```

Notice that the software settings inside the Firefly are set at Baudrt of 57.6 even though the PuTTY connection to the FireFly is at 115200.

The baud rate for serial communication over Bluetooth is likely 115200 (the bluetooth connection is simulating a serial port connection <http://www.bluetooth.com/Pages/Fast-Facts.aspx>). However, for the FireFly to receive data from the OregonRFID multiplexer, it needs to be receiving it at buad rate of 57600.

Once the setting have been entered in the Firefly, command mode can be exited by typing

---<cr>

Now the Null Modem cable can be connected between the Multiplexer and the Firefly and it should automatically send data to be viewed on ExtraPuTTY as follows:

Session	Special Command	Window	Logging	Files Transfer	?
2015-05-20	10:43:04.36	00:00:00.00	HW 0000_00000000000030213	A1	1 1589
2015-05-20	10:43:04.36	00:00:00.00	HW 0000_00000000000030213	A1	1 1589 DETECT
2015-05-20	10:43:04.56	00:00:00.41	HW 0000_00000000000030213	A1	5
2015-05-20	10:43:04.56	00:00:00.51	HW 0000_00000000000030213	A1	6
2015-05-20	10:43:04.56	00:00:00.61	HW 0000_00000000000030213	A1	7
2015-05-20	10:43:04.56	00:00:00.61	HW 0000_00000000000030213	A1	7 1 DETECT
2015-05-20	10:43:05.37	00:00:00.11	HW 0000_00000000000030213	A1	2 1 DETECT

00:12:00 Connected SERIAL/115200 8 N 0

Appendix B

PLC and Limit Switch Logic

The layout of the limit switches and outputs are shown in Figure 61

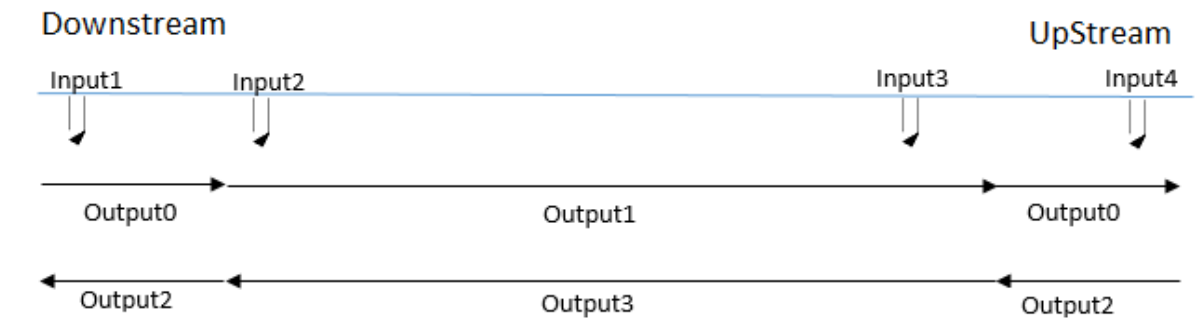


Figure 61 PLC Limit Switch and Output Layout

The 4 limit switches are labeled Input1, Input2, Input3 and Input 4 and wired as shown in Table 16. Thus there are two limit switches at the endpoints and another two in close proximity (1 m) from the travel endpoints.

Channel	Tag	Description
Input 0	_IO_EN_DI_00	Emergency stop (E-Stop)
Input 1	_IO_EN_DI_01	Limit Switch 1
Input 2	_IO_EN_DI_02	Limit Switch 2
Input 3	_IO_EN_DI_03	Limit Switch 3
Input 4	_IO_EN_DI_04	Limit Switch 4
Input 5	_IO_EN_DI_05	User Pushbutton for Forward Movement
Input 6	_IO_EN_DI_06	User Pushbutton for Reverse Movement
Input 7	_IO_EN_DI_06	-
Output 0	_IO_EN_D0_00	Motor Preset Speed 0: slow forward
Output 1	_IO_EN_D0_01	Motor Preset Speed 1: regular speed forward
Output 2	_IO_EN_D0_02	Motor Preset Speed 2: slow reverse
Output 3	_IO_EN_D0_03	Motor Preset Speed 1: regular speed reverse

Table 16 PLC Input and Output List

The logic elements used in the PLC program are provided in Table 17

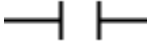
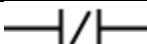
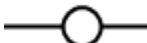

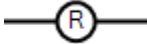
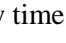
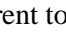
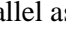
Symbol	Name	Description
	Examine On	Normally open contactor. Allows current through the rung when this input is energized.
	Examine Off	Normally closed contactor. Allows current through the rung when the input is not energized.
	Coil	Output coil momentarily energized when current is going through logic rung.
	Set Coil	Set output coil to on state and leave in the on state when current is going through logic rung.
	Reset Coil	Reset output coil to the off state and leave in the off state when current is going through the logic rung.

Table 17 PLC Logic Elements used in Ladder Logic

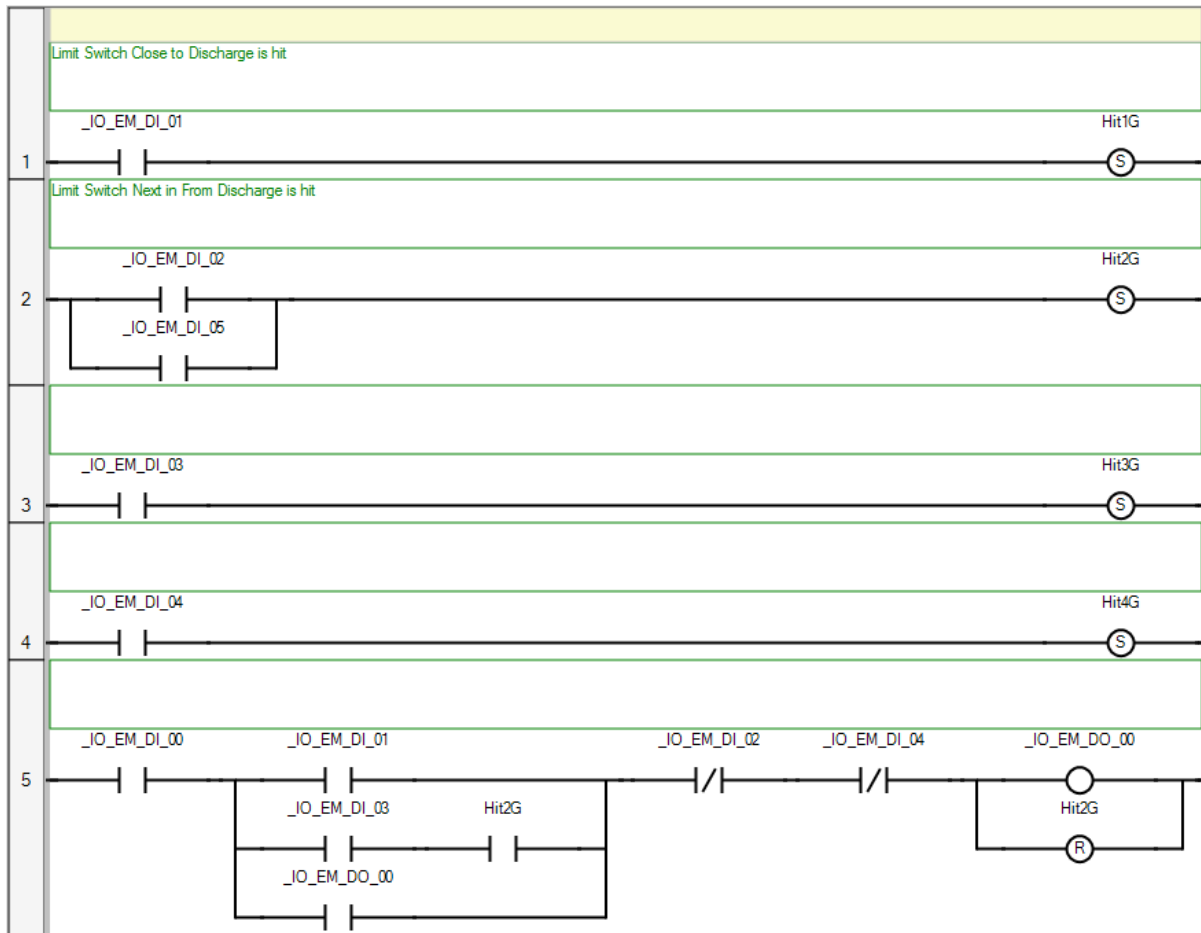
A PLC ladder logic program can be thought of as an electrical circuit with power supplied to the vertical wire running down the left side of the program (where number 1 to 8 are located in Figure 62). Each rung of the ladder is evaluated separately, starting at rung 1 and proceeding to rung 8. The PLC continues to cycle through evaluating each rung of logic from top to bottom while the PLC is on. Any time that an *Examine On* () is connected to an input that is energized, it allows electric current to flow through that rung from left to right. Multiple *Examine On* () elements located in parallel as seen in rung 2 (Figure 62) represent OR logic, while multiple *Examine On* () elements located in series as seen in rung 5 represent AND logic.

With the PLC program for this application (Figure 62), When Input1 is fired, it activates Output0 relay (see Rung 5 in Figure 62) which will control setting 0 on the KB8833. This is a slow forward setting. When Input2 is fired while going forward, Output1 is activated, controlling setting 1 on KB8833 for a fast forward setting. When Input 3 is fired while going forward. Output 0 is activated, for a slow last bit of travel. Output2 is a slow reverse, Output 3 is a fast reverse.

When a signal is received from Input2 or Input3, the PLC needs to be able to figure out which direction the carriage is moving. This is accomplished by setting memory flags corresponding to each limit switch being hit. These flags are called Hit1G, Hit2G, Hit3G, Hit4G. Thus, when Input 2 is fired, the PLC knows it is in the forward direction if Hit1G is still activated. At which point it activated Output1, and resets Hit1G. Alternately, if Hit3G is still active when Input2 is fired, then it knows it is going in the reverse direction and activates Output3 and resets Hit3G.

At the end points, when Input1 is fired, it goes slow forward (Output0), and when Input4 is fired, it goes slow reverse (Output2).

The above controls sequence will operate when the E-stop, that is wired to input 0, is pulled out.



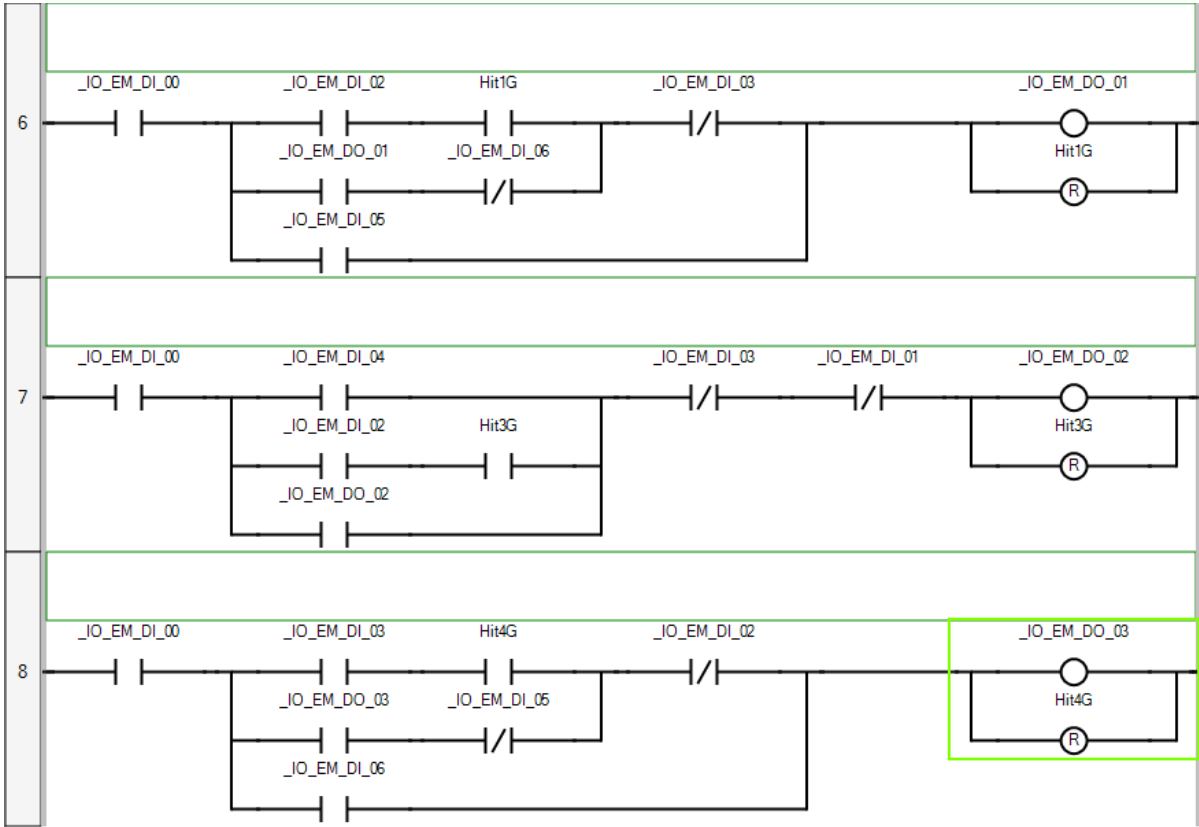


Figure 62 PLC Ladder Logic Program

Appendix C

Jack Screw Details



Detailed Jack Information

06/22/16

Jack Model Number: WJT125U1S-0.00-STDx-STDx-X

Description of Jack: The selected jack is a 5 tons maximum load worm gear machine screw jack with a Standard Base housing, 12:1 ratio gearset, upright, translating, T1 (plain) end condition with standard lead screw. The left hand input shaft is standard. The right hand input shaft is standard.

Selected Jack Data

Screw Diameter	1.5 Inches
Screw Pitch	0.375 Inches
Screw Lead	0.375 Inches
Gear Ratio	12 :1
Screw Thread Root Diameter	1.229 Inches
Static Load	10000 Pounds
Dynamic Load	10000 Pounds
Rise	0 Inches
Linear (travel) Speed	9.375 in/min
Loading Condition	Tension & Compression
Unsupported Length	0 Inches
Column end Fixity	unguided
Column Safety Factor	10.444 :1
Allowable Continuous Travel	66.905 Inches

Performance Details

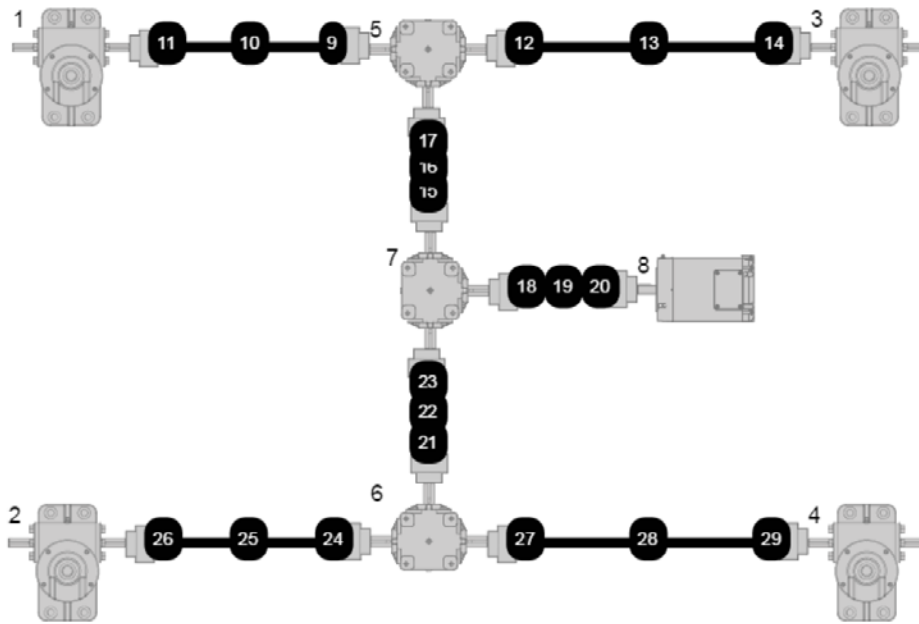
Input Speed	300 rpm
Screw Torque (Raising)	1508.843 in*lb
Screw Torque (Lowering)	296.705 in*lb
Input Starting Torque (Raising)	416.91 in*lb
Input Starting Torque (Lowering)	129.476 in*lb
Input Running Torque (Raising)	257.752 in*lb
Input Running Torque (Lowering)	58.719 in*lb
Input Running Power (Raising)	1.227 HP
Input Running Power (Lowering)	0.28 HP

<u>Stresses & Factors of Safety</u>	<u>F.S. Yield</u>	<u>F.S. Ultimate</u>	<u>Actual Value (lb/in²)</u>
Screw Max. Shear Stress	7.5:1	12.4:1	5,904
Screw Max. Tensile Stress	8.7:1	9.7:1	10,117
Nut Thread Bending Stress	14.4:1	37:1	2,432
Nut Thread Shear Stress	16.4:1	63.3:1	1,067
Input Shaft Stress	5.9:1	13.3:1	5,074
Sleeve Cap (Bolt) Tensile Stress	46.5:1	67.1:1	969
Sleeve Cap (Bolt) Thread Shear Stress	29.1:1	44.1:1	1,316
Worm Cap Bolt Stress	8.7:1	11.4:1	10,537
Worm Cap Bolt Thread Shear Stress	18.7:1	36.6:1	2,457

Misc. Data

Max. Allowable Screw Endplay At Capacity	0.132 Inches
Max. Allowable Screw Endplay At Load	0.132 Inches
Nominal Endplay for a New Jack	0.013 Inches
Thrust Bearing Life	7.57E+5 Inches
Input Shaft Bearing Life	3.81E+6 Inches

System Design



Bill Of Materials

Item ID	Item	Description
1	WJT125U1S-0.00-STDx-STDx-X	HP: 1.23, Torque: 257.75 Lb-in
2	WJT125U1S-0.00-STDx-STDx-X	HP: 1.23, Torque: 257.75 Lb-in
3	WJT125U1S-0.00-STDx-STDx-X	HP: 1.23, Torque: 257.75 Lb-in
4	WJT125U1S-0.00-STDx-STDx-X	HP: 1.23, Torque: 257.75 Lb-in
5	3-way miter box (1:1)	Torque (in): 572.78 Lb-in, Torque (out): 515.50 Lb-in
6	3-way miter box (1:1)	Torque (in): 572.78 Lb-in, Torque (out): 515.50 Lb-in
7	3-way miter box (1:1)	Torque (in): 1272.85 Lb-in, Torque (out): 1145.56 Lb-in
8	Motor	HP: 6.06, Torque: 1272.85 Lb-in
9	Coupling	
10	0 Diameter by 0 Long Shaft with 0 Pillow Block(s)	Torque: 257.75 Lb-in
11	Coupling	
12	Coupling	
13	0 Diameter by 0 Long Shaft with 0 Pillow Block(s)	Torque: 257.75 Lb-in
14	Coupling	
15	Coupling	
16	0 Diameter by 0 Long Shaft with 0 Pillow Block(s)	Torque: 572.78 Lb-in
17	Coupling	
18	Coupling	
19	0 Diameter by 0 Long Shaft with 0 Pillow Block(s)	Torque: 1272.85 Lb-in
20	Coupling	
21	Coupling	
22	0 Diameter by 0 Long Shaft with 0 Pillow Block(s)	Torque: 572.78 Lb-in
23	Coupling	
24	Coupling	
25	0 Diameter by 0 Long Shaft with 0 Pillow Block(s)	Torque: 257.75 Lb-in
26	Coupling	
27	Coupling	
28	0 Diameter by 0 Long Shaft with 0 Pillow Block(s)	Torque: 257.75 Lb-in
29	Coupling	

Appendix D

Using USB Port on Windows Computer to Connect with Oregon RFID Multiplexer

Connect a Null Modem RS232 cable between Oregon RFID Multiplexing reader and the blue Prolific USB-to-Serial conversion cable. Windows should automatically assign a Com Port which will be viewable by going to device manager. For this example, COM5 was assigned to the serial port connection.

Serial Port communication is achieved by opening up a terminal port connection with the device. ExtraPutty is a commonly used terminal emulator program available free from <http://www.extraputty.com/>. The ExtraPutty terminal emulator will be used for the rest of this example.

Start up ExtraPutty. When it first starts, the following screen will appear:

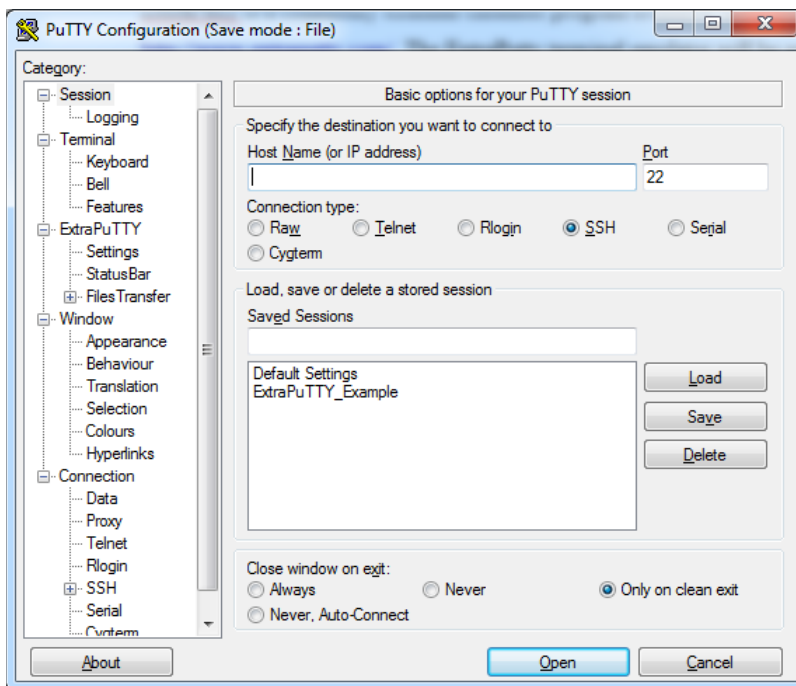


Figure 63 PuTTY Startup Screen

Select the “Serial” option on the left tree options, then in the window “Options controlling local serial line”, for “Serial line to connect to” enter COM5, for “Speed (baud)” enter 57600, and for “Flow Control”, select None (DTR/RTS disable)

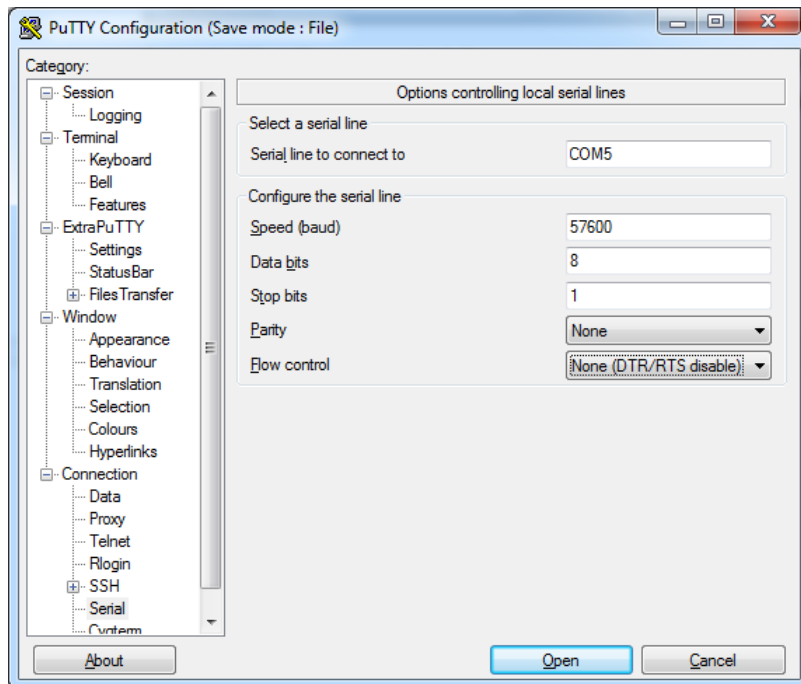


Figure 64 PuTTY Serial line configuration

Appendix E

RFID Mechanical Drive Components

<u>Description</u>	Part Number	Qty	Units	Unit Price	Ext. Price
Type L Timing Belting Urathane, width: 1/2", pitch: 3/8", length: 120 '	1840K3	120	Feet	3.51	421.20
Type L End Plate for mounting both ends of belting to flat surface	2253K91	1	Each	64.02	64.02
Type L Series Timing Pulley Fits 1/2" Belt, 2.39 OD, 18 Teeth, JA Bushing	6495K211	4	Each	34.42	137.68
Quick-Disconnect Bushing, JA Style, Standard ANSI Keyway, Bore Size: 1"	6086K31	4	Each	12.24	48.96
Cast Iron Flange-Mounted Steel Ball Bearing for 1" Shaft Diameter, 4-7/8" Base Length	5968K75	2	Each	39.33	78.66
Cast Iron Base-Mounted Steel Ball Bearing, Eccentric Lock for 1" Shaft Diameter	6361K37	2	Each	39.68	79.36
Conveyor Belt Tensioner with Adjusting Screw, Settl, 3" Maximum Adjustment, 6-7/8" Overall Length	60085K11	2	Each	105.46	210.92
Total					1,040.80

Table 18 RFID Carriage Mechanical Drive Components from McMaster Carr

Appendix F

Servo Drive Pricing Sheet



Date: July 17, 2015
 End Customer: University of Waterloo
 Contact: John Hufnagel

885 Milner Avenue
 Toronto, Ontario
 M1B 5V8

Qty	Part Number	Description	Price Each	Quantity Total
		-		
1	VRL-090B-25-K5-14BJ14	Gearbox 25:1 ratio VRL size 90	\$940.00	\$940.00
1	R88M-K40030T-S2 R88A-	400W,240V,3000rpm ABS K Mtr	\$535.00	\$535.00
1	CRKA005CR-E R88A-	5m CRKA High Flex Encoder Cable-eu	\$110.00	\$110.00
1	CAKA005SR-E	5m CAKA High FlexPwr Cable -eu	\$75.00	\$75.00
1	R88D-KN04H-ECT R88A-CRGD0R3C-BS	G5 SERVO 400W/200V ECAT ABSOLUTE ENCODER G SERIES BATTERY CABLE W/BATTERY	\$731.00	\$731.00
1	XW2Z-100J-B34	G5 SERVO I/O CABLE. 1M, CONNECTS TO XW2B-20GX TERMINAL BLOCK	\$111.00	\$111.00
1	XW2B-20G4	TERMINAL BLOCK,120 WAY, TO CABLE CONNECTOR	\$75.00	\$75.00
1	R88A-CSK003S-E	G5 SAFETY CABLE, R88A-CSK003S-E	\$32.00	\$32.00
1	R88A-RR22047S1	EXTERNAL REGENERATIVE RESISTOR, 220 W 47 OH	\$28.00	\$28.00
			\$55.00	\$55.00
1	NJ101-1000	NJ1 CPU 2 Axis ECAT EIP	\$1,382.00	\$1,382.00
1	NJ-PA3001	NJ5 POWER SUPPLY UNIT 100 TO 240VAC	\$201.00	\$201.00
1	NX-ECC201	NX EtherCAT Coupler	\$115.00	\$115.00
1	NX-ID5442	NX 16Pt, 24 VDC, PNP Input	\$80.00	\$80.00
1	NX-OD5256	NX 16Pt 12-24VDC PNP Trans Out	\$100.00	\$100.00
1	NX-PC0010	NX IO Pwr, IOG 16Pts, 5-24VDC	\$26.00	\$26.00
1	NX-PC0020	NX IO Pwr, IOV 16Pts, 5-24VDC	\$26.00	\$26.00
1	NA5-7W001B	Sysmac NA HMI, 7", Black	\$2,090.00	\$2,090.00
1	SYSMAC-SE00L	SYSMAC STUDIO 1 USER LICENSE ONLY	\$1,000.00	\$1,000.00
Grand Total:				\$7,712.00
				0